# Graphene and Silicon Materials for Quantum Computing

## Anisotropic etching in graphene and high mobility SiMOSFETs with thin oxides

**Inauguraldissertation**

zur

Erlangung der Würde eines Doktors der Philosophie

vorgelegt der

Philosophisch-Naturwissenschaftlichen Fakultät

der Universität Basel

von

**Timothy Nigel Camenzind**

Basel, 2021

Genehmigt von der Philosophisch-Naturwissenschaftlichen Fakultät auf Antrag von

Prof. Dr. D. M. Zumbühl

Prof. Dr. I. Zardo

Prof. Dr. F. A. Zwanenburg

Basel, den 22.06.2021

Prof. Dr. M. Mayor

Dekan

# Abstract

Quantum computing has the highest demand on device quality in order to achieve long coherence times. Therefore, this thesis investigates the two materials graphene and silicon for their particular use in quantum computing applications.

Graphene nanoribbons (GNRs) are a very promising playground for novel states of matter like Majorana fermions, for spin filtering or magnetic ordering. The creation of such states depends on the edge termination of the GNRs which can be produced by using a remote hydrogen or remote nitrogen plasma respectively. Here, we report the successful use of a remote hydrogen plasma which creates etch pits with zigzag terminated edges. This demonstrates the viability of a GNR fabrication process for spin-filtering applications in graphene systems. A remote nitrogen plasma has also been investigated, however, we were not able to find the remote nitrogen regime where anisotropic etching occurs.

Second, silicon is already widely used as a promising candidate for spin qubit applications. The goal of the experiments conducted in this thesis was to investigate the quality of a device fabricated in a fully CMOS compatible process. This has been done by measuring the mobility of the electric charge carriers and by analysing the top gate material influence on the mobility. We report a record mobility of $17.5 \times 10^3\,\mathrm{cm}^2/\mathrm{Vs}$ which, in combination with other extracted parameters, indicates a high quality interface, opening new avenues for high quality quantum dot applications.

# Contents

# 1 Introduction

Finding the ideal material for any given purpose is no easy task. Each and every application has its specific prerequisites, a diverse set of difficulties and a wide range of its possible future use which all need to be addressed by using the right set of tools. In physics, finding the appropriate material can result in the discovery of the key to unveil another part of the universe, or the resources for building the machine that brings the computational power to the next level − the quantum computer.

Building the quantum computer has already been the dream of many people and has been theorized to work with a multitude of quantum building blocks. In recent years, efforts to build the quantum computer have focussed on a few different options which all share the same basic principle: having a two-level system [1]. The proposals and sometimes experiments range from trapped ions [2–4] over superconducting qubits [5–8] to spin qubits [9–12]. Another approach involves using more exotic states like Majorana and Para-fermions. Their non-abelian statistics implicate a more complex system, but are upon discovery viable candidates for qubit implementations.

However large the difference in the underlying physics might be for the above mentioned realisations, they all share the same underlying fact − the need for a high quality host material. Therefore, a large number of semiconductor materials have been investigated such as gallium arsenide (GaAs) [10, 12] and silicon-germanium (SiGe) heterostructures [13], various types of nanowires (InAs [14], InSb [15], GeSi [16]) and silicon [17–19]. Other non-semiconductors include two-dimensional materials like transition metal dichalcogenides (TMDC) [20] and graphene [21, 22]. In this thesis, two of those materials have been looked into for two distinct applications: On the one hand, graphene for spintronics and Majorana-related physics and, on the other hand, silicon for spin qubits. Both materials have been studied extensively in the recent years and due to improvements in the quality of the material and the fabrication process, new and interesting physics have been found such as superconductivity in bilayer graphene

[22] and multiple connected spin qubits in silicon [13].

In order to host Majorana fermions, the graphene device quality has to be improved, lying a special focus on the edge quality. Only a so-called graphene nanoribbon (GNR) with pristine crystallographic edges has the necessary band structure to host this exotic state [23]. Therefore, in the first part of this thesis, the etching characteristics of both a remote hydrogen as well as nitrogen plasma are investigated. It has been proposed that both hydrogen and nitrogen radicals, which are neutral single atoms, induce anisotropic etching in graphite and graphene [24, 25]. The resulting etch pits therefore have a hexagonal shape with one of the two crystallographic directions of graphene − armchair in the case of etching with nitrogen radicals and zigzag when using hydrogen radicals. A GNR with zigzag edge termination is predicted to act as a spin filter [26] whilst a GNR with armchair edge termination can host Majorana fermions [23].

The second part of this thesis will deal with a completely different material − silicon. As one of the most abundant materials on earth it is extensively used in the current semiconductor industry for almost every single electronic device. Using silicon in order to build the quantum computer seems to be the logical conclusion because of the vast infrastructure and the knowledge which has already been acquired so far. However, the disordered interface between silicon and its oxide limits both the quality and reproducibility of future qubit devices [27–29]. Therefore, a careful study of the interface is needed in order to improve the device quality, which has been accomplished in this thesis by investigating the mobility limiting factors of two of the most common top gate materials for silicon metal oxide semiconductor field effect transistors (SiMOSFETs).

## 1.1 Thesis Outline

This thesis is organized as follows: chapter 2 introduces the two investigated systems − graphene and silicon − on a theoretical level and provides relevant background information for the reader to understand the later chapters. Chapter 3 goes into

the anisotropic etching of graphite and graphene by using a remote hydrogen plasma resulting in hexagonal shaped etch pits with a zigzag edge termination. The subsequent chapter 4 describes the process of using a remote nitrogen plasma in order to fabricate nanoribbons with armchair termination for hosting Majorana fermions. In chapter 5, the mobility limiting factors of SiMOSFETs are discussed. The investigated device has shown a record electron mobility for SiMOSFETs with sub 10 nm oxide thickness. Chapter 6 summarizes the work done in this thesis and gives an outlook on future research in the field of graphene and silicon.

# 2 Theory

## 2.1 Graphene

For almost 70 years, an isolated single atomic layer of graphite − graphene − was deemed impossible to fabricate. Graphene was described to be thermodynamically instable and it could not exist as a material in a vacuum without any support [30, 31]. Nevertheless, due to the interesting character of an atomically thin conducting layer, theorists described graphene in full detail [32–34] and even predicted massless charge carriers to exist in this system [35, 36]. In parallel, experimentalists tried to develop a fabrication process for graphene with various degrees of success [37–39]. In the end, Novoselov and Geim discovered that there is a way to produce graphene flakes: by mechanically exfoliating common graphite with a scotch tape and transferring it on a silicon/silicon oxide ($Si/SiO_2$) surface [21]. The weak interaction between the silicon oxide surface and graphene allowed for a thermodynamically stable state and the electrical isolation of $SiO_2$ resulted in graphene being nearly charge neutral. This discovery opened up a whole new field of experiments on graphene ranging from the proof of massless Dirac fermions [40, 41] to the discovery of superconductivity in bilayer graphene at a magic angle [22].

### 2.1.1 Structure of Graphene

In order to understand the properties of graphene one needs to look at the characteristics of the fundamental building block − the carbon atom. A free standing carbon atom contains six electrons in total, arranged in a $1s^2 2s^2 sp^2$ configuration. By hybridizing the $s$- and $p$-orbital, the valance electrons can form covalent bonds with other atoms (see figure 2.1. Carbon can host up to four of those so called $\sigma$-bonds and if it does, the result is one of the common carbon forms known as diamond. In this case, the angle between each bond measures 109.5° and the molecule forms a tetrahedron. Alterna-

tively, electrons in the $p$-orbital can form a different kind of bond, called the $\pi$-bond, which will form a double bond when in combination with a $\sigma$-bond. This strengthens the bond between two atoms. In order to minimise energies, the bonds between the carbon atoms now lie in one plane with an 120° angle between them thus forming a honeycomb pattern, the lattice of graphene. Because the $p$-orbitals involved in the $\pi$-bonds stick out of the plane at a 90° angle, they form a plane of conductance above and below the graphene honeycomb lattice in which electrons can move freely in two dimensions. This has first been described by Wallace in 1947 using a tight binding approach [32]. The outline of this approach will be described in the following paragraphs based on reference [42].

In contrast to other patterns, the unit cell of graphene cannot be described with a single atom. The honeycomb pattern has to be described with a two-atom unit cell and the lattice vectors are given by

$$\vec{a}_1 = \frac{a_0}{2}\begin{pmatrix} 3 \\ \sqrt{3} \end{pmatrix} \quad \text{and} \quad \vec{a}_2 = \frac{a_0}{2}\begin{pmatrix} 3 \\ -\sqrt{3} \end{pmatrix} \tag{2.1}$$

where $a_0 = 1.42$ Å denotes the carbon-carbon distance. The corresponding reciprocal vectors are given by

$$\vec{b}_1 = \frac{2\pi}{3a_0}\begin{pmatrix} 1 \\ \sqrt{3} \end{pmatrix} \quad \text{and} \quad \vec{b}_2 = \frac{2\pi}{3a_0}\begin{pmatrix} 1 \\ -\sqrt{3} \end{pmatrix}. \tag{2.2}$$

This description results in a system of two sublattices (A and B) and a Brillouin zone with four points of symmetry, namely $\Gamma$, $M$, $K$ and $K'$ (see figure 2.1). Why the two valley points $K$ and $K'$ are of special note can be explained using the band structure calculation. In a tight binding approach, a conducting electron in a p-orbital can hop to the position of its three nearest neighbours

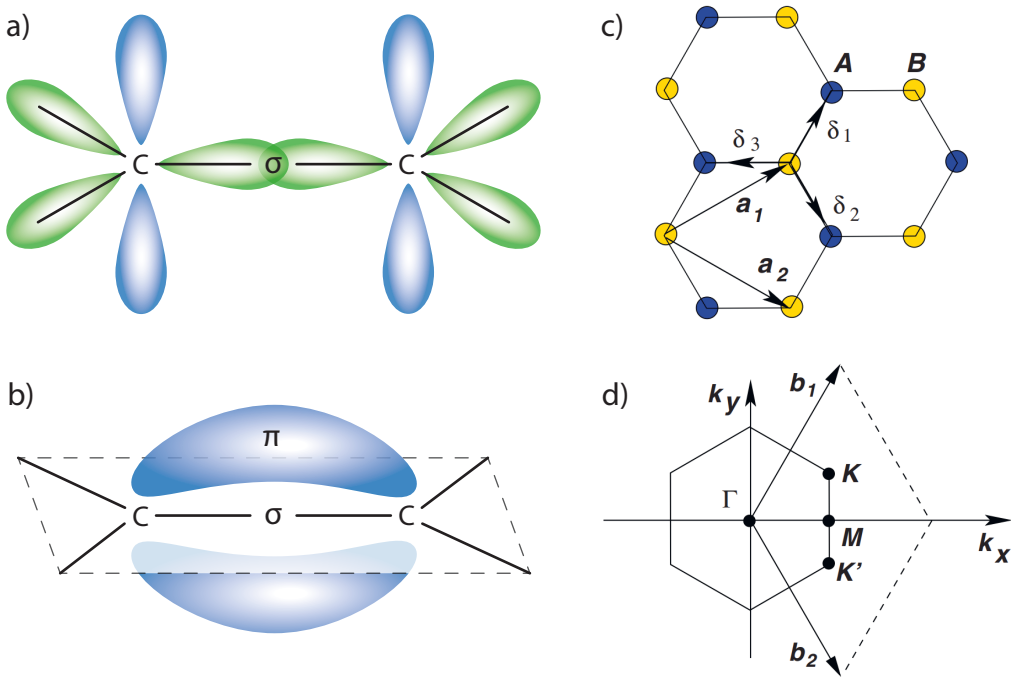


**Figure 2.1: Schematic of chemical bonds and lattice schematic of graphene.** (a) The s- and two p- orbitals of carbon can undergo hybridisation, forming $sp^2$ hybridised orbitals (green) which can form $\sigma$-bonds with other $sp^2$ hybridised orbitals of another atom. (b) The remaining $p$-orbital (blue) can then form covalent $\pi$-bonds, resulting in a double bond. The $\pi$-bond network in graphene is the main contributor to the electronic transport. (c) The graphene lattice consists of a unit cell with two carbon atoms (yellow and blue) with the corresponding lattice vectors $a_1$ and $a_2$ and the three nearest-neighbour vectors $\delta_{1,2,3}$. (d) The resulting reciprocal lattice schematic with the reciprocal unit vectors $b_{1,2}$ shows the important symmetry points $\Gamma$ and $M$, as well as $K$ and $K'$, the valleys of graphene. Figures (a) and (b) adapted from ref [43], (c) and (d) adapted from [42].

$$\vec{\delta}_1 = \frac{a_0}{2}\begin{pmatrix}1\\ \sqrt{3}\end{pmatrix}, \quad \vec{\delta}_2 = \frac{a_0}{2}\begin{pmatrix}1\\ -\sqrt{3}\end{pmatrix} \quad \text{and} \quad \vec{\delta}_3 = -a_0\begin{pmatrix}1\\ 0\end{pmatrix} \tag{2.3}$$

and to the next-nearest neighbours

$$\vec{\delta}'_1 = \pm\vec{a}_1, \quad \vec{\delta}'_2 = \pm\vec{a}_2 \quad \text{and} \quad \vec{\delta}'_3 = \pm\left(\vec{a}_2 - \vec{a}_1\right). \tag{2.4}$$

The resulting Hamiltonian with units used such that $\hbar = 1$ reads

$$H = -t \sum_{\langle i,j\rangle,\sigma} \left(a^{\dagger}_{\sigma,i} b_{\sigma,j} + \text{H.c}\right) - t' \sum_{\langle\langle i,j\rangle\rangle,\sigma} \left(a^{\dagger}_{\sigma,i} a_{\sigma,j} + b^{\dagger}_{\sigma,i} b_{\sigma,j} + \text{H.c.}\right). \tag{2.5}$$

In this equation, $t$ designates the energy needed for hopping between two sublattices (nearest neighbour) and $t'$ for hopping within the same sublattice (next-nearest neighbour). $a^{\dagger}_{\sigma,i}$ and $a_{\sigma,i}$ are the creation and annihilation operators of an electron with spin $\sigma = \uparrow, \downarrow$ on site $R_i$ within the sublattice A. An equivalent notation is used for sublattice B, that is $b^{\dagger}_{\sigma,i}$ and $b_{\sigma,i}$. Based on this Hamiltonian one can calculate the energy bands

$$E_{\pm}(\vec{k}) = \pm t\sqrt{3 + f(\vec{k})} - t' f(\vec{k}) \tag{2.6}$$

with

$$f(\vec{k}) = 2\cos\left(\sqrt{3}k_y a\right) + 4\cos\left(\frac{\sqrt{3}}{2}k_y a\right)\cos\left(\frac{3}{2}k_x a\right). \tag{2.7}$$

A 3-dimensional scheme is show in figure 2.2, where a special focus lies on the $K$ and $K'$ points in the Brillouin zone. Upon expanding the full band structure at these two points, one can show that the dispersion relation becomes linear for a small enough momentum $\vec{q}$ if measured relatively to $K$ and $K'$ ($\vec{k} = \vec{K} + \vec{q}$, with $|\vec{q}| << |\vec{K}|$):

$$E_{\pm}(\vec{q}) \simeq \pm v_F |\vec{q}| + \mathcal{O}\left[(q/K)^2\right] \tag{2.8}$$

$v_F = 3ta/2 \simeq$ 1e6 m/s represents a constant Fermi velocity. A direct consequence of this linearity around the $K$ and $K'$ points is that graphene becomes a zero band gap conductor and therefore one can continuously tune the system from hosting holes to hosting electrons by applying an electric field. The fact of having no band gap can be a blessing and a curse at the same time. On the one hand, graphene systems can be engineered to host both charge carriers in sequence and are the electronic equivalent to semi-transparent mirrors in optics [45, 46]. On the other hand, graphene transistors

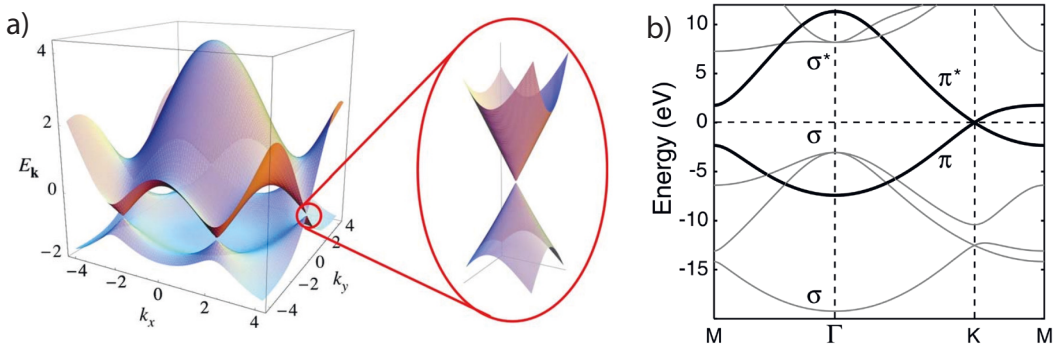


**Figure 2.2: Band structure of graphene.** (a) The energy surface of a graphene ring which shows that the minima of the conduction band lie at the $K$ and $K'$ points. The zoom-in highlights the linear dispersion relation around these highly symmetric points and shows that the approximation is only viable close to the Dirac point. (b) In the dispersion relation it becomes apparent that the $\sigma$-bonds have a band gap, whereas the $\pi$-bonds do overlap at the $K$ and $K'$ points which allows for conductance at the Fermi energy (shown as a dashed line at 0 energy. Figure (a) adapted from [42] and (b) adapted from [44].

cannot be fabricated easily, because a transistor needs a clear off state which cannot be reasonably achieved in a graphene system due to the non-existing band gap.

An additional effect of this linearity in the energy spectrum is the fact that graphene can be the host of massless Dirac fermions, but at a slower speed than in other systems described by linear dispersion relations. Hence the $K$ and $K'$ points are called Dirac points and since there are two distinct Dirac points in the Brillouin zone, there is an additional measure of degeneracy for each electron necessary – the valley degeneracy. In contrast to silicon valleys, where there are six valley states due to the cubic symmetry (discussed in section 2.2.1), there are only two valleys in graphene. This so-called pseudospin adds an extra degeneracy of two, which in combination with the spin-degeneracy results in a total of four degenerate energy levels. This four-fold degeneracy becomes apparent in the Hall effect where steps of $4e^2/h$ can be seen at high fields in the conduction[40].

All of those facts contribute to the appeal of graphene to be used in future research and technology. However, one of the largest setbacks would be if it proved to be impossible to engineer a band gap. Creating a band gap can be achieved by different means, of which the simplest method is to stack two graphene sheets to create a bilayer. During

the process of fabricating graphene monolayers (see section 2.1.6) bilayers can form naturally due to the nature of the scotch tape method. Bilayer graphene has a natural band gap and hosts some interesting physics, with one highlight being the emergence of superconductivity at a specific "magic" angle between the two sheets of graphene [22]. However, more often than not the two sheets are at an arbitrary angle and thus create a Moiré superlattice, which in itself is subject to a vast field of research [47–50].

### 2.1.2 Graphene Nano Ribbons

In addition to the methods above, there are of course other ways of engineering a band gap. One of them consists of constricting the flow of electrons and holes from two dimensions down to one by creating a narrow channel − a graphene nano ribbon (GNR). Not only does this confinement to one dimension create a band gap, it also can be the host of interesting physics depending on the edge termination of the GNR. When cutting a graphene sheet into ribbons, there can be three distinct edge terminations: armchair (AC) zigzag (ZZ) and a mor ore less regular mixture of both AC and ZZ. The first two originate from the honeycomb lattice of graphene and are the result of cutting the graphene sheet either parallel to the unit cell (AC) or at a 30° angle (ZZ) respectively. A more or less random, distorted edge termination is the result of cutting the sheet at any other angle (see figure 2.3).

The interesting physics specific to graphene can be observed when the termination is either a perfect armchair or a perfect zigzag edge. Calculating the full energy spectrum for both types of edge termination results in the band structures seen in figure 2.3. One key difference between the two edge terminations is that ZZ-GNRs are always metallic while AC-GNRs can be both metallic and semiconducting depending on their width on an atomic scale. An AC-GNR is metallic when the formula $N = 3M - 1$ (with $\{M, N\} \in \mathbb{N}$ and $N$ being the number of dimer lines) is satisfied. Further differences become apparent when considering electron-electron interactions which open a gap in the energy spectrum for ZZ-GNRs [44]. This results in a semiconducting GNR in which

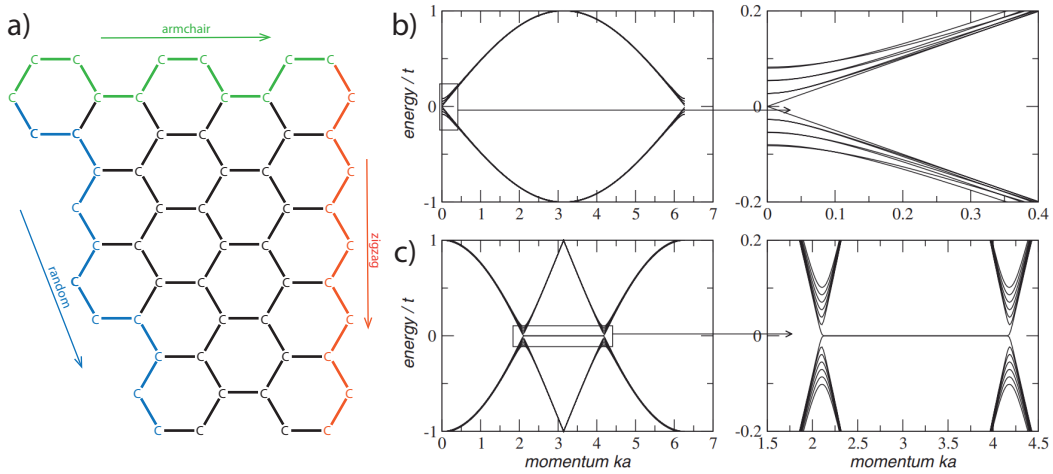


**Figure 2.3: Schematic of different edge terminations and band structure of nanoribbons.** (a) Schematic of a graphene honeycomb lattice indicating different edge terminations. The two distinct edge terminations armchair and zigzag stem from the lattice structure cut at specific angles, whereas the random direction is everything in between and shows no special features in electronic transport measurements. (b) and (c) Electronic dispersion of an armchair (b)) and a zigzag (c)) nanoribbon. The zoom-ins reveal a key difference in that zigzag nanoribbons have a zero energy ground state, therefore are metallic. If an armchair nanoribbons is metallic or semiconducting depends on the exact width of the nanoribbon. Depicted here is a semiconducting case. Figures (b) and (c) adapted from [42].

the low energy states are located on the edge of the ribbon. The nature of these edge states is special in that the spins align ferromagnetically (parallel) in a single edge and anti-ferromagnetically (anti-parallel) in relation to the other edge. This opens up the opportunity to engineer spin filters [51] and magnetic sensors [52]. In contrast to ZZ-GNRs, AC-GNRs do not show edge states and therefore cannot be used for the same applications as ZZ-GNRs. However, there are various proposals for using AC-GNRs for different purposes. One example was provided by Klinovaja and Loss, exploiting the unique band structure in combination with a rotating magnetic field and a superconductor to induce Majorana bound states [23]. These Majorana bound states can then be used as qubits in order to build the quantum computer.

### 2.1.3 Fabrication of Graphene Nano Ribbons

In order to see some the proposed effects in GNRs, the edge quality is of utmost importance, especially for the ZZ-GNR. Some effects in AC-GNRs do not require a perfect edge but the direction of the nanoribbon has to be accurate. Others, like quantized conductance, one of the underlying conditions for most of the previously mentioned effects, are only achieved in ballistic GNRs with perfect edges. Minor distortions or defects already suppress the quantization and give rise to other effects such as Coulomb blockade [53] or Anderson localization [54, 55]. Not only must the fabrication process of GNRs avoid any defects in the graphene, but the fabrication process also has to be highly selective in terms of the resulting edge configuration.

Most fabrication methods start with the exfoliation of graphene (described in more detail in section 2.1.6) on an appropriate surface. Usually, as a surface one can either choose silicon oxide ($SiO_2$) or hexagonal boron nitride (hBN), each with its own advantages and disadvantages, discussed in later paragraphs. After exfoliating and locating the graphene flake, GNRs can be fabricated by one of the methods described in the following paragraphs. The list is not complete, it just highlights the progress of GNR research and shows the two main approaches to the fabrication of GNRs − bottom-up and top-down approaches.

**Bottom-up approaches** The idea behind bottom-up approaches is to perform a synthesis of the final product using simple precursor molecules. In combination with the right catalysts, the synthesis is tightly controlled and highly repeatable. Both zigzag and armchair ribbons have been synthesised by Roman Fasel's group using *2,12-dibromo-14-(3',5'-dimethyl-[1,1'-biphenyl]-4-yl)-dibenzo[a,j]anthracene* [56] and *6,11-dibromo-1,2,3,4-tetraphenyltriphenylene* [57] precursor molecules respectively (see figure 2.4 for a visual representation). The precursor molecules self-align on a gold substrate and after two thermal cycles, a ZZ- or AC-GNR is formed depending on the precursor molecule. The synthesised GNRs are thermally stable, have a perfect

edge and − using the appropriate precursor molecule − any arbitrary width can be synthesised. The length of such ribbons is time dependent and is only limited by the amount of precursor molecules. The limiting factor is the fabrication of electrical contacts. First, the GNRs have to be transferred onto a non-conducting substrate, which is inefficient at best due to the strong interaction between the GNRs and the metal substrate. Secondly, contacting the synthesised GNRs with regular metal evaporation only yields Shottkey barriers and not the desired ohmic contacts. This strongly reduces the possibility to measure the effects described in section 2.1.2.

Another way to chemically synthesise GNRs is via epitaxial growth on a silicon carbide (SiC) substrate [58]. In this paper, Sprinkle et al. etched trenches into a SiC substrate,

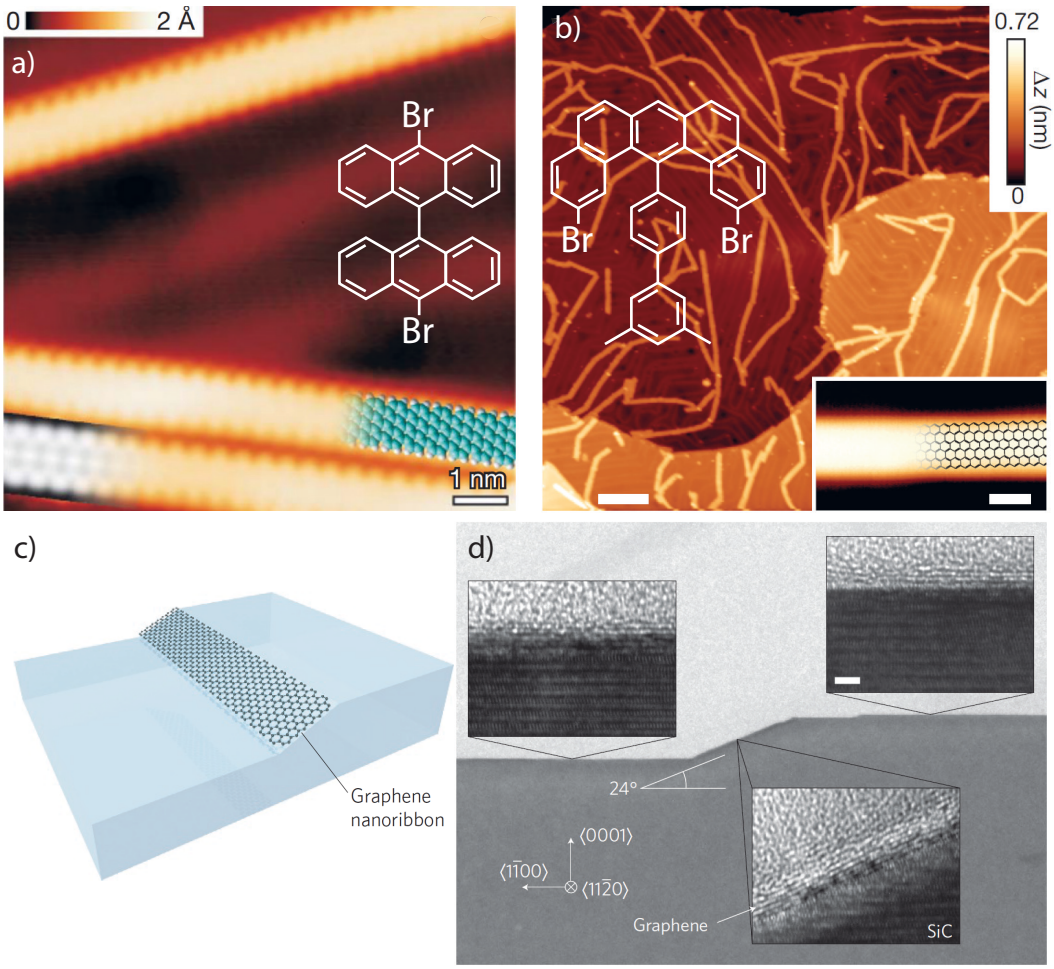


**Figure 2.4: Bottom up approaches.** (a) and (b) Chemical synthesis of graphene nanoribbons is achieved by using the respective precursors to form either armchair (a) or zigzag (b) nanoribbons. The resulting GNRs are well defined in width and can reach several 100 nm in length. The synthesis is on a gold surface, therefore contacting the GNRs is only possible after a transfer onto an isolating substrate. (c) and (d) Sublimation of an etched SiC substrate leads to Si evaporating of a trench facet leaving carbon on the surface which form a graphene layer. The width of the GNR is defined by the trench facet, allowing deliberate fabrication. However, the edge quality has not been further investigated. Figure (a) adapted from [57], (b) adapted from [56] and (c) adapted from [58].

then heating it within an inert atmosphere. Silicon starts to sublime on the trench facet due to the weaker bonding energy, and the remaining carbon atoms form a graphene layer on that same trench facet (see figure 2.4). The width is therefore determined by the trench walls and GNRs with widths as small as 40 nm have been produced with this method. Contacting the GNRs is more attainable because the GNRs do not have to be transferred after the synthesis and because of the isolating substrate. Since

the necessary trenches in SiC can be deliberately fabricated, this method is highly scalable. However, the edge quality has not been investigated and due to the nature of trench fabrication with standard photo-lithographic lift-off processes the roughness of the trenches is directly translated to the GNRs which results in non-perfect edges.

**Top-down approaches** Instead of synthesising a GNR from smaller precursors in bottom-up fabrication, top-down approaches start with a larger precursor than the size of the final product and shape the initial educt into the desired configuration. One of these approaches is to use photo or electron beam (e-beam) lithography, commonly known from semiconductor fabrication, both in academia and in large scale semiconductor industry. A photo or e-beam resist is spun on the initial educt and subsequently treated with patterned radiation in order to create a mask. Further processing steps can be either adding material to the educt − for example metallic contacts − or removing material to imprint the mask on the educt. The mask is later removed and only the processed material is left behind.

In the case of GNRs, graphene is exfoliated on a suitable substrate ($SiO_2$ or hBN) and an e-beam resist, usually PMMA, is spun over the whole chip. Other protective masks include silicon nanowires [59] and PS-PDMS copolymer [60], but due to strong limitations of both of those and the simplicity of using PMMA, they are usually not considered. Using standard e-beam methods, the desired shape of a GNR is patterned and after development, the resist should only cover the GNR and some graphene on both ends in order to guarantee that the GNR can be contacted with metal contacts (see figure 2.5 for details). Subsequently, the graphene is treated with an argon/oxygen ($Ar/O_2$) plasma, which etches graphene efficiently and only leaves the protected graphene. Although this fabrication method is rather straight-forward, both the roughness of a PMMA mask edge and the isotropic and efficient etching of an $Ar/O_2$ plasma result in a poor edge quality due to the roughness of the final product. Since the lithographic process determines both the shape and orientation of the GNR, the edge configuration is truly random unless the lithography is in perfect alignment with one

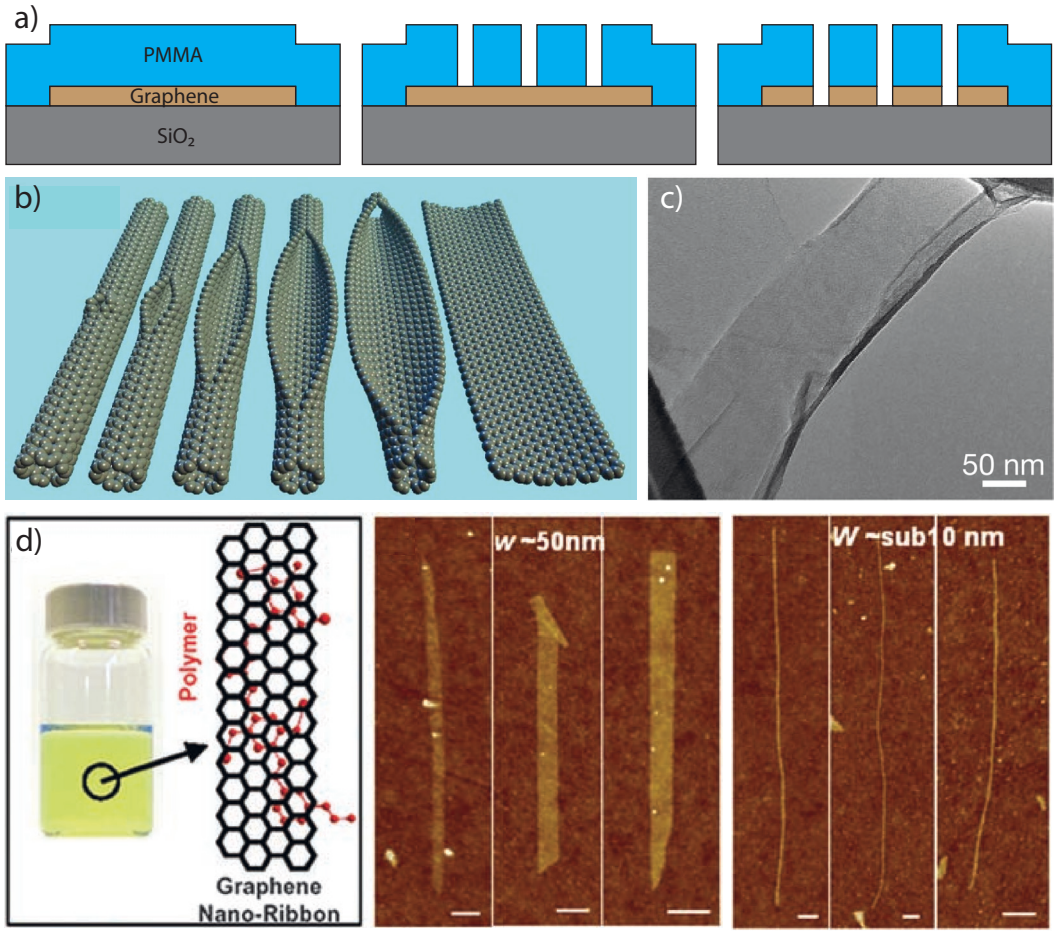


**Figure 2.5: Top down approaches.** (a) Top down approaches include the etching of graphene with an Ar plasma. Graphene is covered with a resist and after electron beam lithography, a mask of PMMA remains on the graphene. The unprotected areas are afterwards removed via an Ar plasma, resulting in GNRs with extremely rough edges and usually in a random crystal direction. (b) and (c) Unzipping carbon nanotubes is another way of achieving GNRs with rather smooth edges, but neither pure AC or ZZ termination. (d) Using a polymer as an intermediate substrate to create complexes containing nanoribbons results in GNRs with widths below 10 nm. All process involve many different chemicals leaving residues on the GNRs which impacts their electronic properties in a negative way. Figures (b) and (c) adapted from [61] and (d) adapted from [62].

of the principal axes of graphene (ZZ or AC) Even then, the roughness induced by the edge is larger than the unit cell. Furthermore, PMMA is known to leave residues on surfaces so that after the process, the remaining GNRs are not clean which can influence the quality of the measurements.

Unzipping carbon nanotubes (CNTs) is another way of fabricating GNRs (see figure 2.5). The process has been the centre of intense research due to the availability of

both single and multi-wall CNTs which allow for both single and multilayer GNRs. There are a wide range of methods to unzip carbon nanotubes including solution-based oxidation [61], controlled etching in PMMA [63], sonication [64], the usage of cobalt or nickel particles [65] and zinc sputtering [66]. All of those methods result in rather smooth edges but both electronic measurements and investigations with Raman and scanning tunnelling microscopy (STM) show that the edges are neither perfect AC nor ZZ. Similarly to lithographic processes using PMMA, the multitude of chemicals used in the process leave residues on the surface of the GNRs which affect the quality of the device in a negative way [67].

Another method is using a polymer as an intermediate substrate (see figure 2.5). This can be done by heating expandable graphite briefly to 1000 ℃ and dissolving the now expanded graphite in a solution of 1,2-dichloroethane (DCE) and a specific polymer (in this case: poly(m-phenylenevinylene-co-2,5,dioctoxy-p-phenylenevinylene) (PmPV)) [62]. By sonicating the solution, small graphene pieces stick to the PmPV and create a stable, lightweight complex which can be purified by removing larger pieces by centrifugation. The residual complexes are then transferred onto a $SiO_2$ chip and heated up to 400 ℃ in order to remove the remaining PmPC. The results are GNRs of varying lengths of up to 1 $\mu$m and widths ranging from 50 nm down to below 10 nm. Again, this method produces smooth edges, but apparently not enough because all GNRs were semiconducting and no magnetic ordering was observed. Additionally, residues of the chemicals used in the process are the probable cause for the low mobilities (100 - 200 $cm^s$/Vs) measured in experiments and therefore limit the usage of this process overall.

When comparing the above mentioned GNR fabrication methods, a pattern seems to emerge. Either GNRs have perfect edges but are difficult to process further or have distorted edges but are either scalable or easy to process further. The following section will discuss the use of a remote hydrogen plasma and the resulting effect of anisotropic etching, which (in theory) results in perfect zigzag edges with options for scalability

and no additional use of chemicals.

### 2.1.4 Hydrogen Plasma

Dry etching is a commonly used method to fabricate a wide range of samples [68–71]. Most etching methods avail a mask to etch the desired shapes because of the isotropic etching mechanisms of the chosen reagents. In the case of graphene, this method has already been used to form nanoribbons with an $Ar/O_2$ plasma (see section 2.1.3) with little success with regards to the orientation of the edges and therefore their quality. One way to achieve a high edge quality would be to have a process which etches one crystal direction in graphene more efficiently or even only etches in one crystal direction. This anisotropy has been studied in 1970 by McCarroll and McKee [24, 25]. They treated graphite surfaces with hydrogen, oxygen and nitrogen. Interestingly, their research showed that molecules do not etch graphite surfaces at any of the investigated temperatures (between 300 and 1200 ℃) but that the atomic counterparts of hydrogen and nitrogen (so-called radicals) do etch the graphite surface. Additionally, the etch pits do have a hexagonal shape which leads to the conclusion that both hydrogen and nitrogen radicals have a favoured edge direction, therefore etching anisotropically. Later studies found that hydrogen radicals create edge pits with zigzag edges [72] while nitrogen radicals create edges terminating in the armchair direction [73]. The main focus of this thesis will be on the use of a hydrogen plasma for ZZ-GNR fabrication, but parallels to the use of nitrogen plasma for AC-GNR fabrication will be highlighted.

A plasma is defined as an ionized gas [74]. By sufficiently heating a gas, molecules start to collide with enough energy so that electrons are being separated from their cores and decompose into charged atoms and molecules. This charge separation gives rise to new dynamics, especially a flow of current and an interaction with external magnetic fields. Another way to generate a plasma without heating it up to very high temperatures is to break the chemical bonds of molecules by providing enough energy

via a radio frequency (RF) or microwave (MW) source. By applying a rapidly varying electric field, electrons start to oscillate at the same frequency. Upon collision with neutral particles, the electrons transfer the energy to the neutral molecules. With enough energy transferred, bonds start to break and the gas becomes ionized. The ionized particles then break further bonds of neutral particles, which is a self-sustaining process, creating a plasma containing neutral molecules, radicals and ions.[1]

The energy needed to ignite the plasma within the boundaries of the work presented in chapter 3 is provided by a surface launcher (surfatron) which is wrapped around a quartz tube (the reaction chamber, see figure 3.5). By attaching a RF source to the two plates of the surfatron, an electric field between the two plates is created. The stray field outside the surfatron then couples to the gas molecules inside the reaction chamber and ignites the plasma as described in the previous paragraph. This method has the distinct advantage that no metallic parts are inside the reaction chamber which could contaminate the gas and that there is no possibility of the plasma corroding the electrode. Due to the size of the surfatron and the surface wave propagating along the tube, relatively long plasma columns are achieved without the use of external magnetic fields which makes the experimental setup compact and easy to operate.

As described above, hydrogen ($H$) radicals are used in order to create hexagonal etch pits with a ZZ-termination. By using a surfatron in combination with a hydrogen flow, a plasma with the following species is created: $H_2, H, H^+, H_2^+, H_3^+$, some higher vibrational states and electrons. In this so-called *direct* plasma regime, the abundance of energy provided by the surfatron allows the plasma to sustain itself which leads to a visible glow due to the ionization. In the *direct* plasma regime isotropic etching is induced by the highly energized ionized particles. Outside of the range of the electric field provided by the surfatron, the species inside the plasma start to recombine and the glow subsides until it is no longer visible. This gradient happens due to the different recombination rates of the species inside the plasma. The positively charged ions can

[1] Radicals are neutral atoms or molecules with an unpaired electron in the valence shell while ions are charged atoms or molecules

easily recombine with the negatively charged electrons, whereas the recombination of two radicals needs a third body in order to transfer the excess energy away. This mainly happens mainly at the walls of the reaction chamber where the material of the chamber has a huge impact on the recombination rate. Metals have a highly catalytic nature whereas the quartz used in this work has a relatively small $H$ radical recombination coefficient [75, 76]. This allows for a so-called *remote* plasma regime, where almost all charged species have recombined and only neutral molecules and radicals are present. The extent of both the *remote* and *direct* plasma regime can be tuned by adjusting the pressure, as more particles in the chamber allow for more collisions and recombination opportunities, and the position of the sample in the reaction chamber determines the etching process and speed.

How exactly hydrogen radicals lead to anisotropic etching has not been conclusively determined yet. While Horn et al. [78] describe a more general methyl group removal via $H$ radicals, Davydova et al. [77] incorporate the formation of ZZ-terminated edges in graphene. The first approach by Horn et al. is based on a $H$ radical reacting with a C-C double bond, breaking the $\pi$-bond and subsequently creating a new H-C bond (see figure 2.6). The intermediate step is an unpaired electron residing on the second carbon atom, which is subsequently paired with another $H$ radical. The repeated interaction with $H$ radicals leads to the breakage of the C-C bond, the removal of a methyl group and a newly formed C-C double bond due to some rearrangement within the group. As mentioned before, this approach is more general and cannot describe the anisotropy seen in experiments, since both AC- and ZZ-terminated edges possess double bonds. Moreover, it has been shown that anisotropic etching only starts at pre-existing defects in the graphene structure, indicating that the approach by Horn et al. is not stretching far enough to explain this phenomenon.

The other explanation mentioned above, put forth by Davydova et al. [77] is based on molecular dynamics simulations of a ZZ-GNR in a downstream $H$ plasma, which is exactly the experimental setup used in this work (see chapter 3). The process consists

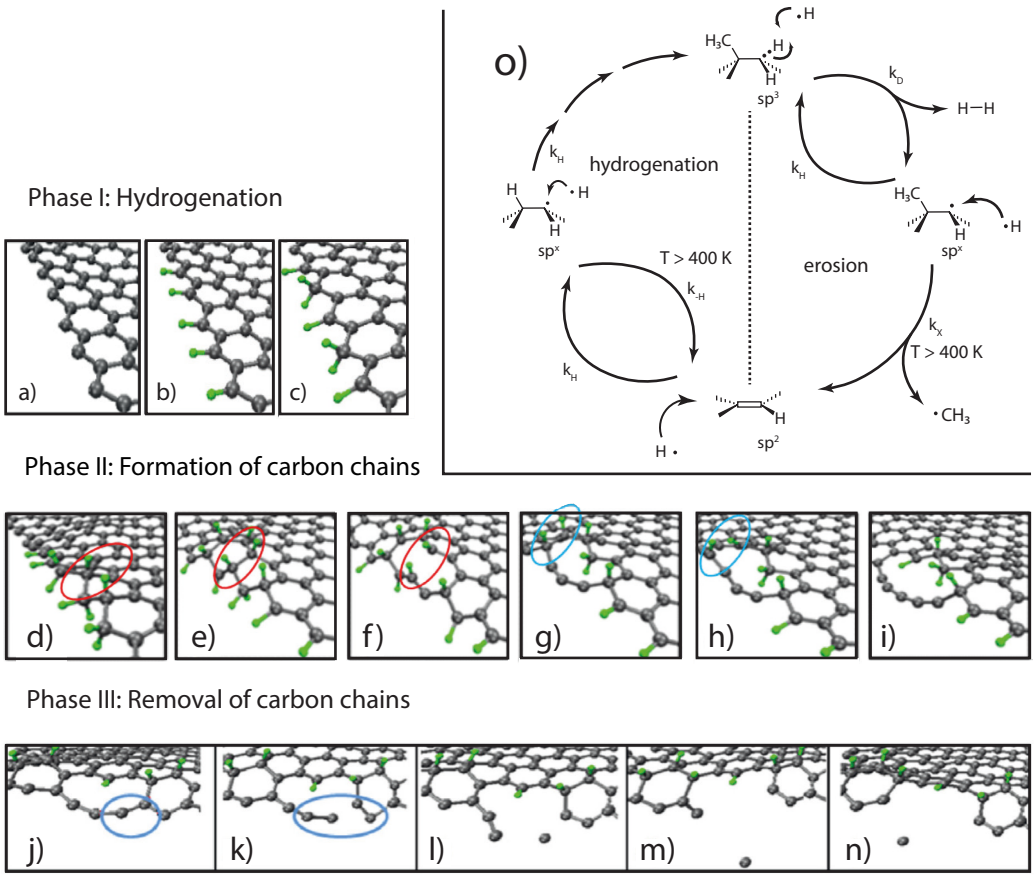


**Figure 2.6: Possible etching mechanism.** (a) - (c) In stage one, hydrogenation of pre-existing defects or zigzag edges weaken the C-C bonds of the lattice. (d) - (i) Due to the stress of $sp^2$ to $sp^3$ hybridised carbon atoms, a breakage of the second row of carbon atoms occurs, leaving dangling carbon chains. **j) - n)**. Sputtering of the carbon chains via $H$ radicals results in the removal of the chains, resulting in a newly formed zigzag edge. (o) Another approach of explaining $H$-Plasma etching is via the reaction of $H$ radicals with a C-C double bond via intermediate unpaired electrons. This process does not depend on the crystal direction and thus cannot explain the isotropic etching capability of a $H$ plasma. Figures (a)-(n) adapted from [77], (o) adapted from [78].

of three stages as shown in figure 2.6. In stage one, carbon atoms at defects or pre-existing ZZ-edges become hydrogenated due to the low energy barrier. The newly formed CH and $CH_2$ group lower the activation energy needed for hydrogenation of the second row of carbon atoms in the lattice. In phase two, the resulting mechanical stress due to local $sp^2$ to $sp^3$ hybridization in the second row of carbon atoms leads to the breakage of the C-C bonds between the first and second row. This results in free dangling carbon chains attached only on both of the ends. This happens multiple times and upon reaching a critical length, the $H$ radicals in the reaction chamber sputter the

dangling bonds in phase three. The result is a newly formed edge with ZZ-termination which is needed for ZZ-GNR experiments.

### 2.1.5 Raman Spectroscopy

In the previous section it was always assumed that a remote hydrogen (nitrogen) plasma creates perfect ZZ (AC) terminated edges. There are many ways to prove this assumption, some more elaborate than others. One way would be to measure transport through a device fabricated with this process and check for the respective signals (see section 2.1.2 for more details). However, this method involves many additional processing steps which take a long time for the production of each device and additionally, other effects could limit the visibility of the desired features. A more direct approach is to image the edge by high-resolution transmission electron spectroscopy (HRTEM) [79–82], scanning tunnelling microscopy (STM) [56, 83–85] or atomic force microscopy (AFM) [57, 86, 87]. All of those methods are mostly non-invasive [2] but require additional sample preparation (HRTEM, STM) or are highly time-consuming (AFM).

A more direct and simpler way of probing the edge configuration is to use Raman spectroscopy [88]. This method uses a single wavelength laser to excite a state and the succeeding relaxation emits a (or multiple) photon(s) at a slightly larger wavelength. The shift in wavelength or frequency then holds information about the structure of the material. In carbon particularly, the laser creates an electron hole pair and the resulting photon can scatter in three different ways, which manifests in three distinct peaks in the Raman spectrum of graphite and graphene: G, 2D and D.

**G-Peak** The peak at 1580 $cm^{-1}$ comes from the inelastic first order Raman scattering process during which a photon creates a virtual electron-hole pair at the Γ-point in the Brillouin zone (see section 2.1.1 for more details). The newly created electron or hole then scatters at a iTO or iLO phonon, recombining with the respective partner and

[2] A GNR edge can be depicted with HRTEM without damaging the GNR at low enough acceleration voltages. However, at higher operation voltages graphene edges have been rearranged [79].

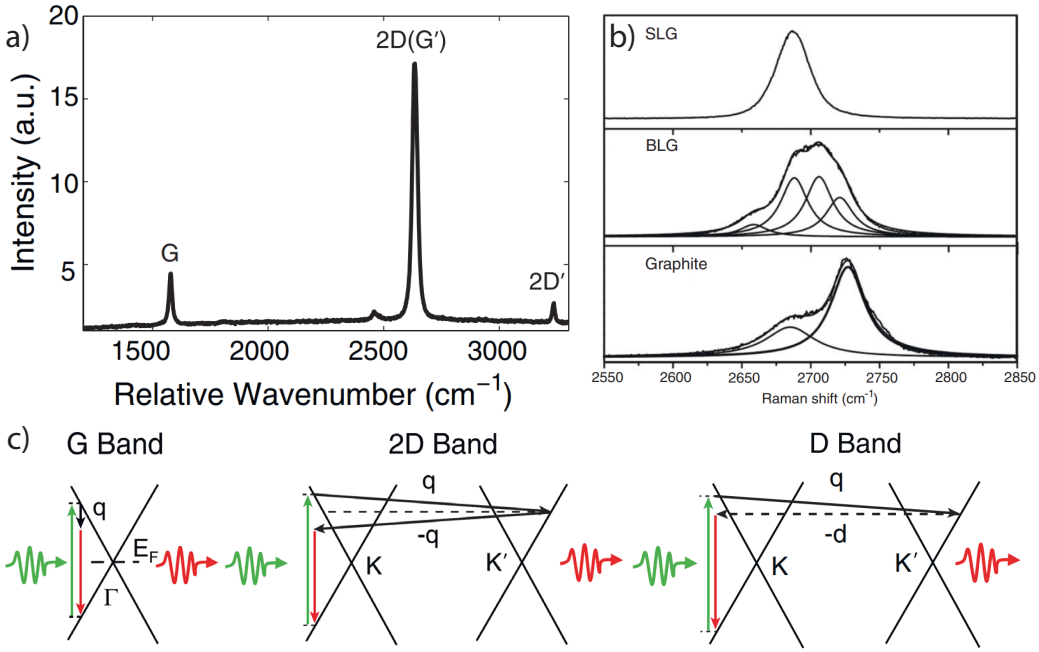


**Figure 2.7: Raman spectrum of graphite and graphene.** (a) Typical Raman spectrum expected from single layer graphene. (b) Detailed zoom-in of the 2D-peak for single layer graphene (SLG), bilayer graphene (BLG) and grapite. The shape of the 2D peak gives information due to the multiple scattering processes possible for the 2D peak depending on the amount of layers present. (c) Detailed schematics of the scattering processes leading to the Raman peaks for graphene. The G-peak is due to photon absorption and emission at the Γ-point, whereas both the 2D- and D-peak involve a momentum transfer via a phonon and defects. Figure adapted from [88].

emitting a photon at a slightly lower frequency than the incident photon. The involved iTO or iLO phonon has little to no momentum in $k$, meaning the process remains at the Γ-point. From the height of the G-peak, the thickness and, more specifically, the amount of layers in a given graphite sample can be deduced. Since the information about the amount of layers is decoded in the height of the G-peak, it needs proper calibration at first in order to be of quantitative value. The width of the G-peak holds further information about the strain and deformation of a graphene system. However, this holds only true if the G-peak is split into two sub-peaks, which happens neither in graphene nor graphite, but occurs in nanotubes for example.

**2D-Peak** Although the G-peak can be used to determine the number of layers in a graphene stack, it is more common to use the 2D-peak at $\sim 2700$ cm$^{-1}$ because of the

clear shape difference between single and bilayer graphene. While the 2D-peak of a single layer of graphene is a single Laurentzian, the 2D-peak of a bilayer graphene shows four peaks. Most of the time the four peaks are not clearly distinguishable, but the overall shape of the observed peak clearly indicates multiple peaks. The photon-phonon process behind the 2D-peak in graphene is doubly resonant due to the two scattering events happening sequentially and resonantly. First, a photon from the laser creates a virtual electron hole pair and either the electron or the hole scatters at an iTO phonon. This phonon now scatters to the corresponding $K'$ point, which is associated with a momentum $q$. The momentum component originates from the vibrational mode which can be described as an in-plane breathing motion of the carbon atoms in the honeycomb lattice. Since the process has to conserve momentum, a second phonon subsequently scatters back to the $K$ point with the momentum $-q$. The virtual electron and hole pair recombine and emit a photon with the corresponding energy difference, which is at a slightly lower frequency than the incident photon.

**D-Peak** The third prominent peak in the Raman spectrum of graphene is the peak near 1350 $\mathrm{cm}^{-1}$, which only appears when there is a defect in the system where the laser induces phonon movement. The process is almost identical to the 2D peak, starting with the creation of a virtual electron hole pair and the scattering of a phonon with momentum $q$. The difference lies in the backscattering which occurs at a defect site, not at the corresponding $K'$ point. The defect can be almost any lattice defect like $\mathrm{sp}^3$ carbon atoms, vacancies and most prominently an edge. Interestingly, the D-peak vanishes in the presence of perfect ZZ-edges due to the characteristics of the process itself. The momentum vectors for AC- and ZZ-edges differ by 30° and therefore, only the AC segment can give the phonon the necessary momentum kick in order to conserve the total momentum of the process. This allows for a quick determination of the edge configuration, because the D peak vanishes for ZZ edges. If the D-peak is visible, additional experiments which include the rotation of the polarized Raman excitation laser can reveal the amount of ZZ and AC components in a given edge [87].

### 2.1.6 Sample fabrication

Chapter 3 will discuss the etching of both graphite and graphene with a remote hydrogen plasma. In this section, the fabrication process of the samples used in this work is introduced as well as further steps for encapsulated GNR devices for transport measurements.

The first type of sample is cleaved graphite to determine the ideal parameters for anisotropic etching by means of remote hydrogen plasma. Here, graphite is cleaved by using the scotch tape method pioneered for graphene by Novoselov and Geim [21]. The scotch tape with the graphite pieces is afterwards pressed onto a clean $Si/SiO_2$ wafer piece with prepared numbered markers for easy identification. Due to the strong van-der-Waals interaction of graphite with the $SiO_2$, some of the graphite pieces will stick to the wafer surface during the removal of the scotch tape. This results in a separation of the layers of graphite, creating atomically flat and pristine graphite surfaces. This method presents a quick preparation of samples for the characterization of a remote hydrogen plasma and it is even statistically possible to create single layer graphene, which has been shown in the previously mentioned work [21].

However, graphene on $Si/SiO_2$ is known to be of poor quality for transport measurements due to the rough surface of $SiO_2$ [89–91] and the abundance of charge puddles [92–95]. In order to improve the quality of a graphene sample, hexagonal Boron Nitride (hBN) is commonly used as a substrate for graphene due to the flatness of the surface

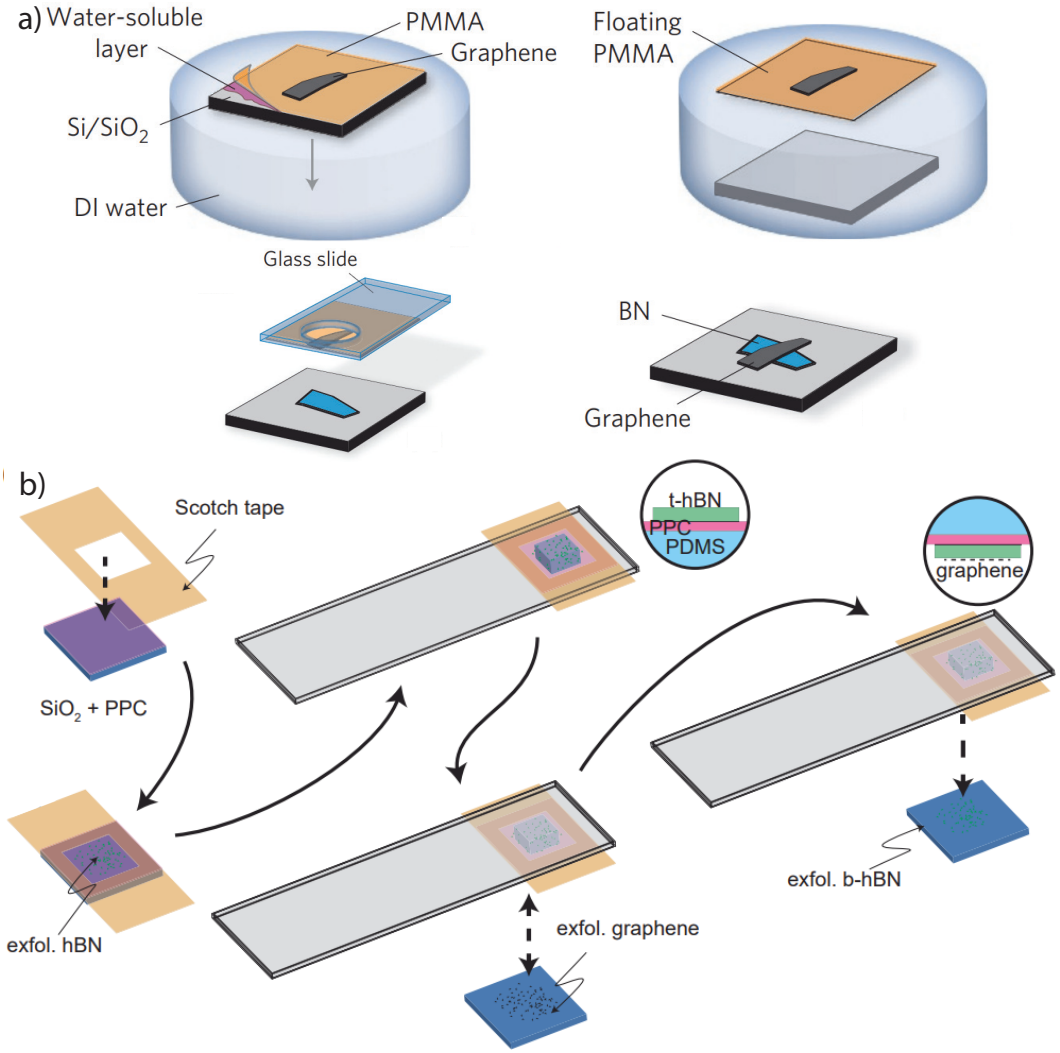


**Figure 2.8: Fabrication steps of an encapsulated graphene sample.** (a) Graphene is exfoliated using the scotch tape method onto a prepared polymer stack on a $Si/SiO_2$ wafer. The chip is put in water which dissolves the water soluble layer in the polymer stack. The graphene on the PMMA layer floats on top of the water and is picked up with a glass slide. Subsequently, the graphene is transferred onto a prepared hBN flake. (b) The enecapsulation is done by preparing an hBN flake on a with PPC coated wafer piece. It is spanned over a PDMS stamp and can then be transferred on the already fabricated hBN/graphene stack. Figure (a) adapted from [96], (b) adapted from [97].

and the fact that the lattice constant is almost the same as the lattice of graphene [98]. The fabrication starts by exfoliating hBN as shown in fugure 2.8. This is done by using the same scotch tape method as for graphene and graphite samples. This method generates hBN flakes of various thicknesses on the wafer from which a suitable candidate is chosen by means of optical microscopy. The ideal hBN flake has a large

area of uniform thickness and is well isolated from other flakes and potential other contamination. The exact height as well as the surface roughness can be identified by using atomic force microscopy. In order to deterministically place a graphene sample on the hBN flake, a modified scotch tape method is used. Here, graphite is exfoliated with a scotch tape and subsequently pressed on a polymer stack on top of a $Si/SiO_2$ wafer piece. The polymer stack consists of a PMMA layer with a water-soluble layer (usually polyvinyl alcohol (PVA) or dextrane) underneath. After finding a suitable graphene flake, the wafer piece is carefully placed on water, where the PVA or dextrane layer dissolves upon contact with the water. The graphene flake on top of the PMMA layer will float on the surface while the wafer piece sinks to the bottom. The floating PMMA piece then can be picked up using a glass plate with a hole and the graphene piece can be transferred on top of the hBN flake with a micromanipulator. PMMA is afterwards dissolved in acetone, leaving a hBN/graphene stack.

As described in section 2.1.4, anisotropic etching with a remote hydrogen plasma starts at existing defects. For samples investigated in chapter 3, round holes are etched into the graphene via $Ar/O_2$ plasma determined by an etch mask. After the removal of the etch mask, graphene samples are placed in the reaction chamber and treated with a remote hydrogen plasma, which resulted in hexagonal etch pits.

The same process opens an avenue for GNR fabrication. Here, graphene is etched in a remote hydrogen plasma for a small period of time and the resulting etch pits are investigated with an AFM. The straight edges are then used to align deterministically placed holes in an etch mask. $Ar/O_2$ plasma is again used for the primary holes and subsequently treated with the remote hydrogen plasma. After sufficient etch time, determined by repeated AFM measurements, two opposing hexagonal etch pits form a GNR between them. One of the main advantages of remote hydrogen plasma etching can be seen here. The smooth transition from bulk graphene to GNR caused by the fabrication process allows for high quality contacts to the bulk graphene and gives rise to an adiabatic transition from the two-dimensional transport regime in bulk graphene

to the one-dimensional GNR.

In order to preserve the fabricated GNR device, a second hBN flake can be placed on top of the current hBN/graphene stack. This can be done in a similar fashion to the above mentioned graphene transplantation, but with some key differences. Here, a $Si/SiO_2$ wafer is prepared with a thick layer ($\sim$ 1 $\mu$m) of poly-propylene carbonate (PPC) and a windowed scotch tape is placed around the edge of the chip (see figure 2.8). hBN is subsequently exfoliated via the scotch tape method on the PPC layer and a suitable flake is chosen with optical microscopy. The scotch tape holding the PPC is carefully peeled off the wafer and then placed on top of a polydimethylsiloxane (PDMS) cube, creating a stamp like structure. The hBN flake is then transferred on the hBN-graphene stack with a micromanipulator. Afterwards the assembly is heated up, which decreases the adhesion forces between the PPC and the PDMS cube. The stamp can then be removed and the left over PPC layer is dissolved in chloroform, resulting in a complete hBN-graphene-hBN stack.

Contacts to an encapsulated sample are slightly more involved than top-contacts for regular graphene samples. Here, an etch mask − which doubles as the actual contact mask − is prepared and the stack is then etched by an $SF_6/Ar/O_2$ plasma. The etching is fast and reveals the graphene in a one-dimensional fashion. The subsequent evaporation of contact metal (here Cr/Au) creates a low-resistive contact to the graphene, which is usually of higher quality than regular top-contacts. This is believed to be because of the electronic structure of graphene, where the electrons are flowing horizontally over the graphene.

## 2.2 Silicon

Silicon is one of the most common elements on earth and the impact of silicon on modern technology must not be underestimated. Almost all consumer electronics are built containing incorporated silicon chips and therefore, silicon has been one of the most widely studied elements. Almost every theoretical model for semiconductors has been applied to silicon, thus generating an almost endless library of knowledge on semiconductor materials. This research includes theoretical descriptions of the band structure [99–101] as well as proposals for electron spin qubits [102, 103]. Based on these theoretical works and also considering the first observation of Coulomb blockade in silicon in 1993 [104] and 1994 [105], huge advances in the field of silicon quantum applications have been made in the last 15 years starting with the observation of single electron quantum dots, research into spin blockade in double quantum dots and Rabi oscillation measurements. This laid the foundation for the fabrication of qubits − the quantum counterpart to the classical bit − in silicon and lead to the measurements of spin qubits in single quantum dot systems [106–108] as well as in coupled systems [109–112]. In parallel, silicon germanium (SiGe) as a material system for hole qubit applications has been explored both theoretically and experimentally in various geometries from classical heterostructures [13, 113, 114] to nanowires in different shapes [16, 115–118].

This section will focus on silicon metal-oxide semiconductor field effect transistors (SiMOSFET) and lays special focus on the mobility limiting factors present in this system.

### 2.2.1 Structure of Silicon

Silicon is along with carbon a group IV element with four valence electrons. The valence orbitals of silicon can undergo a $sp^3$ hybridization and form four covalent $\sigma$-bonds with other silicon atoms. At standard conditions, silicon crystallizes into a diamond cubic

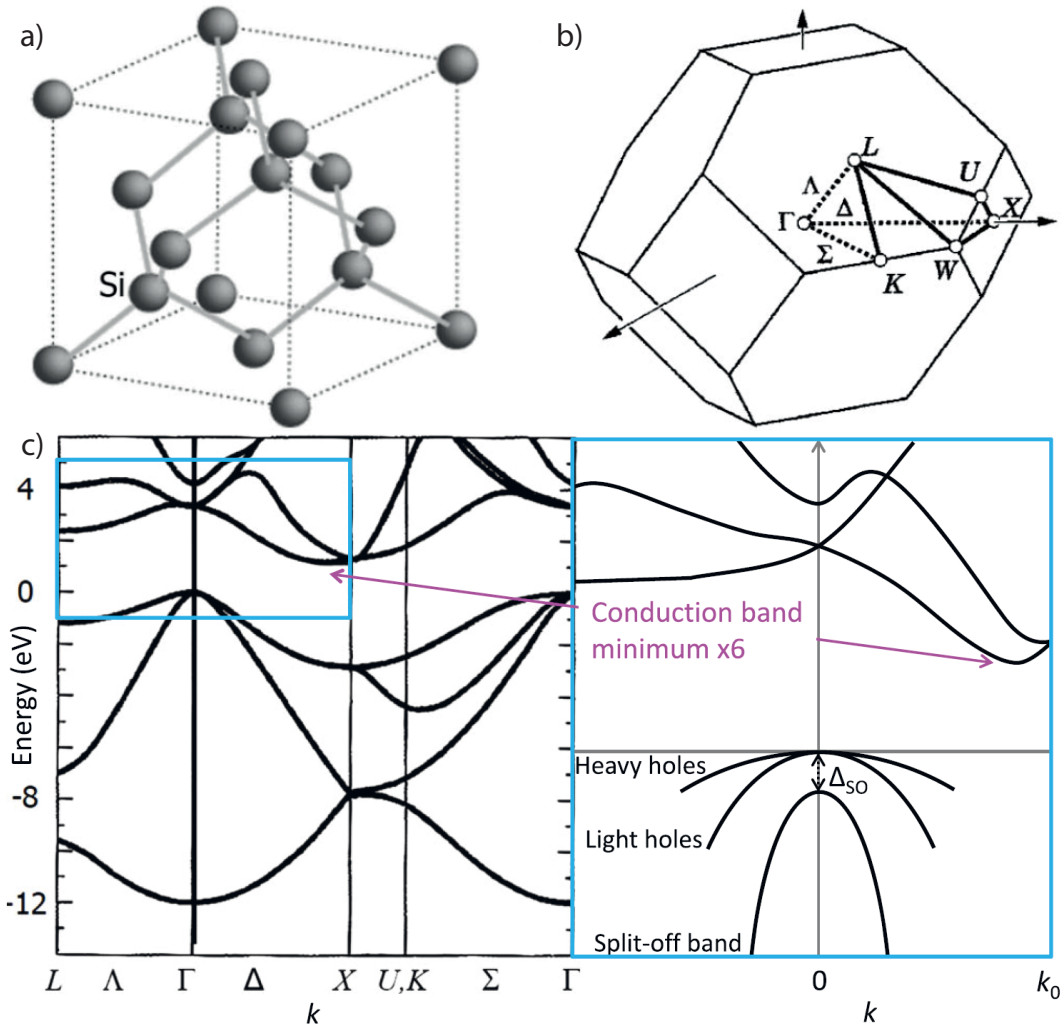


**Figure 2.9: Crystal structure of Si and calculated band structure.** (a) The most stable form of silicon is a diamond crystal structure, which is a derivative of the face-centred-cubic crystal. This structure is basically two intersecting face-centred cubic crystals shifted in all three directions by 1/4 of the width of the unit cell. (b) The three dimensional Brillouin zone illustrates the points and directions used in the band diagram. Of note is mainly the $\Delta$ direction, in which the valleys of silicon lie. (c) Calculated band structure of silicon which shows the indirect band gap and the resulting valley degeneracy of six at 0.85 $k_0$. The zoom-in highlights the position of the valleys and the three different bands in the valance band, namely the heavy-hole, light-hole and split-off band. These bands are important for hole applications in silicon. Figure adapted from [18].

lattice as seen in figure 2.9 from which the band structure can be calculated using empirical pseudopotentials [99] or a tight binding model [3]. The calculated band structure can be seen in figure 2.9. At a first glance, the band structure of silicon is not substantially different from other common semiconductors such as germanium (Ge) or

[3]Silicon can also form a two-dimensional hexagonal lattice (like graphene) called silicene [119].

gallium arsenide (GaAs), however, there are some key differences that make it unique, for example the heavy-light hole splitting and the indirect band gap. The most profound effects of its unique characteristics manifest in the electronic properties of silicon which is discussed extensively in the literature on silicon [18, 99, 120–123].

When analysing the properties of the top most-valence bands in silicon, the similarities to other group IV semiconductors become apparent. There are three valence bands that meet at the Γ-point, namely the light and heavy hole bands as well as a split-off band. The first two bands are of interest for hole applications because of the profound difference in the respective effective masses (0.16 for light holes and 0.46 for heavy holes). Simply said, the difference in effective mass directly translates to the size of the confinement needed for quantum applications such as quantum transport or spin qubits. The smaller the effective mass, the larger the structure can be for low occupation numbers of quantum dots [18, 122, 123]. The split-off band can usually be neglected because the energy difference between the uppermost valence bands and the split off band can be larger than the actual band gap of a given material. However, the split-off band in silicon needs some consideration due to the fact that the energy difference between the bands is determined by the spin-orbit interaction and scales with the fourth power of the atomic number. In silicon, the spin-orbit interaction is very weak resulting in an energy splitting of only 0.044 eV between the heavy/light hole bands and the split-off band [124].

The relatively small energy difference between the heavy/light hole bands and the split-off band is not the only difference between silicon and other group IV semiconductors. Another key property of the band structure of silicon lies within the lowest conduction band. In contrast to the direct band gap in for example GaAs, silicon possesses an indirect band gap. The minimum of the lowest lying conduction bands is located at 85% along the Δ direction between the Γ point the the $X$ point which is located on the Brillouin zone boundary [99, 120]. This has two major implications. First, the excitation of a carrier from the valence band into the conduction band requires not

only energy (for example a photon), but also a change in momentum. The change in momentum can be provided by phonons or by impurities in the crystal structure. Second, since there are six equivalent $X$ points in the Brillouin zone, there are six equivalent minima in the conduction band − so called valleys. In bulk silicon, these valleys are degenerate in energy, but depending on the charge carrier transport direction they still show slight differences between them. For the crystal direction [100], the dispersion can be written as

$$\epsilon\left(\vec{k}\right) = E_c + \frac{\hbar^2}{2m_0}\left[\frac{(k_x - k_0)^2}{m_L} + \frac{k_y^2}{m_T} + \frac{k_z^2}{m_T}\right]. \tag{2.9}$$

Here, $E_c$ is the energy of the conduction band at the minima $k_0$ and $k_x$, $k_y$ and $k_z$ the momenta in $x$, $y$ and $z$ direction respectively. $\hbar$ is the reduced Planck constant and $m_0$ represents the electron mass. The effective masses in the transverse directions $y$ and $z$ need to be equal according to symmetry and therefore they have the same effective mass $m_T$. The longitudinal effective mass $m_L$, however, can be different and for silicon this results in a large anisotropy ($m_T \approx 0.19$ and $m_L \approx 0.98$). Intuitively, one would expect transport to be highly anisotropic in silicon due to the different effective masses, but this only applies when transport is governed by a single valley. A measure of the anisotropy could be the mobility $\mu$, as it is directly influenced by the effective mass $m^*$:

$$\mu = \frac{e\tau}{m^*} \tag{2.10}$$

In this equation, $e$ represents the electronic charge of a single charge carrier and $\tau$ is the scattering time. A large effective mass would result in a low mobility, whereas a high mobility can be achieved if the effective mass is small. Irrespective of mass, all of the valleys contribute to the transport of charge carriers resulting in an isotropic conductance behaviour, which is in agreement with the cubic symmetry of the crystal structure.

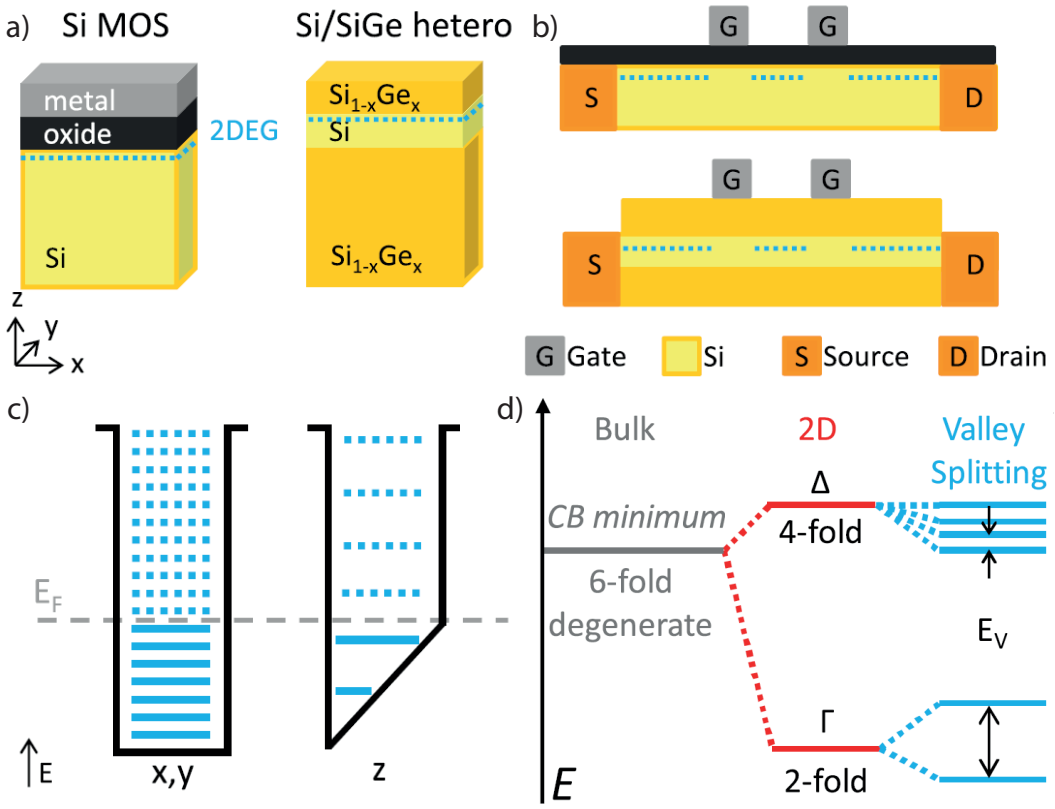


**Figure 2.10: 2-dimensional gasses in silicon structures and the resulting valley splitting.** (a) 2DEGs and 2DHGs can be formed in multiple ways in silicon structures. A voltage applied to a top gate induces a charge carrier layer either at the interface of Si and $SiO_2$ in SiMOS or at the interface of Si and SiGe in Si/SiGe heterostructures. (b) The resulting 2DEG or 2DHG can be formed using an additional set of gates to locally deplete the charge carrier layer in order to form quantum dots. (c) The resulting confinement in these structures before formation of quantum dots is mainly in the $z$ coordinate. This means that the energy levels are quantized in one direction whereas the charge carriers can flow freely in the other two directions because of the continuous energy levels. (d) The sixfold degenerate valley energy levels are split in two dimensional structures due to the induced strain into two groups. The two $z$-valleys shift to lower energies ($\Gamma$ group) whereas the $x$- and $y$-valleys shift to higher energies ($\Delta$-group). Further splitting is achieved with local electric fields, which strongly depends on the exact atomic structure of the sample resulting in different valley splittings for each device. Figures adapted from [18].

### 2.2.2 Interface engineering

The valley degeneracy of silicon can be lifted by reducing the dimensionality of the system [100]. This can either be done by sandwiching a silicon layer between two $Si_xGe_{1-x}$ layers [101, 125] or by creating a flat interface between silicon and silicon oxide ($SiO_2$) [124, 126–128]. For both systems, electrons (holes) can be accumulated

by applying a positive (negative) voltage with a metal top gate, thereby creating a 2-dimensional electron (hole) gas (2DEG and 2DHG respectively, see figure 2.10). As a side note, there is an additional possibility to create a 2DHG. It involves the fabrication of a stack made of Si-$SiO_2$ and $Al_2O_3$ as an additional layer on top [129]. By heating the sample to 400℃ in an argon atmosphere, negative charges start to accumulate at the $Si0_2$-$Al_2O_3$ interface. Because the sample has to be neutral, a positive mirror charge accumulates at the Si-$SiO_2$ interface, thus creating a 2DHG which is accessible via highly p-doped regions in the silicon substrate.

Back to the first two systems. Because of the lattice mismatch between the two layers in a silicon device (Si - $Si_xGe_{1-x}$ or Si - $SiO_2$), the resulting strain splits the six-fold valley degeneracy into two groups of states as shown in figure 2.10. The two z-valleys are shifted to lower energies (Γ-valleys) while the four $x$ and $y$ valleys slightly shift towards higher energies (Δ valleys). This first splitting is typically quite large, meaning somewhere approaching 200 meV so that only the lower two Γ states will contribute to the transport and degeneracy in the calculations. Further splitting of the lowest lying valley states usually happens within an electric confinement. In heterostructures such as Si/SiGe, this happens naturally due to the quantum well; in silicon metal oxide semiconductor structures (SiMOS), the splitting happens due to the applied top gate voltage which creates an electric field in the area of the conducting layer. Typical values for valley splitting are around 0.1 to 1 meV and mostly depend on the atomic structure at the conducting layer as far down as to an atomic length scale. Therefore, valley splitting is not something universal, but is different from device to device even on a single chip [130–135].

In order to be able to resolve the valley splitting, a high-quality device has to be fabricated. The quality of the sample is usually measured by factors such as the coherence times (for example $T_1$ or $T_2^*$), the mean free path of charge carriers and the mobility of the sample. While the determination of coherence times is usually a bit more involved both in the sample fabrication as well as in the actual measurements as

one needs quantum dots [13, 136], both the mean free path and the mobility can be extracted from relatively simple Hall bar measurements. The mean free path $\lambda$ can be calculated using the mobility $\mu$

$$\lambda = \frac{\hbar}{e} k_F \mu \tag{2.11}$$

with the reduced Planck constant $\hbar$ and the electron charge $e$ as pre-factors. The Fermi momentum $k_F$ depends on the density and considers not only spin degeneracy $g_s$, but also valley degeneracy $g_v$ in the following way

$$k_F = \sqrt{\frac{4\pi n}{g_s g_v}}. \tag{2.12}$$

This results in $k_F = \sqrt{\pi n}$ for valley degenerate semi-conductors such as silicon.

In order to calculate the mean free path of the charge carriers, one has to measure density $n$ and mobility $\mu$. The latter can be extracted from the longitudinal conductivity $\sigma_{xx}$ in a two-dimensional electron gas using

$$\mu = \sigma_{xx} \cdot \frac{1}{ne} = \frac{l}{w} \frac{I}{U_{xx}} \cdot \frac{1}{ne} \tag{2.13}$$

with the charge carrier density $n$, the current through the device $I$ and the longitudinal voltage $U_{xx}$. Additionally, since the mobility is a geometrically independent quantity, the width of the sample $w$ and the distance between the two voltage probes $l$ are included in the calculation.

The density $n$ required for the calculation of both the mobility and the mean free path can be extracted from the Hall voltage by analysing the Hall coefficient $R_{xy}$ within the classical regime

$$R_H = \frac{R_{xy}}{B} \frac{U_{xy}}{IB} = \frac{1}{ne}. \tag{2.14}$$

In this equation, the Hall resistance is calculated by taking into consideration the transversal Hall voltage $U_{xy}$, the current flowing through the device $I$ and the magnetic field $B$. In order to suppress possible effects of magnet hysteresis and possible offset

charges, one can take the slope of a Hall trace ($R_{xy}$ vs $B$) and calculate the density using

$$n = \left( \frac{dR_{xy}}{dB} e \right)^{-1}. \tag{2.15}$$

The density in a SiMOS sample behaves proportionally to the strength of the applied electric field generated by a voltage on a top gate. For accumulation type samples, a positive (negative) voltage has to be applied in order to accumulate electrons (holes) in the region below the metal top gate. This already highlights some of the parameters that have to be optimised for high mobility samples, namely the interface where the electrons (holes) accumulate and the influence of the metal stack on top of the sample. The impact on the quality in the latter case can be explained through the strain on the conducting channel, which can either increase or decrease the mobility of the charge carriers as described in the following section. Additional sample related quality influencers include background doping and remote charge impurities, discussed in more detail in the following section section.

### 2.2.3 Mobility limiting factors

According to theory, the scattering rate of different kinds of scattering is defined by screened scattering potentials [137]. The different types of scattering can be included into the square of the matrix element $\langle |U(q)|^2 \rangle$ for any given momentum transfer $\hbar q$. In combination with a dielectric response function $\epsilon(q, T, \Gamma)$ which is dependent on temperature $T$ and collisional broadening $\Gamma$ the scattering rate can be calculated using

$$\frac{1}{\tau(T,\Gamma)} = \frac{1}{2\pi\hbar E_F} \int_0^{2k_F} dq \frac{q^2}{\sqrt{4k_F^2 - q^2}} \frac{\langle |U(q)|^2 \rangle}{\epsilon^2(q, T, \Gamma)} \tag{2.16}$$

with

$$E_F = \frac{\hbar^2 k_F^2}{2m^*} \tag{2.17}$$

and

$$k_F = \sqrt{\pi n}. \tag{2.18}$$

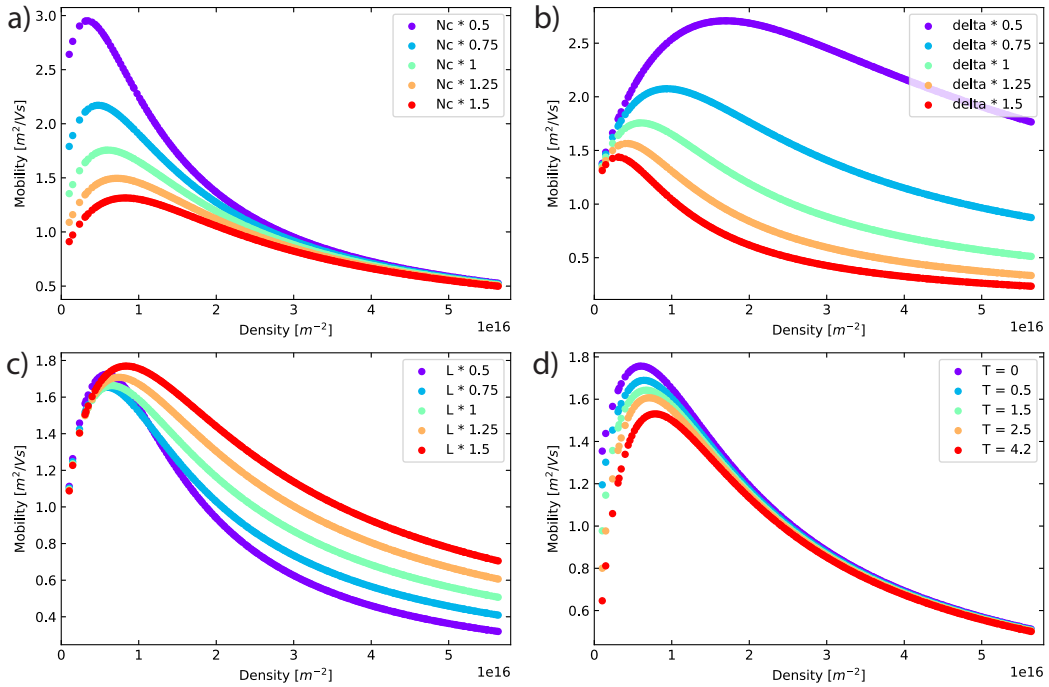


**Figure 2.11: $N_C$, $\Delta$, $L$ and $T$ dependence of the mobility in SiMOS.** (a) The density of interface charges has the most influence at low electron densities in the conducting channel. A higher $N_C$ results in more scattering events and thus in a lower mobility. (b) The rms height of the interface roughness denoted by $\Delta$ has a more pronounced influence on the mobility in the high density regime. This comes mainly from the fact that a higher density is directly translated to a higher electric field which pulls the charge carriers to the interface, where the interface roughness becomes the limiting factor. The rougher the interface is, the lower the mobility due to increased scattering. (c) The second parameter for interface roughness is $L$, the average distance between two roughness peaks. Again, the shorter the distance between two possible scattering events, the lower the mobility. (d) Temperature has as expected no impact in the high density regime because the interface does not change when varying the temperature. In this model, temperature variation affects the low density regime, in which the mobility is limited by interface charges.

$n$ denotes the density of charge carriers occurring in the conducting channel while $m^*$ represents the effective mass of those charge carriers. This formalism allows for an easy combination of multiple scattering types via the matrix element $\langle|U(q)|^2\rangle$ by simply adding unscreened potentials (Matthiesen's rule).

There are different types of scattering that can occur in semiconductors. The following paragraphs introduce the main contributors to scattering in 2DEGs and discuss their density and temperature dependence. This section is largely following [137].

**Coulomb scattering** There are three main contributors to Coulombic scattering: charges in the depletion layer, oxide charges and charge centres near the conducting channel. In this model, only the last contributor is considered as the impact of the other scattering mechanisms become negligible when considering the overall scattering rate and if the charges are present near the 2D layer. The matrix element for Coulomb scattering $\langle |U_C(q)|^2 \rangle$ then can then be written as

$$\langle |U_C(q)|^2 \rangle = N_C \left[ \frac{e^2}{2q\epsilon_0\epsilon_l} \right]^2 F_i^2(q) \tag{2.19}$$

with the vacuum permittivity being $\epsilon_0$ and the average dielectric constant at the interface $\epsilon_I = (\epsilon_{ox} + \epsilon_{Si})/2$. One of the extractable parameters can be found in the equation - $N_C$, the density of interface charges. Additionally, this equation includes a form factor $F_i$ which describes the finite extent of the wave function at the interface

$$F_i(q) = \frac{1}{(1 + q/b)^3} \exp(-qz_c) \tag{2.20}$$

with $z_c$ describing the distance between the center of the wave function and the interface. Usually this is considered to be 0 (as the wave function sits exactly at the interface), but there are considerable effects on $N_C$ when changing $z_c$ to finite numbers [137]. $b$ is the actual density $n$ dependent term in the matrix element for Coulomb scattering and includes the depletion charge density $N_{dep}$

$$b = \left[ \frac{12e^2 m_z}{\epsilon_0 \epsilon_{Si} \hbar^2} \left[ N_{dep} + \frac{11}{32} n \right] \right]^{1/3} \tag{2.21}$$

with $m_z$ as the effective mass in z-direction. $N_{dep}$ is a material parameter depending on the doping concentration and can be calculated using $N_{dep} = (N_A - N_D) d_{dep}$ with $d_{dep} \approx 1.2\mu m$ as the depletion layer thickness [138]. $N_A$ and $N_D$ are the acceptor and donor densities respectively. As shown in figure 2.11, the effect of Coulomb scattering can mostly be made visible at low charge carrier densities $n$. This is due to the fact that the number of interface charges is comparable to the number of charges in the

channel, therefore increasing the effect of one interface charge on the overall scattering.

**Interface roughness** Because the conducting channel is located at the interface of two different materials, here Si and $SiO_2$, the roughness of said interface has a large influence on the amount of scattering and therefore on the mobility. In this model, the matrix element for surface roughness contribution $\langle|U_{SR}(q)|^2\rangle$ can be written as

$$\langle|U_{SR}(q)|^2\rangle = S(q)e^2F_s^2 \tag{2.22}$$

There are two main aspects which define the surface roughness matrix element $\langle|U_{SR}(q)|^2\rangle$, namely the power spectrum $S(q)$ as well as $F_s$, which describes the electric field perpendicular to the interface.

The interface between Si and $SiO_2$ is never exactly perfect. Si is a diamond crystal and $SiO_2$ is of amorphous nature which creates a rather rank change of the crystal structure at the interface. Therefore, depending on the growth conditions, this creates a transition region of finite width. The region can be described using on of two different power spectra, either Gaussian or exponential. Intuitively, one would assume a Gaussian distribution, where the interface roughness is isotropic in all directions. However, studies on the interface have shown that an exponential power spectrum describes the interface more precisely than a Gaussian power spectrum [139, 140]. On an atomic picture this means that the interface cannot be defined by a smooth transition from Si to $SiO_2$ but instead shows step-like behaviour with finite step-sizes of a couple of nanometers. The power spectrum can then be described as

$$S(q) = \frac{\pi\Delta^2L^2}{(1+q^2L^2/2)^2} \tag{2.23}$$

in which $\Delta$ describes the root mean square (rms) height of the roughness' amplitude and $L$ denotes the average distance between two sequential roughness spots (correlation length). Both $\Delta$ and $L$ can be extracted from mobility curves when analysing the

density dependence.

The second parameter in the surface roughness matrix element $\langle |U_{SR}(q)|^2 \rangle$ describes the influence of the applied electric field in order to accumulate charge carriers in the conducting channel. In a nutshell: as the strength of the electric field increases, the charge carriers are getting pulled closer towards the surface and therefore the influence of the interface roughness becomes larger. Since the density and applied electric field are proportional to each other, one can write the influence of the electric field in terms of density $n$ and receive the following formula:

$$F_s = \frac{e}{\epsilon_0 \epsilon_S i} \left( N_{dep} + \frac{1}{2} n \right). \tag{2.24}$$

**Phonons** Another occasion for charge carriers to scatter is either via optical or acoustic phonons. Due to the crystal structure of silicon, optical phonons can be neglected because they are only present if there is a dipole in the system (for example in GaAs samples, where the crystal structure hosts two different types of atoms). For acoustic phonons, the scattering rate can be calculated using the following formula assuming single subband occupation [141–143]

$$\frac{1}{\tau_{phon}} = \left( \frac{\hbar^3 \rho s_l^2}{m_d D_{ac}^2 k_B T} \cdot W \right)^{-1}. \tag{2.25}$$

Here, $\rho$ indicates the density of silicon, $s_l$ the sound velocity in silicon, $m_d$ the effective mass of charge carriers parallel to the surface, $D_{ac}$ the deformation potential of acoustic phonons, $k_b$ the Boltzmann constant and $T$ the temperature. All mentioned parameters (except temperature) are literature values which means that phonon scattering is only temperature dependent in silicon samples. The density-dependent term $W$ describes the effective width of the conducting layer and can be written as

$$W = \frac{16}{3} \left( \frac{\epsilon_{Si} \hbar^2}{12 m^* e^2} \right)^{1/3} \cdot \left( N_{dep} + \frac{11}{32} n \right)^{-1/3}. \tag{2.26}$$

Broadly speaking, the density dependence of the mobility limited by phonon scattering has a power of $-1/3$, so the lower the density, the higher the mobility. This dependence can usually be observed at high temperatures (around 300 K) [143]. For lower temperatures, phonon scattering quickly becomes negligible due to the temperature dependence of the scattering rate of $T$ (see equation 2.25. In experiments, usually a temperature dependence of $T^{-1.75}$ is observed in consequence of the strong contribution of intervalley phonon scattering. The higher energies of said phonons give rise to a stronger temperature dependence than the theoretically predicted $T$ dependence [142]. Generally, only the lowest valleys are occupied and therefore, a $T$ dependence is still viable to use in the calculations for higher temperatures. In the case of low temperature physics such as the experiments in chapter 5 (and already below 77 K, the temperature of liquid nitrogen), phonon scattering can be neglected due to the temperature dependence.

**Strain** In silicon, strain has different effects depending on the charge carrier [144]. When it comes to holes, strain influences the band structure to the extent that the heavy-hole and light-hole bands change shape and shift in energy so that the two bands are now split at the Γ-point in the Brillouin zone. In this particular case, biaxial compressive strain increases the band splitting, thereby reducing the scattering rate and raising the overall mobility. In the case of electrons, strain does not change the band structure very much, but has a rather significant influence on the valley splitting. Usually, the Γ- and Δ- valleys in a 2DEG in silicon are split by a large energy difference (around 200 meV) with the effect that inter-valley scattering is not possible at low temperatures. On the one hand, biaxial compressive strain raises the energy of the two lower-lying Γ-valleys, thus increasing the rate of inter-valley scattering and subsequently reducing the mobility. On the other hand, biaxial tensile strain can increase the mobility due to the lowering of the Γ-valley energies, thereby reducing inter-valley scattering.

In gate-induced silicon 2DEGs, strain is caused by the material of the top gate when cooling down a sample to low temperatures. Common top gate materials are palladium

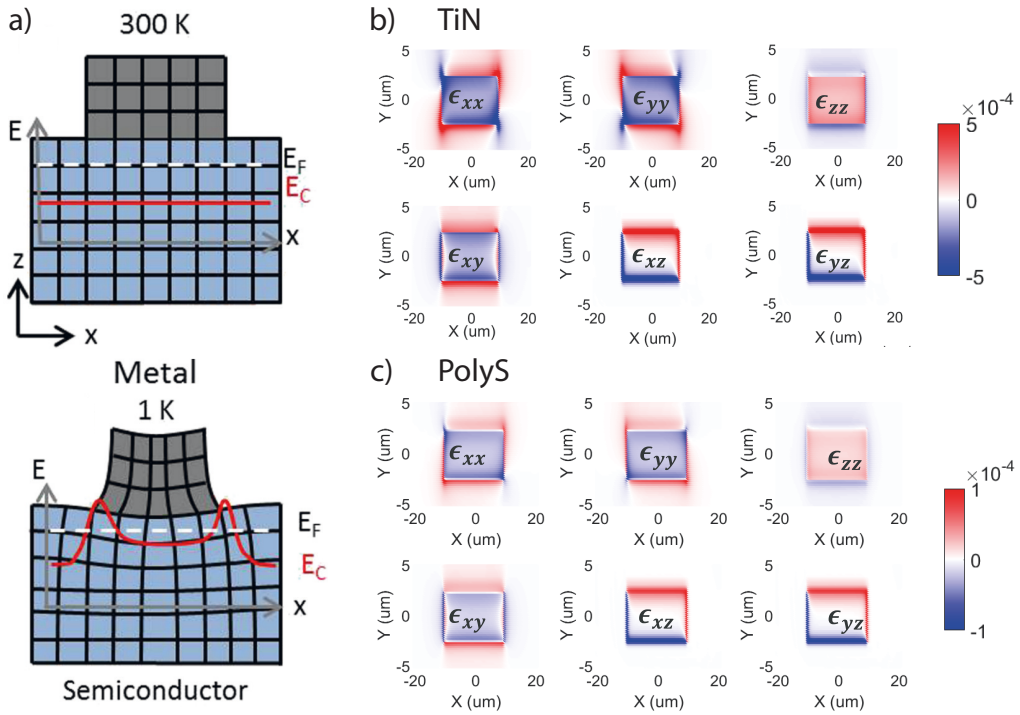


**Figure 2.12: Strain induced by different top gate materials in SiMOS.** (a) Because the top gate material and silicon have different crystal structures and lattice dimensions, strain is induced in the sample at lower temperatures. Usually, the conducting channel is located far enough away from the Si - metal interface so that the strain is relieved in the region of the 2DEG. If the distance is now small enough for strain to have an influence, it can even form unwanted quantum dots in the conducting channel. (b) and (c) Calculated strain influence of two top gate materials. This model calculates a five times stronger induced strain with TiN than Si, therefore decreasing the possible peak mobility, as discussed in chapter 5. Figure (a) adapted from [144], (b) and (c) are provided by Fahd A. Mohiyaddin from IMEC, Belgium.

(Pd), Aluminium (Al), titanium nitride (TiN) and poly-silicon (PolyS, highly doped silicon). The latter two materials are used as top gates in chapter 5 and have been studied both experimentally and theoretically. In this paper, it has been shown that TiN induces biaxial compressive strain and due to the sub-10 nm thick oxide, the strain induced by the top gate has a huge impact on the mobility of the sample compared to the same sample with a PolyS top gate (see figure 5.7). The calculated compressive strain induced by the TiN top gate is around half an order of magnitude larger than the one induced by the PolyS top gate, which reduces the mobility by approximately 60%. The full model and explanation can be found in chapter 5.

**Crystal structure dependent terms** There are additional scattering mechanisms but all of them are either irrelevant due to the crystal structure of silicon or so small in comparison to the main two scattering mechanisms (Coulomb and interface scattering) that they can be neglected. Examples for crystal structure dependent scattering mechanisms are piezoelectric and alloy scattering [145]. Both scattering processes come with two different atom types in the unit cell which creates a dipole moment and thus local electric fields. If strain is applied to the system, these local electric fields are disturbed, thereby causing scattering of charge carriers at these centres. This effect is rather small but can be a large intervening factor if temperatures are low enough, so whenever other scattering processes are being suppressed. The scattering rate can be described by the following formula

$$\frac{1}{\tau_{pz}} = \frac{\sqrt{m^*}e^2K^2k_bT}{2^{3/2}\pi\hbar^2\epsilon_0\epsilon_{Si}}E^{-1/2} \tag{2.27}$$

which shows that the scattering rate is inverse proportional to the square root of the energy $E$ and thus to density [145]. $K$ denotes the dimensionless electromechanical coupling constant, connecting the piezoelectric constant $e_{pz}$ with the dielectric constants $\epsilon_0$ and $epsilon_{Si}$ and the longitudinal elastic constant $c_l$ in the following way

$$\frac{K^2}{1-K^2} = \frac{e_{pz}^2}{\epsilon_0\epsilon_{Si}c_l}. \tag{2.28}$$

However, as mentioned above, this effect is only relevant for polar semiconductors, most prominent in wurzite crystals like the II-VI semiconductor CdS where the dipole is large enough to make the piezoelectric scattering rate the dominant effect.

Another dipole effect is alloy scattering which again only occurs in compound materials like GaAs or CdS. Alloy scattering happens when the regularity of the crystal structure is disturbed by a random dislocation of an atom or a swap of two atoms. The effect is rather small, but can have an impact under certain circumstances [146, 147].

### 2.2.4 Dielectric response function

In equation 2.16, the dielectric response function $\epsilon(q, T, \Gamma)$ has been introduced. This function combines the effects of the interaction potential $V(q)$, the compressibility of an electron gas $g_0$ and the correction of the response function for two-dimensional systems and low electron density $G(q)$ in the following way if collisional broadening is neglected and at $T = 0$ [137]

$$\epsilon(q, 0, 0) = \alpha \left(1 - \frac{\alpha - 1}{\alpha} \sqrt{1 - {}^{4k_F^2}/_{q^2}} \theta(2k_F - q)\right) \tag{2.29}$$

where

$$\alpha = 1 + V(q) g_0(q, T = 0, \Gamma = 0)(1 - G(q)). \tag{2.30}$$

$\theta$ represents a step function, if $\theta = 0$ for $q < 2k_F$ and $\theta = 1$ for $q \geq 2k_F$. When analysing the integral boundaries in equation 2.16, one can reduce equation 2.29 to $\epsilon = \alpha$, neglecting the correction term inside the brackets as they always go to 0 inside the boundaries. The correction term $G(q)$ and the interaction potential $V(q)$ can be written as

$$G(q) = \frac{q}{4\sqrt{q^2 + k_F^2}} \tag{2.31}$$

$$V(q) = \frac{e^2}{2\epsilon_0 \epsilon_{Si} q 0} F(q) \tag{2.32}$$

with the form factor $F(q)$ described in terms of $b$ from equation 2.21

$$F(q) = \frac{1}{16} \left(1 + {}^{\epsilon_{ox}}/_{\epsilon_{si}}\right) \frac{8 + 9{}^{q}/_{b} + {}^{3q^2}/_{b^2}}{\left(1 + {}^{q}/_{b}\right)^3} + \frac{1}{2} \cdot \frac{1 - {}^{\epsilon_{ox}}/_{\epsilon_{si}}}{\left(1 + {}^{q}/_{b}\right)^6}. \tag{2.33}$$

The compressibility $g_0$ is equal to the density of states in a two-dimensional electron gas $\rho_F = {}^{2m^*}/_{\pi\hbar^2}$ multiplied with a temperature dependent correction term and an additional smearing $p(E)$

$$g_0 = \frac{2m^*}{\pi\hbar^2} \cdot \left(1 - 0.268 \left(\frac{T}{E_F}\right)^{1/2}\right) p(E). \tag{2.34}$$

The smearing can be written with a characteristic value of $\sigma \approx$ 1-2 meV. $\sigma$ represents the amount of band tailing in a given system and in this equation, it suppresses the mobility at low electron densities [137, 148]. Explicitly one gets

$$p(E) = 0.5 \cdot \mathrm{erfc}\left(\frac{E}{\sqrt{2}\sigma}\right). \tag{2.35}$$

$\sigma$ can also be calculated using the theory by Arnold, who describes the band tailing with a fluctuating potential caused by the remote background charges $N_C$ [148]. With $d$ denoting the average distance between electrons and the Coulomb centres one can write $\sigma$ as follows

$$\sigma^2 = N_C \frac{\left(e^2\lambda\right)^2}{\left(d^2 8\pi^2 \epsilon_0^2(\epsilon_{ox} + \epsilon_{Si})\right)^2}. \tag{2.36}$$

The screening wavelength is inverse proportional to the density of states $D(E) = D_0 p(E)$ at the energy level $E$ and is written as

$$\lambda(E_F) = \frac{\epsilon_0 \epsilon_{Si}}{2\pi e^2 \cdot D(E)}. \tag{2.37}$$

The mobility of a two-dimensional electron gas is temperature-dependent. In this model, temperature is added to the equation by making the compressibility temperature-dependent as can be seen in equation 2.34. The effects on the scattering rate have been calculated by Gold and Dolgopolov [149], which results in the following series

$$\frac{1}{\tau(q, T, \Gamma = 0)} = \frac{1}{\tau(q, 0, 0)} + \sum_{n=1}^{\inf} \frac{1}{\tau_n(q, T, 0)}. \tag{2.38}$$

with $1/tau(q, 0, 0)$ as described in equation 2.16 and

$$\begin{aligned} \frac{1}{\tau_n(q, T, 0)} = \frac{n+1}{2\pi\hbar E_F} \int_0^{2k_F} dq \frac{q^2}{\sqrt{4k_F^2 - q^2}} \frac{\langle |U(q)\rangle|^2}{\epsilon(q, T = 0, \Gamma = 0)^2} \\ \cdot \left(\frac{V(q)(1 - G(q)\Delta g_0(q, T, E_F)}{\epsilon(q, T = 0, \Gamma = 0)}\right)^n. \end{aligned} \tag{2.39}$$

$\Delta g_0 = g_0 - \rho_F$ stands for the reduced compressibility, which only includes the

temperature-dependent correction. Those temperature-dependent correction terms regarding the equation 2.16 are almost equal to the original term for $T = 0$, except for some additional factors, and for temperatures below 5 K the first two terms dominate. Above 5 K, other scattering mechanisms have to be included. For silicon, this would mainly be the electron-phonon scattering term because lattice vibrations are not negligible any more.

Combining all of the mobility-limiting factors, the dielectric response function as well as the temperature-dependent terms, we receive a well-rounded model which gives insight into the quality of the interface as well as the quality of the sample in general. The application of this model is discussed in chapter 5 in which high mobility SiMOSFET samples have been investigated at various temperatures.

# 3 Anisotropic Etching of Graphite and Graphene in a Remote Hydrogen Plasma

D. Hug, S. Zihlmann, M. K. Rehmann, Y. B. Kalyoncu, T. N. Camenzind, L. Marot and D. M. Zumbühl

*Department of Physics, University of Basel, CH-4056 Basel, Switzerland*

K. Watanabe, T. Taniguchi

*National Institute for Material Science, 1-1 Namiki, Tsukuba 305-0044, Japan*

This chapter was published in *npj 2D Materials and Applications* **1**, 21 (2017)

## 3.1 Abstract

We investigate the etching of a pure hydrogen plasma on graphite samples and graphene flakes on $SiO_2$ and hexagonal Boron-Nitride (hBN) substrates. The pressure and distance dependence of the graphite exposure experiments reveals the existence of two distinct plasma regimes: the *direct* and the *remote* plasma regime. Graphite surfaces exposed *directly* to the hydrogen plasma exhibit numerous etch pits of various size and depth, indicating continuous defect creation throughout the etching process. In contrast, anisotropic etching forming regular and symmetric hexagons starting only from preexisting defects and edges is seen in the *remote* plasma regime, where the sample is located downstream, outside of the glowing plasma.

This regime is possible in a narrow window of parameters where essentially all ions have already recombined, yet a flux of H-radicals performing anisotropic etching is still present. At the required process pressures, the radicals can recombine only on surfaces, not in the gas itself. Thus, the tube material needs to exhibit a sufficiently low H radical recombination coefficient, such as found for quartz or pyrex. In the *remote* regime, we investigate the etching of single layer and bilayer graphene on $SiO_2$ and hBN substrates. We find *isotropic* etching for single layer graphene on $SiO_2$, whereas we observe highly *anisotropic* etching for graphene on a hBN substrate. For bilayer graphene, anisotropic etching is observed on both substrates. Finally, we demonstrate the use of artificial defects to create well defined graphene nanostructures with clean crystallographic edges.

## 3.2 Introduction

Graphene nanoribbons (GNRs) have emerged as a promising platform for graphene nano devices, including a range of intriguing quantum phenomena beyond opening of a confinement induced band gap [11, 26, 51, 150, 151]. In armchair GNRs, giant Rashba spin-orbit coupling can be induced with nanomagnets, leading to helical modes and spin filtering [23]. Further, Majorana fermions localized at the ends of the ribbon were predicted in proximity of an s-wave superconductor [23]. Zigzag ribbons, on the other hand, were proposed as a promising system for spin filters [151]. Theory showed that electronic states in zigzag ribbons are strongly confined to the edge [26, 150, 151], recently observed in experiments [152–155]. Further, edge magnetism was predicted to emerge at low temperatures [26, 44, 51, 150, 156], with opposite GNR edges magnetized in opposite directions. High quality, crystallographic edges are very important here, since edge disorder suppresses magnetic correlations [44] and tends to cause electron localization, inhibiting transport studies. GNRs fabricated with standard electron beam lithography (EBL) and $Ar/O_2$ etching typically exhibit pronounced disorder [157–163], complicating transport studies.

Fabrication methods creating ribbons with clean crystallographic edges were recently developed, including carbon nanotube unzipping [61, 64], ultrasonication of intercalated graphite [62], chemical bottom up approaches [56, 57], anisotropic etching by nickel nanoparticles [164], or during CVD processing [165–167], or carbothermal etching of graphene sheets [168–171]. Here, we use a hydrogen (H) plasma etching technique [25, 72, 172–174] because it allows precise, top-down and on-demand positioning and tailoring of graphene nanostructures. Such nanostructures can easily be designed to spread out into larger graphene areas incorporated into the same graphene sheet, thus providing for a relatively easy way to make electrical contacts.

## 3.3 Results and Discussion

In this work, we investigate the anisotropic H plasma etching of graphite surfaces in dependence of the gas pressure and the sample - plasma distance (see Methods). We find that the etching characteristics can be divided into a direct and a remote plasma regime. In the *direct* plasma regime, the sample is placed within the glowing plasma, and surfaces show many hexagons of various sizes indicating a continuous defect induction throughout the etching process. In the *remote* plasma regime, on the other hand, the sample is placed downstream of the glowing plasma, and etching occurs only from preexisting defects which makes the fabrication of well defined graphene nanostructures possible. Further, we have prepared single layer (SL) and bilayer (BL) graphene flakes on $SiO_2$ and hexagonal boron nitride (hBN) substrates and exposed them to the remote H plasma. We observe a strong dependence of the anisotropy of the etch on the substrate material. SL graphene on $SiO_2$ is etched isotropically, confirming previous findings [172, 175], whereas we observe highly anisotropic etching of SL graphene on hBN [176], producing very regular and symmetric hexagonal etch pits. Anisotropic etching of SL graphene on hBN offers the possibility to fabricate diverse graphene nanostructure with well defined edges (e.g. GNRs) and allows investigation of their intrinsic electronic transport properties.

### 3.3.1 Distance Dependence

We first investigated graphite flakes, allowing for rather simple and fast processing. The graphite specimen [177] were cleaned by peeling with scotch tape and subsequently exposed for one hour to a pure H plasma at a temperature $T = 400\,^{\circ}\mathrm{C}$ and a distance $d$ from the end of the surfatron. We first present the distance dependence of the H plasma process. Figure 3.1a shows AFM topography scans for exposures of one hour at four different distances at constant pressure $p = 1\,\mathrm{mbar}$. At the larger distances, etch pits of monolayer step height are created upon plasma exposure, exhibiting a

regular hexagonal shape and demonstrating a strongly anisotropic process [25, 72]. All observed hexagons exhibit the same orientation. From previous studies, it is known that hexagons created by exposure to a remote H plasma exhibit edges pointing along the zigzag direction [25, 72]. As the sample is brought closer to the plasma, significantly more etch pits appear, often located at the border of existing holes, sharing one common hexagon side (see Figure 3.1a, $d = 42\,\mathrm{cm}$). For the closest position $d = 37\,\mathrm{cm}$ – unlike the larger distances – the sample is located within the visible plasma glow region, resulting in a strong and several layers deep scarring of the entire surface.

To quantitatively study the distance dependence, we evaluated larger images to gather better statistics and plot histograms showing the number of holes as a function of diameter, see Figure 3.1b-d. The overall number of holes obviously increases strongly with decreasing sample-surfatron distance $d$. For small distances, a wide distribution of diameters is seen, ranging from several 100 nm down to nearly vanishing hexagon size, suggesting that new defects serving as etch seeds are created throughout the exposure time. The width of the hole diameter distribution is given by the anisotropic etch rate and the exposure duration in this regime. For larger $d$, on the other hand, the few holes seen have comparable diameters, consistent with etching proceeding predominantly from preexisting graphite defects, without adding new defects. This results in a narrow width of the distribution of hole sizes. As previously reported [25, 72, 172], exposure to energetic ions seems to create defects, while exposure to hydrogen radicals appears to result in anisotropic etching and growth of hexagons centered around preexisting defects and borders.

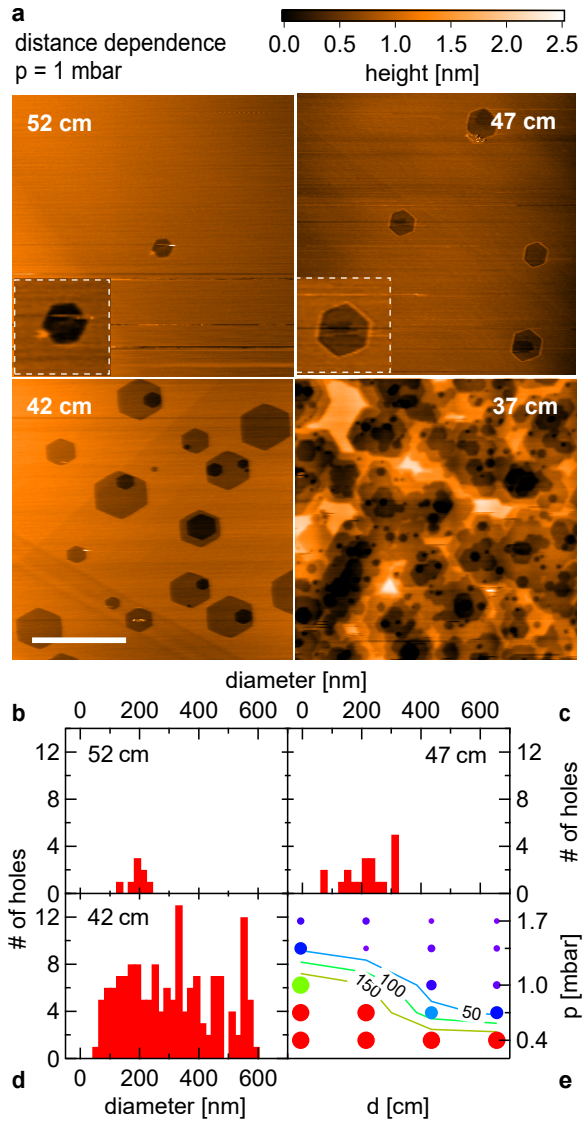


**Figure 3.1: Distance dependence of graphite exposures**
(a) AFM images (tapping mode) of graphite surfaces for various distances $d$, as labeled, all exposed to the plasma for 1 h at $p = 1$ mbar and $T = 400°C$, all shown on the same color scale. Main panels are $3 \times 3\,\mu m^2$, scale bar is $1\,\mu m$, insets (dashed white boxes) are $0.25 \times 0.25\,\mu m^2$. Slight hexagon distortion at 42 cm is an imaging artefact due to drift. See SOM for the complete distance and pressure matrix. (b-d) Histograms obtained from $10 \times 10\,\mu m^2$ scans, showing the number of holes against hole diameter (bin size 20 nm). (e) The size of the circle markers corresponds to the width of the diameter distribution. The color indicates the number of holes, with red corresponding to large number of holes. For samples located within the glowing plasma (red circles), a lower bound of 300 holes and a minimum width of distribution of diameter of 600 nm is shown.

### 3.3.2 Pressure Dependence

Next, we turn to the pressure dependence. In Figure 3.2a, AFM topography images are shown at four different pressures $p$ at constant distance $d = 52\,\text{cm}$. The number of holes increases with decreasing pressure, similar to decreasing distance, giving rise to etch pits of monolayer step height at intermediate pressures. At the highest pressures, however, no etch pits were observed, in strong contrast to the lowest pressure, where ubiquitous and deep etching is seen, demonstrating the strong influence of $p$. Analyzing the etch pits using histograms confirms that $p$ and $d$ have a similar influence on the etching process (compare Figure 3.2b, c with Figure 3.1b-d). Figure 3.1e summarizes the histograms of all investigated graphite samples (see supplementary online material (SOM)), using color to represent the number of holes, while the size of each marker is proportional to the width of the distribution of hole diameters. A clear correlation between the number of holes and the width of the distribution is seen: the largest circles are red, while the small circles are purple.

The analysis of the graphite exposure data leads to two qualitatively different types of processes: the *direct* and the *remote* plasma regime. In the *direct* plasma regime (large, red circles, Figure 3.1e), the sample is located directly within the plasma discharge region, hence exposing it to large densities of radicals and ions, capable of inducing defects throughout the exposure, giving a broad hole diameter distribution. In the *remote* plasma regime (small, purple circles, Figure 3.1e), on the other hand, the sample is positioned outside, downstream of the plasma generation region, where ions have recombined and only a residual flux of radicals is present. There, etching proceeds predominantly from preexisting defects and edges, leaving the basal planes mostly untouched. In this regime, a narrow distribution of hole diameters results, centered around the diameter given by the anisotropic etch rate and the exposure time. See SOM for more details.

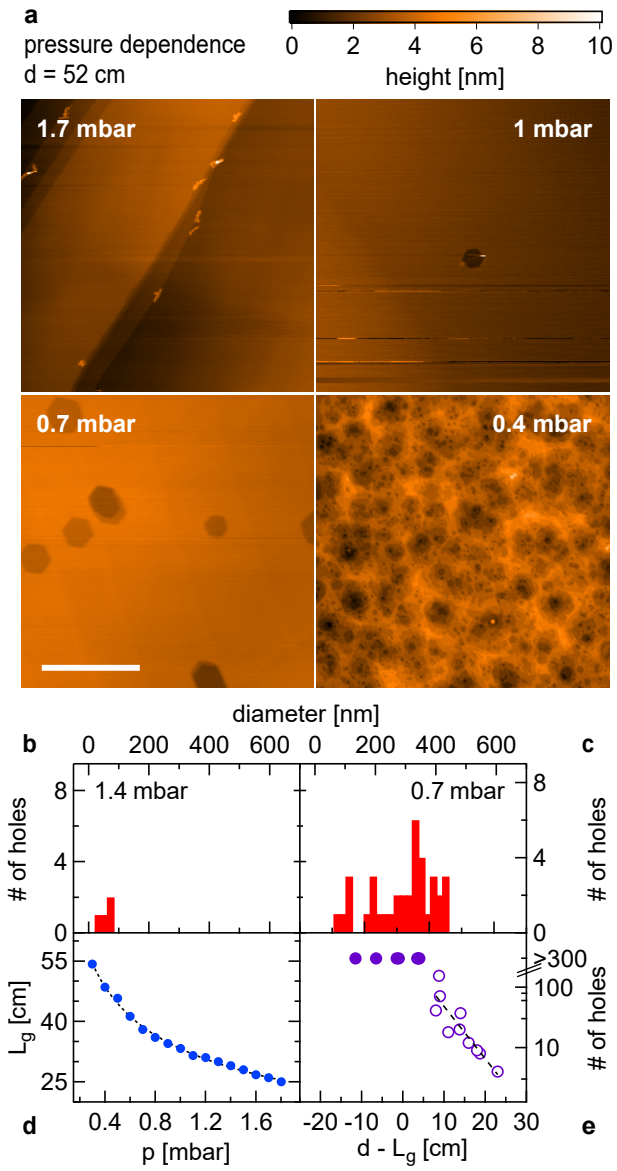


**Figure 3.2: Pressure dependence of graphite exposures**
(a) AFM images (tapping mode) of graphite surfaces for various $p$, as indicated, exposed for one hour at $d = 52\,\text{cm}$ and $T = 400°\text{C}$, all shown on the same color scale. All panels are $3 \times 3\,\mu\text{m}^2$, scale bar is $1\,\mu\text{m}$. (b,c) Histograms from $10 \times 10\,\mu\text{m}^2$ scans, displaying the number of holes against hole diameter (bin size 20 nm) for $p$ as labeled. (d) Length $L_g$ of the optically visible plasma as a function of $p$. The dashed curve is a $1/\sqrt{p}$ fit. (e) Number of holes versus distance from plasma edge $d - L_g$. A lower bound of 300 holes is given for the heavily etched cases where an exact hole-count was not feasible. The dashed black line is an exponential fit to the data with $< 300$ holes with 1/e decay length $\sim 5$ cm.

Further, there is an intimate connection between distance and pressure: lower pressure results in a longer gas mean free path and therefore a larger average distance for recombination in the diffusive gas. This results in a larger length of the plasma column $L_g(p)$, measured from the edge of the visibly glowing plasma to the surfatron, see Figure 3.2d. Thus, changing the pressure with fixed sample position modifies the distance between sample and plasma edge. Hence, it is useful to introduce an effective distance $d' = d - L_g(p)$, the distance from the sample to the edge of the glowing plasma. Thus, $d' \lesssim 0$ roughly marks the direct plasma regime while $d' \gg 0$ signifies the remote plasma regime. Reactive particles are generated inside the plasma column and start recombining once they have left the plasma generation region.

The reaction kinetics in low temperature H plasmas are highly non-trivial despite the relatively simple chemical composition [178]. Nevertheless, it is well known that at the pressures used here ($p \sim 1\,\mathrm{mbar}$), the predominant radical decay mechanism is surface mediated association rather than gas collisions. Two colliding H atoms require a third body to carry away the excess energy for association to occur [179]. However, under the present conditions, three body collisions are very unlikely, thus leaving only the surface assisted process (which also leads to surface heating [76]). Recombination of ions, in contrast, can also occur through an additional collisional channel, in absence of a surface. Which species – ions or radicals – decay on a shorter length scale downstream of the plasma edge thus depends on both the surface properties and gas parameters. For anisotropic etching without defect creation, a flux of H radicals in absence of ions is needed, as previously reported [25, 72, 172], thus requiring the ion density to decay on a shorter length than the radicals.

The surface attenuation of H radicals thus plays an important role, and was previously studied [75, 76]. Some glasses such as pyrex or quartz – as used in our experiments – were identified as a materials with a low recombination coefficient, particularly compared to some common metallic surfaces such as stainless steel and aluminum. This weak surface attenuation can open a downstream window offering a flux of H radicals

while essentially all ions have already recombined, as desired and achieved here, see e.g. Figure 3.1b, 3.2b and 3 (below). Nevertheless, the etch rate in the downstream window was observed to decrease slowly over long periods of time, reaching a vanishingly small etch rate after more than 100 hours of plasma exposure. The elevated temperatures in the furnace may enhance impurity migration towards the surfaces of the tube, possibly amplifying the surface attenuation of H radicals. Larger anisotropic etch rates were observed when utilizing higher purity quartz tubes manufactured from synthetic fused silica [180], supporting the assumption of the role of impurities. High impurity content and even small amounts of metallic deposition on the tube wall give wave damping due to dielectric losses and result in an enhanced decay of radicals.

To study the decay of reactive species, we note that the ion flux is proportional to the number of holes created. We find a roughly exponential decrease of the number of holes with distance, see Figure 3.2e and SOM, with a 1/e decay length of about 5 cm. The anisotropic etch rate, on the other hand, is related to the flux of H radicals. We extract the anisotropic etch rate, defined as the growth per unit time of the radius of a circle inscribed to the hexagonal etch pit, averaged over a number of holes, shown in Figure 3.4a. Only the largest set of hexagons of each exposed graphite sample were evaluated to obtain the etch rate, since smaller holes might not have etched from the beginning of the exposure. As expected, the anisotropic etch rate is largest for small distances, falling off quickly with increasing separation from the plasma edge. There is also an apparent pressure dependence, with larger pressures tending to give lower etch rates, see Figure 3.4a. Given only two or three points along the d-axis for each pressure, and only few holes for some parameter sets ($d$, $p$), a reliable H-radical decay length cannot be extracted from these data. A theoretical estimate gives an H-radical decay length of $\sim 12\,\mathrm{cm}$, see SOM, in agreement with observations in Figure 3.4a, and longer than the ion decay length of 5 cm, as observed. The etch rates we extract are a few nm per min at 400 °C, consistent with previous reports [72, 172].

### 3.3.3 Substrate Dependence

Next, we study the plasma exposure of SL and BL graphene exfoliated onto a $SiO_2$ substrate using the established tape method [21]. We patterned disks using standard EBL and reactive ion etching with an $Ar/O_2$ plasma, resulting in circular graphene holes which were subsequently exposed to the remote H plasma in the regime where H radicals but essentially no ions are present, as determined from the graphite experiments. BL graphene grows regular hexagons with parallel sides (see Figure 3.3b), as expected from the graphite results. SL graphene, on the other hand, displayed mostly round holes (see Figure 3.3a), though some weakly developed, irregular hexagonal shapes are also occasionally seen. Further, several additional, not EBL defined holes appear on the SL after exposure, all smaller than the EBL initiated etch pits. After a second plasma exposure, the number of holes on the SL increased further, indicating generation of new defects, while only EBL defined holes appear on the BL. Note that the SL and BL regions shown in Figure 3.3a and b are located on the same graphene flake, ensuring identical plasma conditions.

In addition, the average hole diameter on SL is visibly larger than on the BL (Figure 3.3a and b) after the same exposure time, indicating a faster etch rate on SL. Thus, SL on $SiO_2$ is more reactive when exposed to the plasma and no longer anisotropic when exposing . This is consistent with previous reports [172, 175, 176], and is suspected to arise from charge inhomogeneities in the $SiO_2$ substrate [181–183] or other $SiO_2$ surface properties. A broad range of plasma parameters in the remote regime were investigated for SL and BL samples on $SiO_2$, giving qualitatively similar results (isotropic SL etching). The etch rate for SL and BL on $SiO_2$ is shown in Figure 3.4b. For the SL samples, only the EBL defined holes were evaluated, ignoring the plasma induced defects, since these do not etch from the beginning of the exposure. Clearly, for all plasma parameters studied, SL exhibits a significantly larger etch rate compared to BL [72, 175], as already visible from the AFM images in Figure 3.3a and b.

The temperature dependence of the etch rate for both SL and BL on $SiO_2$ is shown in

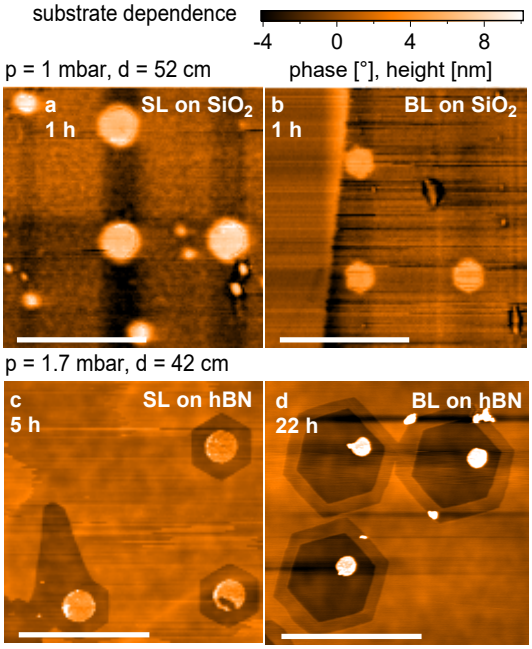


**Figure 3.3: Substrate dependence of SL/BL graphene** (a,b) AFM phase contrast images of a SL (a) and BL (b) section of the same flake on a $SiO_2$ substrate, etched for 1 h at $T = 450\,°C$. Round holes of 50 nm diameter were defined before H-etching. AFM topography image of a SL (c) and BL (d) flake on hBN etched for 5 h and 22 h, respectively. Holes of 200 nm (SL) and 100 nm (BL) were defined before etching. For (d) the color scale values are divided by four. The scale bars on all images are 1 $\mu$m.

Figure 3.4c. The etch rates are strongly reduced at temperatures far above and below the process temperature, consistent with previous reports [72, 175], and consistent with reported hydrogen recombination rates on quartz increasing dramatically with temperature [184].

To study the substrate dependence, we use high-quality hBN crystals as grown in Ref. [185]. SL and BL graphene were aligned and deposited onto areas covered with several 10 nm thick hBN lying on a $SiO_2$ substrate, following the recipe of Ref. [96]. Then, the same fabrication steps were repeated as before to fabricate circular graphene holes. Figure 3.3c shows an AFM topography image of SL graphene on hBN after 5 h of remote H plasma exposure. Clearly, very regular and well aligned hexagonal holes are visible, indicating a highly anisotropic etch. Etching of the hBN substrate by the H plasma was not observed, see profiles in SOM. We observed this anisotropic SL graphene etching on hBN in more than 10 samples demonstrating the high reproducability of the process.

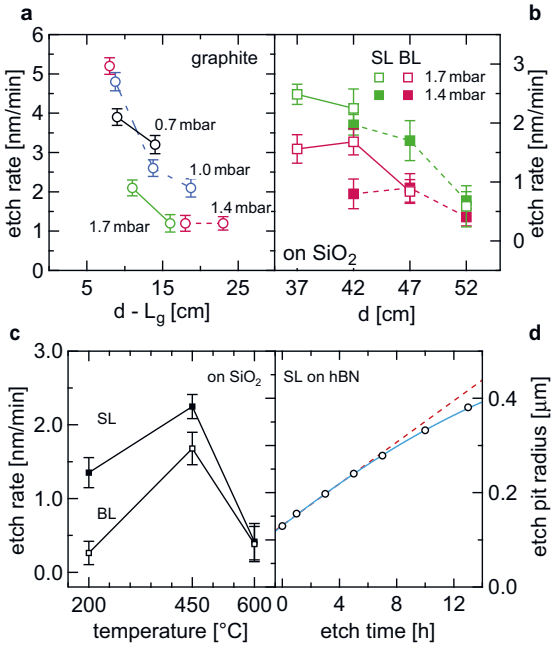


**Figure 3.4: Anisotropic etch rates** (a) Graphite anisotropic etch rate versus distance from plasma $d - L_g$ for several configurations. (b) Etch rate of SL and BL on $SiO_2$ at indicated parameters. (c) Temperature dependence of the etch rate of SL and BL samples on $SiO_2$. Error bars are standard deviations. (d) Average radius of a circle inscribed to the hexagonal etch pits as a function of exposure time for SL on hBN. Several etch pits were evaluated in order to obtain average size and standard deviation, where the latter is smaller than the diameter of the marker circle. The dashed red line is a linear fit to the points at $\leq 5$ h, the blue curve is a tanh-fit shown as a guide for the eye.

In Figure 3.3d we present an AFM topography image of a BL graphene flake on hBN which was exposed to the H plasma for 22 h. We observe anisotropic etching of the BL flake with a slightly higher etch rate for the top layer ($\sim 0.3$ nm/min) compared to the bottom layer ($\sim 0.2$ nm/min), leading to a staircase-like structure at the etch pit borders. As seen in Figure 3.3d, the hexagons in the bottom and the top layer are of the same orientation. We note that the bottom layer is on hBN while the top layer is laying on graphene. The situation of the top layer is comparable to the SL etching on a graphite surface, where it was shown that the edges of the hexagons are aligned with the zigzag direction of the graphite lattice [25, 72]. Since the bottom layer exhibits hexagons oriented in the same direction as the hexagons emerging on the top layer, this further confirms that the etching of SL graphene on hBN is yielding etch pits oriented along the zigzag direction. The ribbon defined by the two left hexagons

in Figure 3.3d has a width of about 20 nm, demonstrating the fabrication of nanoscale graphene structures with a remote H plasma.

The size of the SL hexagons as a function of exposure time is shown in Figure 3.4d. A linear fit (dashed red) is clearly over estimating the etch rate for long exposure times, deviating from the data by several standard deviations for the longest times. This hints towards either an insufficient H atom collection mechanism as the etch pits are growing larger or an aging effect of the tube as discussed above.

Raman spectroscopy on SL and BL samples on hBN was performed before and after H plasma etching. The $D$ and $D'$ disorder peaks were not seen (see SOM), both before and after H plasma etching. This suggests that neither defect formation nor hydrogenation [186–189] is occurring in the bulk 2D during plasma etching, taking into account the annealing of the sample during the cool down phase [187], opening the door for high quality electrical properties.

The EBL defined circles stand very clearly visible in the center of the hexagons as an elevated region, as seen in Figure 3.3c and d, growing in height but not diameter upon further H plasma exposure. These discs appear also away from the graphene flakes directly on the hBN, wherever circles were EBL/Ar/$O_2$-plasma defined. However, these elevated regions are also observed to shrink in height in ambient conditions. For a better understanding of the composition and behaviour of these surface structures, further investigations are required, which are however beyond the scope of this work. In addition, the adhesion between graphene and hBN often appears to be rather poor. Graphene flakes of several micrometres in length seem to be tilted with respect to the circular pillars induced by EBL. AFM tip forces or elevated temperatures may have shifted the flakes from their original position [190, 191].

## 3.4 Conclusion

In conclusion, we have investigated the pressure and distance dependence of the anisotropic etching of graphite surfaces in a H plasma. We have found that the etching characteristics can be divided into two regimes, the remote and the direct plasma regime. In the remote region of the plasma ($d' > 0$) etching only occurs at preexisting defect sites whereas for $d' < 0$ new defects are induced. Further, we have prepared SL and BL graphene flakes on $SiO_2$ and hBN substrates and exposed them to the remote H plasma. We observed isotropic etching of SL graphene on $SiO_2$, whereas on hBN it is highly anisotropic, exhibiting very regular and symmetric hexagonal etch pits. BL graphene, on the other hand, did not show a substrate dependence of the etching character and was anisotropic for both substrates.

By inducing artificial defects by lithographic means it becomes possible to pattern graphene nanostructures of various geometries with clean crystallographic edges defined by the etching in a remote H plasma. This leads to the opportunity to fabricate GNRs with well defined edges on a well suited substrate for electronic transport experiments, such as hBN. It would be interesting to study the etching process in dependence of the graphene electrochemical potential, which can be adjusted in-situ with a back gate during the etching process. Also, a remote nitrogen plasma [73] could be investigated to be potentially used in a similar way to define armchair edges via anisotropic etching of atomic nitrogen.

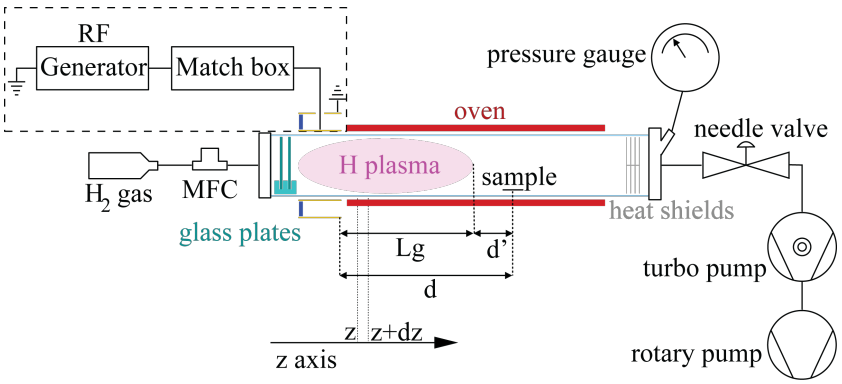


**Figure 3.5: Setup** of the plasma furnace. The quartz tube has a length of ca. 1 m and a diameter of 80 mm (drawing not to scale).

## 3.5 Materials and Methods

A pure H plasma was created in a quartz tube through a matching network by a 13.56 MHz radio frequency (RF) generator at a typical power of 30 W. See Figure 3.5 for a sketch of the setup. This RF power was capacitively coupled to the 80 mm diameter tube by an outer electrode acting as a surfatron [192]. The pressure was regulated using a needle valve for 20 SCCM H gas flow of purity 6N. The sample was placed at a distance $d$ from the end of the surfatron, was electrically floating and a three-zone furnace controlled the temperature $T$. The ion impact energy is roughly the difference between the plasma potential and the floating potential and is around $10-15$ eV with an average ion mass of 2 amu. We estimate the ion flux to be significantly lower than $10^{15}$ ions/cm$^2$s measured for a similar plasma setup but at lower pressure [189]. In order to characterize and optimize the anisotropic etching process, we studied the influence of pressure, distance, and temperature on the etching process, generally finding good repeatability. In particular, the graphene on hBN exposures have been reproduced more than ten times. Data points where a technical malfunction has occurred are not included in the evaluation.

## 3.6 Acknowledgements

We would like to thank B. Eren, R. Maurand, C. Schönenberger and R. Steiner for helpful discussions. We acknowledge support from the Swiss Nanoscience Institute (SNI), NCCR QSIT and Swiss NSF. Growth of hexagonal boron nitride crystals was supported by the Elemental Strategy Initiative conducted by the MEXT, Japan and JSPS KAKENHI Grant Numbers JP26248061, JP15K21722 and JP25106006.

## 3.7 Author Contributions

D. H., S. Z., M. R., Y. K. and T. C. prepared samples and carried out the measurements. D. H., M. R. and D. Z. wrote the manuscript with contributions from all authors. L. M. helped with the plasma setup. K. W. and T. T. provided the hexagonal Boron Nitride.

## 3.8 Supplementary Information

### 3.8.1 Direct and remote plasma region

In Figure 3.6, AFM scans acquired after exposure of natural graphite samples for 1 hour to a pure hydrogen (H) plasma at a power of 30 W depict the influence of the pressure and distance on the etching strength and type. For every pressure and distance combination a new graphite sample was fabricated as described in the main text. The matrix representation of the AFM scans of the complete set of investigated parameters remarkably demonstrates the transition from soft anisotropic etching (above or to the right of the cyan line) including only H atoms, to strong etching parameters (below or to the left of the cyan line) comprising also ions. The separation between the two regimes is based upon the size distribution of the hexagonal pits as ions are expected to induce defects acting as new etch sites throughout the whole exposure time. Lowering the pressure as well as decreasing the distance has the effect to increase the number of holes as well as the size distribution and depth of the etch pits, demonstrating an

increase of the reactive particle density. On some of the AFM images, unintentional growth or deposition of some additional nanostructures such as worms or particles is seen, e.g. $d = 42\,\mathrm{cm}$ and $p = 1.4\,\mathrm{mbar}$ or $p = 0.7\,\mathrm{mbar}$.

For all AFM scans shown in Figure 3.6, the number of holes and their respective diameters are evaluated and plotted in histograms shown in Figure 3.7, describing a comparable picture as the AFM topography scans. Again, not only the amount of holes but also the width of the diameter distribution shows a strong dependence on pressure and distance. As for the AFM scans, the remote (upper right) and the direct (lower left) plasma region can be distinguished using the widths of the distributions in the histograms. In the lower right panels we estimated the number of holes for each diameter to $> 12$ and the width of the diameter distribution to be at least 600 nm, since an exact investigation of the hole number and diameter was not feasible (see Figure 3.6).

The number of hexagons etched into the graphite surface as well as the width of the hole diameter distribution reflect the number of ions inducing defects on the graphitic surface, assuming a low intrinsic defect density on the surface of the graphite samples.

### 3.8.2 Exponential decay of reactive particles

The number of holes (purple) and the width of the diameter distribution (orange) is shown in Figure 3.8 against the distance between the plasma edge and the sample, $\mathrm{d}' = d - L_g$. For $\mathrm{d}' < 0$ the sample is directly exposed to the glowing plasma, hence experiencing the impact of ions perforating the graphite surface with uncountable, several layers deep holes. For $\mathrm{d}' > 0$ on the other hand, the hole number and the width of the hole distribution both appear to roughly decay exponentially with larger sample-plasma distance, with an 1/e decay length of $\sim 5\,\mathrm{cm}$ extracted from a fit to an exponential (dashed lines).

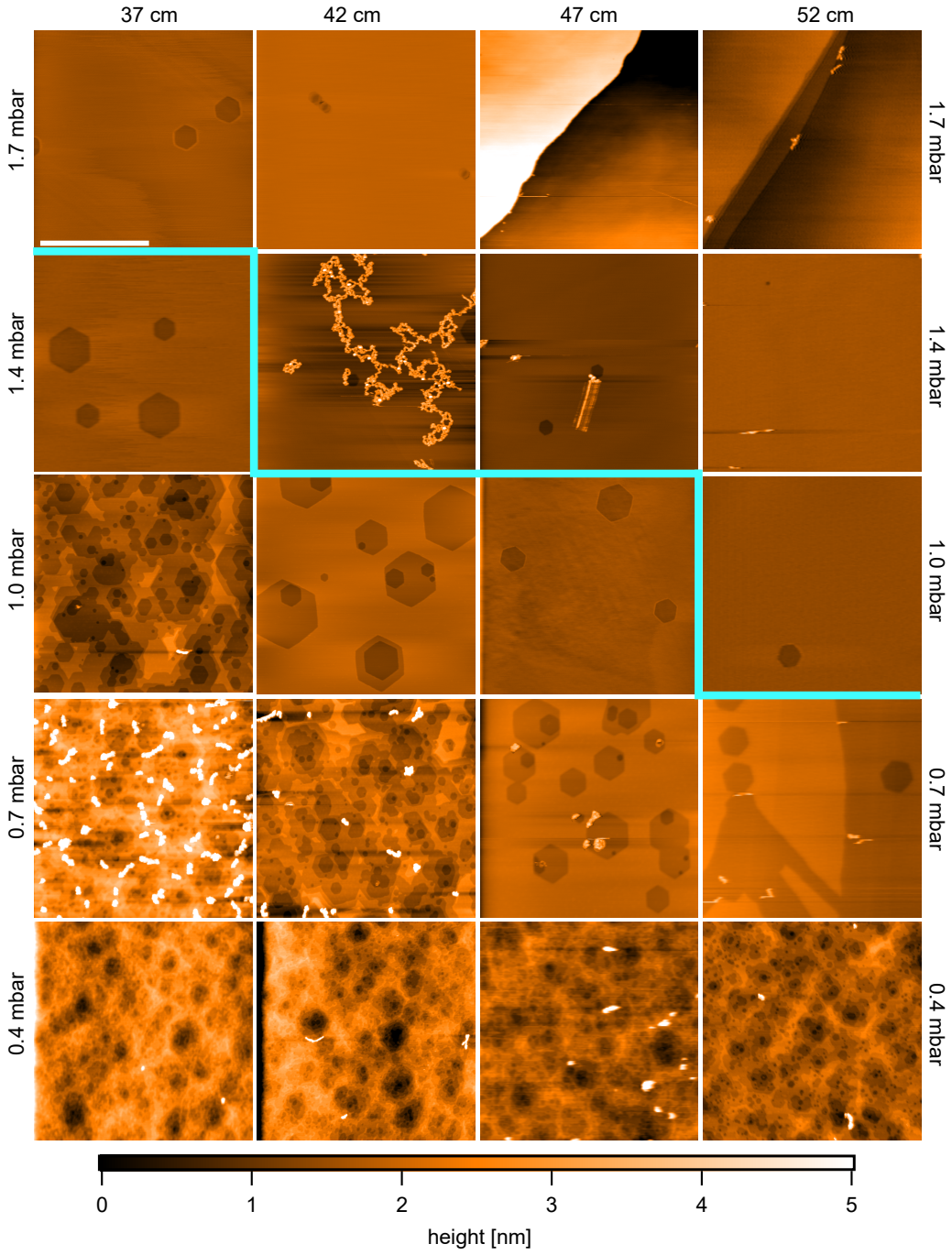


**Figure 3.6: Distance and pressure dependence of graphite plasma exposure.** AFM topography scans at all parameters investigated in Figure 1E in the main paper. All AFM images are $2 \times 2\,\mu\text{m}^2$ in size. The cyan curve marks the transition from the remote (upper right) to the direct (lower left) plasma region. On some surfaces, particles are visible which probably are amorphous carbon residues, either grown or deposited during the etching process (see AFM scans for $p = 0.7\,\text{mbar}$ and $d = 37\,\text{cm}$ or $p = 1.4\,\text{mbar}$ and $d = 42\,\text{cm}$).

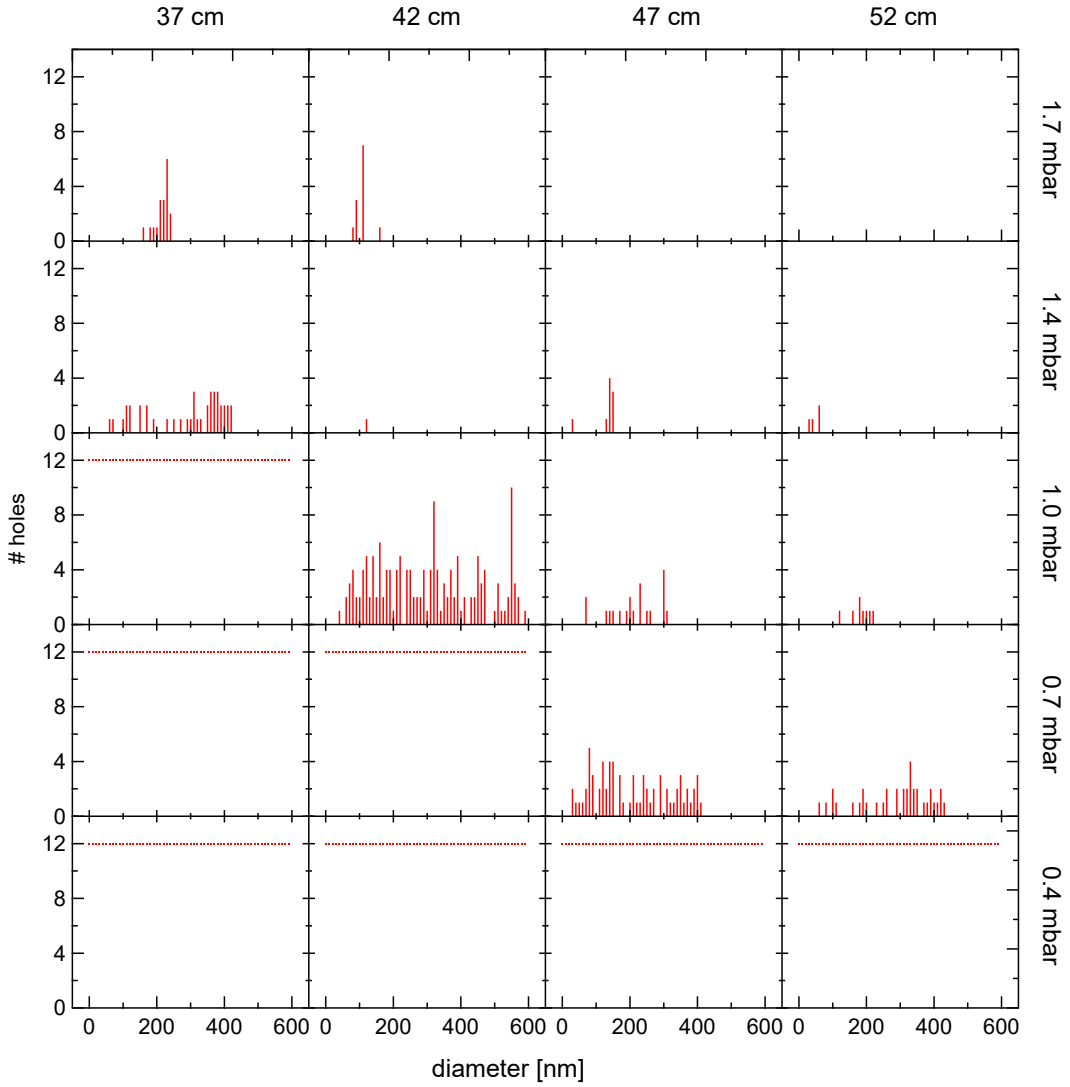


**Figure 3.7: Distance and pressure dependence of graphite plasma exposure.** Histograms (10 nm bin size) showing the number of holes for all pressure and distance parameters corresponding to Figure 3.6, obtained from $10 \times 10\,\mu\text{m}^2$ AFM scans. For AFM scans of strongly etched surfaces, we plot 12 holes for every hole diameter.

The radical concentration is decaying exponentially when moving down the axis of the tube, and is given by [76, 184]

$$[H] = [H]_0 \cdot \exp\left(-a\sqrt{p}d'\right) \tag{3.1}$$

with sample-plasma edge distance $d'$, concentration $[H]_0$ at $d' = 0$, pressure $p$, and the geometrical factor $a$:

$$a = \sqrt{\frac{v_{therm}\gamma}{R \cdot D'}}. \tag{3.2}$$

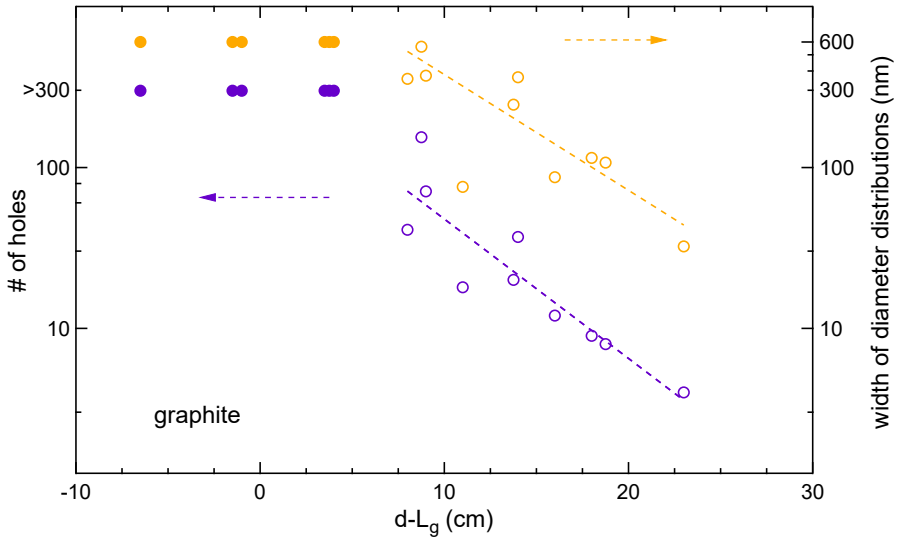


**Figure 3.8:** Number of holes (purple, left axis) and width of diameter distribution (orange, right axis) as a function of effective distance $d' = d - L_g$.

Here, $v_{therm} = \sqrt{8k_BT/(\pi m)} \approx 2'750\,\mathrm{m/s}$ is the molecular $H_2$ thermal velocity, with Boltzmann constant $k_B$, hydrogen mass $m$ and temperature $T$. The material dependent recombination coefficient [76, 184] of the radicals is $\gamma \approx 7.5{\cdot}10^{-4}$, $R = 4\,\mathrm{cm}$ is the radius of the quartz tube and $D' = 7.39\,\mathrm{atm\ cm^2/s}$ is the temperature dependent diffusion coefficient [193, 194] taken here at $\sim 700\,\mathrm{K}$ from Ref. [193]. Note the explicit pressure dependence of the decay length. Here, this results in a decay length of $\approx 12\,\mathrm{cm}$ at $p = 1\,\mathrm{mbar}$, which is consistent with our data. As mentioned in the main manuscript, the recombination of the radicals in the gas phase is expected to be irrelevant and the radicals only recombine at the surface of the quartz tube for the pressure range $p \sim 1\,\mathrm{mbar}$ used here.

### 3.8.3 Raman measurements before and after plasma exposure

The influence of the H atoms on the graphene quality was further investigated by performing Raman measurements before, after 3 h and after 5 h of plasma exposure, as shown in Figure 3.10. To compare the Raman traces, we subtracted the background before normalizing the traces with the graphene G peak height at $\approx 1582cm^{-1}$. The Raman scans taken on the bare hBN substrate in panel D are normalized to the $SiO_2$

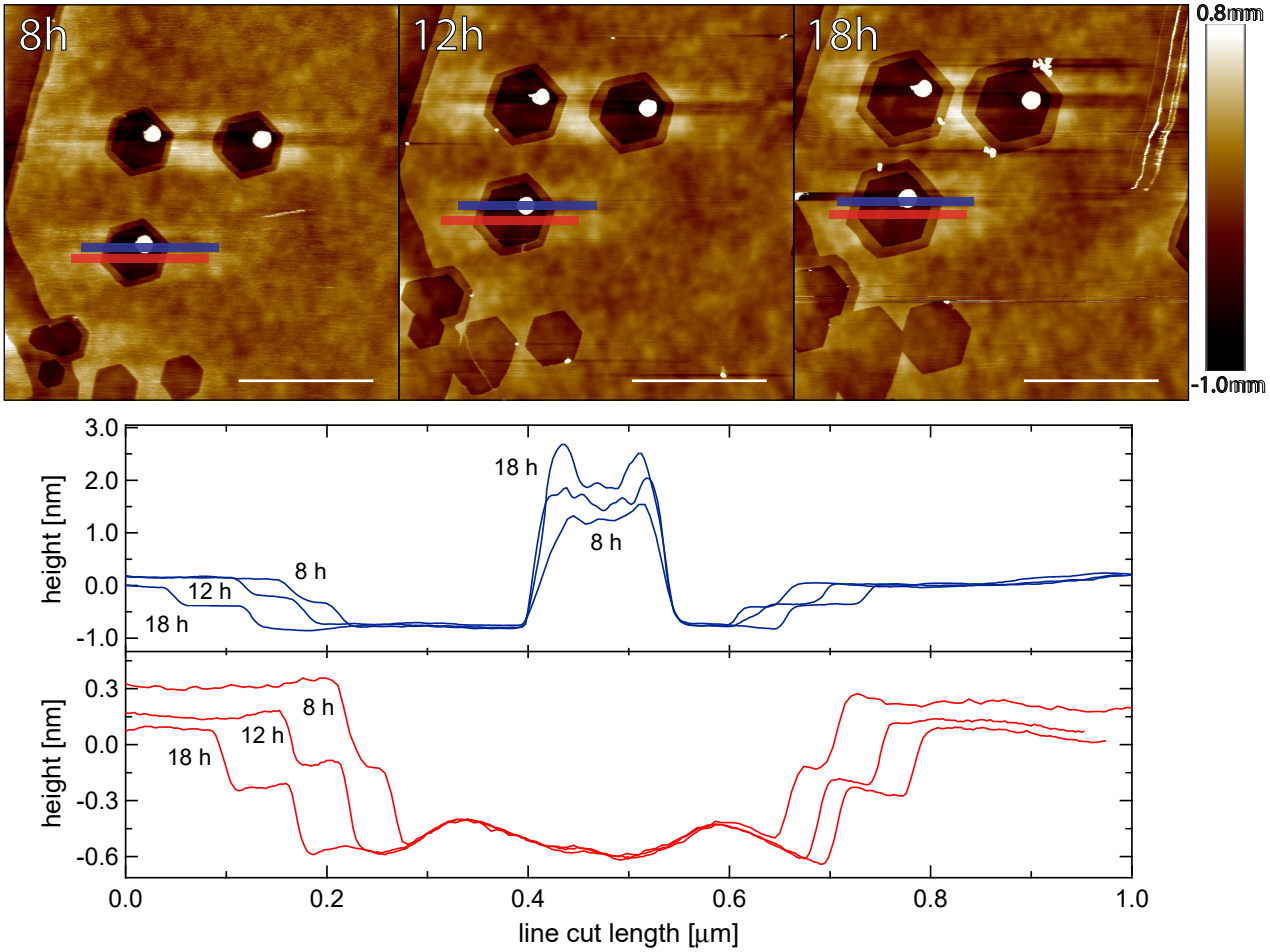


**Figure 3.9: AFM images of BL graphene on an hBN substrate** time series after 8 h, 12 h and 18 h of remote H-plasma exposure (upper panel). AFM profiles (lower panel) taken along paths indicated in upper panel (color coded). Averaging over the vertical range as indicated by the finite vertical width bars in the upper panel is performed to obtain an improved signal. These cuts demonstrate that the hBN substrate is not etched by the H-plasma, since the graphene step height is independent of exposure time. The center pillar appears to be growing with exposure time.

peak (not visible) to allow comparison. All Raman measurements presented in this work were acquired with a green laser with a wavelength of $\lambda = 533\,\mathrm{nm}$, where the bulk hBN $E_{2g}$ peak at $1366\,\mathrm{cm}^{-1}$ and the graphene D-peak at $1350\,\mathrm{cm}^{-1}$) are close to each other. Nevertheless, in many cases a weak D-peak can still be reliably extracted.

Panel D shows Raman spectra of the hBN flake before (yellow), after 3 h (blue) and after 5 h (red) of remote H plasma etching. The hBN $E_{2g}$ peak [195] shape, height and position does not significantly change, indicating no or only insignificant interaction of the hBN with the H plasma. Panel E shows Raman spectra acquired on bulk graphene,

again before (yellow), after 3 h (blue) and after 5 h (red) of H plasma etching. We did not observe a D-peak in the bulk of the graphene flakes even after 15 h of plasma etching (not shown), indicating no induction of defects or hydrogenation of our samples [186, 187]. Note that after the end of the plasma exposure, the samples are annealed in vacuum while the oven is cooling down from process temperature to room temperature.

Significant information about the type and quality of edge can in principle be obtained from Raman spectra of the graphene edge [169]. However, care needs to be taken to not overheat and possibly reconstruct or otherwise change the edge with the laser [196] when illuminating the graphene edge on $SiO_2$ at a laser power of 1.5 mW or more. Our spectra do not meet these low power requirements. The damage threshold for graphene on hBN is not known, and study of these effects goes beyond the scope of this work.

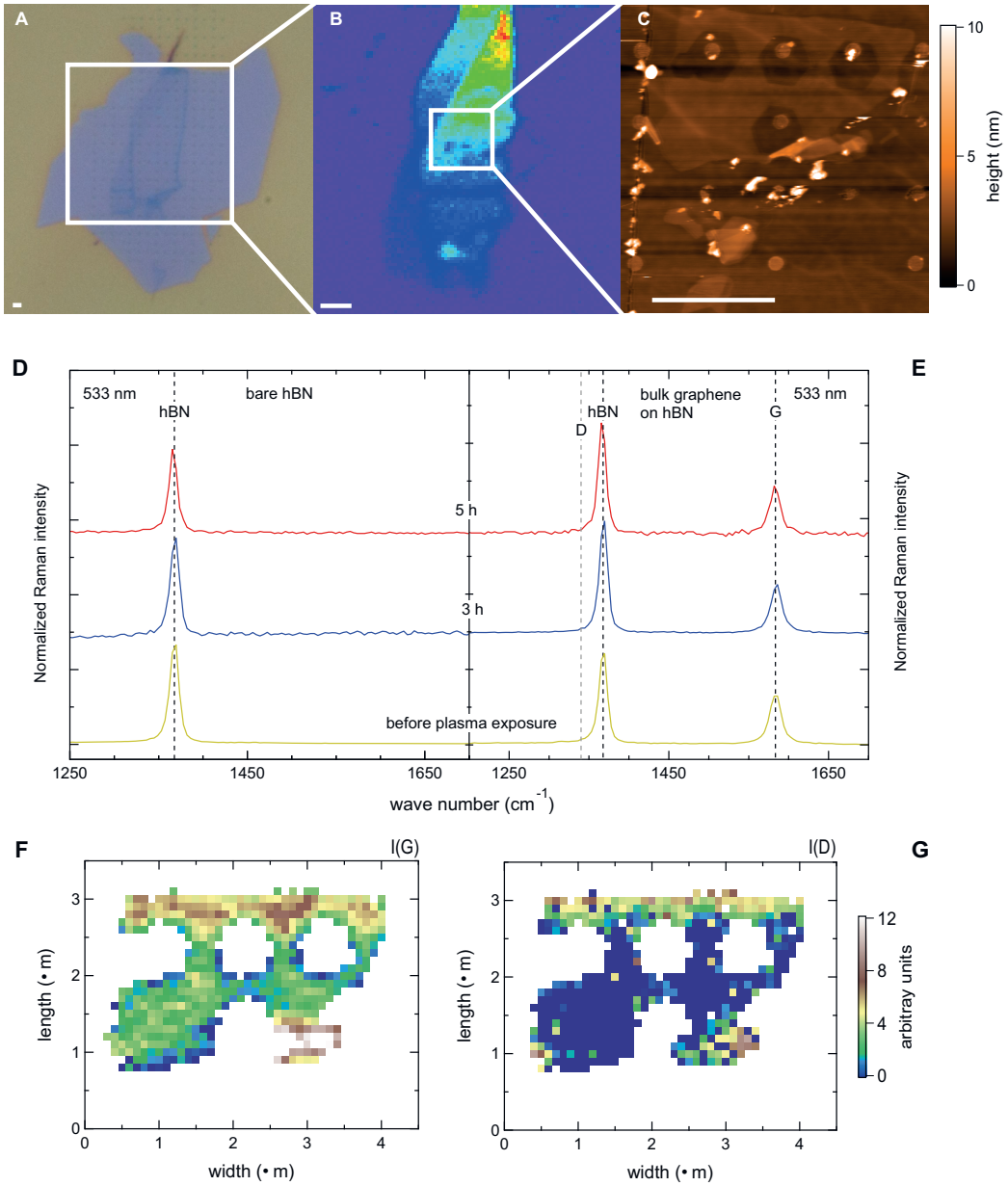


**Figure 3.10: Raman spectra and spatially resolved Raman scans of the hBN sample in the main paper.** Panel A: optical image of a graphene on hBN sample. Panel B: Raman map of the 2D peak of the same graphene flake before H plasma exposure. Panel C: AFM topography scan showing the region where the Raman single spectra were taken. The scale bars in Panel A to C are 2 $\mu$m. Panel D and E: Raman spectra of the bare hBN flake (panel D) and bulk graphene on hBN (panel E) before (yellow), after 3 h (blue) and after 5 h (red) of remote plasma exposure. The Raman spectra are vertically shifted for clarity. Panel F and G: 2D maps of the G peak (panel F) and D peak (panel G) of the flake region shown in panel C.

# 4 Anisotropic Etching of Graphite and Graphene in a Remote Nitrogen Plasma

T. N. Camenzind, M. K. Rehmann, Y. B. Kalyoncu and D. M. Zumbühl

*Department of Physics, University of Basel, CH-4056 Basel, Switzerland*

## 4.1 Introduction

In the previous part of this work, the focus of discussion has been lying on anisotropic etching with a remote hydrogen plasma. The process creates hexagonal-shaped etch pits with zigzag (ZZ) edge termination which can be used to fabricate nanoribbon samples for electron transport studies. The main focus lies on the magnetic ordering at the edges which results in spin-selective transport. Changing the gas used to create the plasma from hydrogen to nitrogen changes the edge termination of the hexagonal-shaped etch pits. Instead of ZZ terminated edges, the process results in armchair (AC) edge termination [73]. This changes the electronic band structure as well as the transport properties fundamentally (see section 2.1.2 for more details). In theory, shifting the band structure in $k$-space and opening a gap at $k = 0$ will allow the graphene nanoribbon to host Majorana fermions [23]. Experimentally, this can be achieved by using a rotating magnetic field induced by nanomagnets and by proximity induced superconductivity.

The first step in creating a sample for hosting Majorana fermions is the fabrication of an AC-terminated nanoribbon. In order to accomplish that, we investigated the etching induced by a remote nitrogen plasma. The investigated parameters were the distance $d$ from the plasma to the sample, the pressure $p$ inside the reaction chamber and the power $P$ used to generate the plasma. The plasma itself was created using a MKS Instruments 1kW remote process applicator driven by a solid state microwave generator with an automatic impedance matching box in between. This setup allows for a highly tunable nitrogen plasma containing the glowing region within the applicator and, in theory, only $N$ radicals are found outside of the applicator. In contrast to the RF driven surfatron used in the previous work with a remote hydrogen plasma, the generation of nitrogen radicals demands more energy because of the triple bond of $N_2$ molecules. This could partially explain why no sign of anisotropic etching has been seen in a previous study where the nitrogen plasma has been generated with an RF source and only 30 W of power [197].

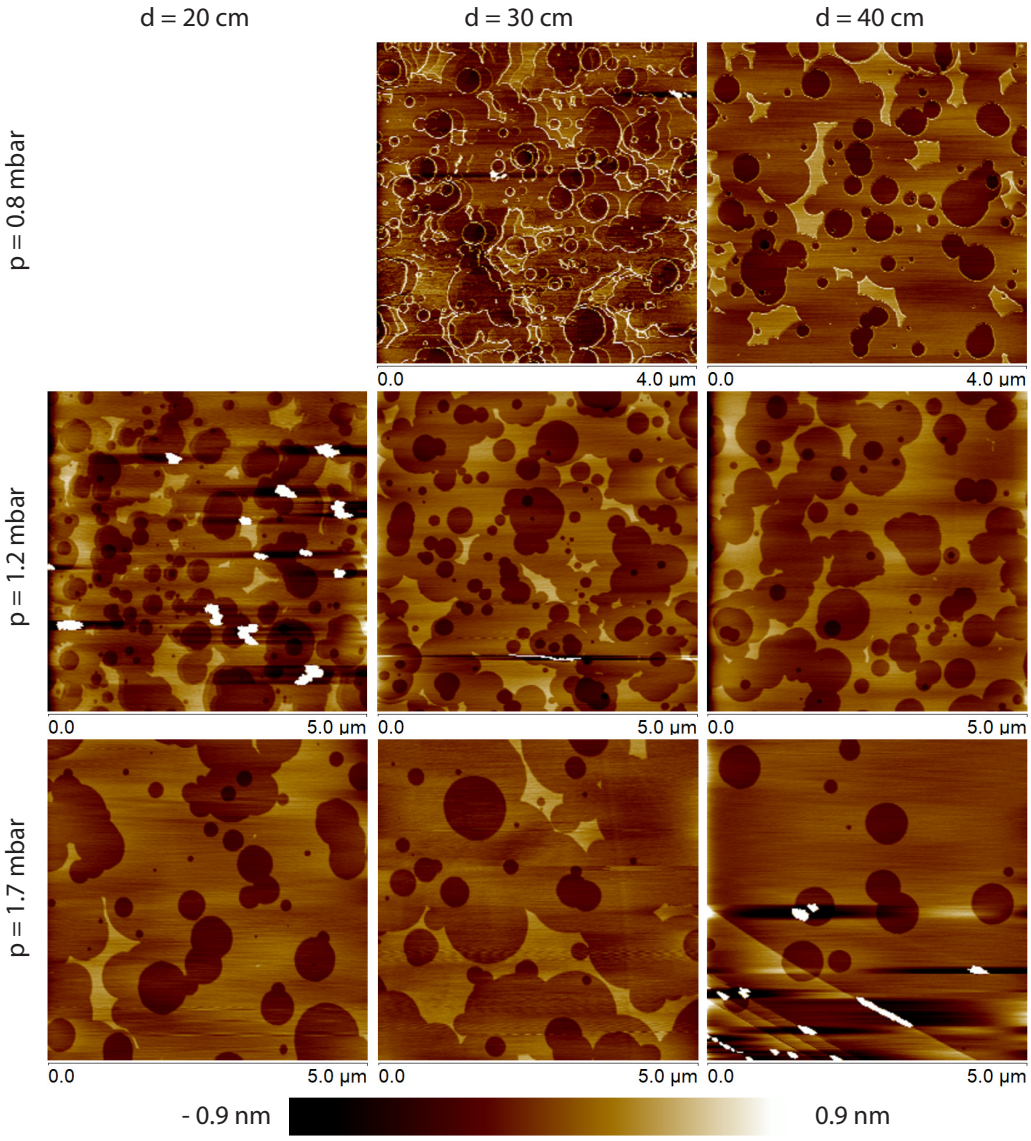


**Figure 4.1: Distance and pressure dependence of etch pits in graphite due to nitrogen plasma exposure.** There are two clear trends visible. Both the size and amount of etch pits are reduced by either increasing the pressure or the distance to the glowing region of the plasma. This is in agreement with the recombination rate of active nitrogen species (ions), where the rate decreases for larger distances and higher pressure. No hexagonal etch pits are visible because the anisotropic etching region (remote plasma) has not been reached under all investigated conditions.

## 4.2 Distance, Pressure and Power Dependence

In figure 4.1, we show the pressure and temperature dependence of the nitrogen plasma induced etching at 800 °C. Overall, there are two clear trends visible. First, increasing the pressure inside the reaction chamber reduces both the amount of etch pits and the number of etched layers of graphite. Additionally, the more the pressure is increased, the more the size of these etch pits is reduced. The same trend can be seen when increasing the distance between the glowing region of the plasma and the sample itself. Both phenomena can be explained by a reduced amount of active species, namely nitrogen radicals and ions, due to the recombination at the reaction chamber walls. At the same gas flow of nitrogen into the plasma zone, higher pressure results in more collisions between two active species and subsequently into recombination to nitrogen molecules which do not etch graphite. This is also true for the distance dependence, as larger distances amount to more possible collisions. For single-layer etching, only the regime at the largest investigated distance and pressure seems viable. However, anisotropic etching has not even been seen in this remote regime where it should be possible according to Zhang *et al.* [73].

We propose possible explanations for this non-existence of anisotropic etching in our setup. Because nitrogen ions tend to etch isotropically and we only see round etch pits, we believe that we are not yet in the purely remote regime needed for anisotropic etching. To reach this regime, we would need to increase the distance to the glowing part of the nitrogen plasma further by extending the reaction chamber. This has not been done due to the non-availability of appropriately long suprasil tubes at the time. Another reason why the anisotropic region has not been reached in our setup could be the amount of gas or the speed of the gas flow passing over the samples. In contrast to the previous work with a remote hydrogen plasma, no quartz diffuser plate has been placed between the inlet of gas and the creation region of the plasma in our experiments. This could lead to an increased speed of the gas through the reaction chamber, therefore reducing the amount of possible collisions for ions to combine an

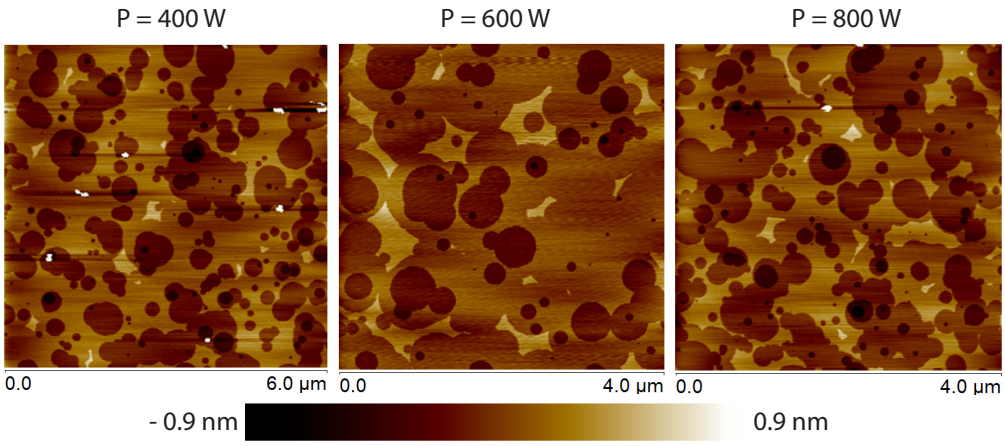


**Figure 4.2: Power dependence of etch pits in graphite due to nitrogen plasma exposure.** The applied power to the applicator seems to have no influence on the amount and size of the etch pits in this regime. This can be either explained that all nitrogen bonds have already been broken at the lowest applied power or that not enough power has been applied to the system. Pressure applied in this series was 1.2 mbar at a distance of 50 cm.

so to inert nitrogen molecules. However, a control experiment with a remote hydrogen plasma with the GHz source showed hexagonal-shaped etch pits of the same quality and quantity as when the RF surfatron source is applied.

Another possible explanation for the isotropic etching could be the applied power to create the plasma. We performed experiments ranging from 200 to 800 W of microwave power but did not see any significant change in the shape of the etch pits (see figure 4.2). One note here is that the power injected by the solid state generator does not necessarily add up to the same amount of power coupled into the plasma, as the matching box inherently reduces the forwarded power due to its design. However, we deem this negligible since the power loss is usually around 10% and thus not contributing significantly to changing the etching from isotropic to anisotropic.

Finally, there is a small metallic portion of the applicator where it connects to the suprasil tube. From previous studies it is known that ions and especially radicals tend to recombine at walls due to catalytic effects. This is especially true for metallic surfaces as the binding energy is significantly larger than for other surfaces such as quartz or suprasil. We therefore introduced a small quartz tube to shield the gas flow

from the metallic walls but it did not change the results in a meaningful way. The etch pits stayed round and no anisotropic etching has been observed in any experiment conducted in our laboratory.

## 4.3 Conclusion

In summary, we tried to exploit the anisotropic etching that a remote nitrogen plasma is supposed to induce according to Zhang *et al.* [73]. During our testing, all experimentally possible parameters such as distance to the plasma, pressure inside the reaction chamber and applied power were varied over a large range. However, we were not able to reach the anisotropic etching regime in our laboratory. We believe this to be linked to our specific setup, where we were not able to reach the remote plasma regime where only nitrogen radicals are present. This could be achieved by using a longer tube or larger pressure, as both increase the recombination of nitrogen ions. As an outlook, if the remote regime is reached, where only anisotropic etching happens, experiments will shift to graphene samples because the parameters for anisotropic etching could change when changing the substrate [198]. Further investigations into the edges using Raman spectroscopy are then needed for the determination of the nanoribbon edge quality and possible use for hosting Majorana fermions [23].

# 5 High mobility SiMOSFETs fabricated in a full 300 mm CMOS process

T. N. Camenzind and D. M. Zumbühl

*Department of Physics, University of Basel, CH-4056 Basel, Switzerland*

A. Elsayed, F. A. Mohiyaddin, R. Li, S. Kubicek, J Jussot, B. Govoreanu and I. Radu

*IMEC, Kapeldreef 75, B-3001 Leuven, Belgium*

This chapter was published on *arXiv:2106.05254*

## 5.1 Abstract

The quality of the semiconductor-barrier interface plays a pivotal role in the demonstration of high quality reproducible quantum dots for quantum information processing. In this work, we have measured SiMOSFET Hall bars on undoped Si substrates in order to investigate the quality of the devices fabricated in a full CMOS process. We report a record mobility of $17.5 \times 10^3\,\mathrm{cm}^2/\mathrm{Vs}$ with a sub-10 nm oxide thickness indicating a high quality interface, suitable for future qubit applications. We also study the influence of gate materials on the mobilities and discuss the underlying mechanisms, giving insight into further material optimization for large scale quantum processors.

## 5.2 Introduction

The spin of an electron in Silicon has been considered as one of the most promising candidates for large-scale quantum computers, due to its long coherence time, compactness, potential to operate at relatively high temperatures, and compatibility with CMOS technology for upscaling [10, 199, 200]. High fidelity single and two qubit operations have been demonstrated in academic lab-based devices [108, 201]. The scale up process to multi-qubit arrays will however entail high quality qubits in large numbers, necessitating a transition to industrial fabrication techniques [202].

While spin qubit-devices can be fabricated using semiconductor manufacturing techniques, a detailed and careful analysis on the impact of different fabrication process steps on the performance of spin qubits is crucial. Hallbar mobility is a widely used metric to characterize the MOS interface quality, which can provide valuable feedback to fabrication process optimization. In this work, we perform transport measurements on SiMOSFETs and investigate the quantum Hall effect. The gate stack for SiMOSFET is the same as that for qubit integration [203]. We extract key characteristics of the MOS gate stack such as critical density and mobility as well as transport and quantum lifetimes. Comparing the obtained results to a transport model, we identify

and quantify the leading scattering terms. Additionally, we explore possible mobility limiting factors when changing the top gate material from PolySi to titanium nitride (TiN).

The devices measured in this work are undoped inversion gated Hall bars fabricated in a state-of-the art 300 mm fab line [203]. The starting substrate consists of a (100) silicon wafer with a background doping $<5 \times 10^{15}\,\mathrm{cm}^{-3}$. The Hall bar top gates are defined by electron beam lithography and subsequent dry etching process, and the fanout metal pins are defined by deep UV lithography. After depositing the gate material, the whole wafer is covered with a passivation layer. In order to measure the electronic properties of the investigated samples, a positive voltage has been applied to the top gate to form a 2-dimensional electron gas (2DEG) at the interface of Si and $SiO_2$. Throughout this work, we perform four-wire electronic transport measurements using standard lock-in techniques. Both the longitudinal and transverse Hall voltages were measured simultaneously with differential voltage amplifiers. Additionally, the current through the sample was measured using an IV transimpeadance amplifier. The measurements were carried out in a dilution refrigerator with a base temperature of 20 mK with a 9 T magnet. Higher temperatures were achieved by heating the mixing chamber, resulting in electron temperatures between 100 mK and 4.2 K.

## 5.3 Density and Mobility Study

Fig.5.1 shows the density and mobility study performed on a sample with a PolySi top gate at three different temperatures. First, the density of charge carriers in the 2DEG was extracted from the transverse Hall effect in the linear regime far from quantum oscillations, particularly at the lowest temperature with magnetic field between $\pm 1$ T. The density of charge carriers in the 2DEG has an overall linear dependence on the applied top gate voltage $V_G$ as expected from a plate-capacitor model. Assuming the relative dielectric constant $\epsilon_r(SiO_2) = 3.9$, we extract the thickness of the oxide and obtain a value of $8.1 \pm 0.1$ nm. This in good agreement with the oxide thickness of

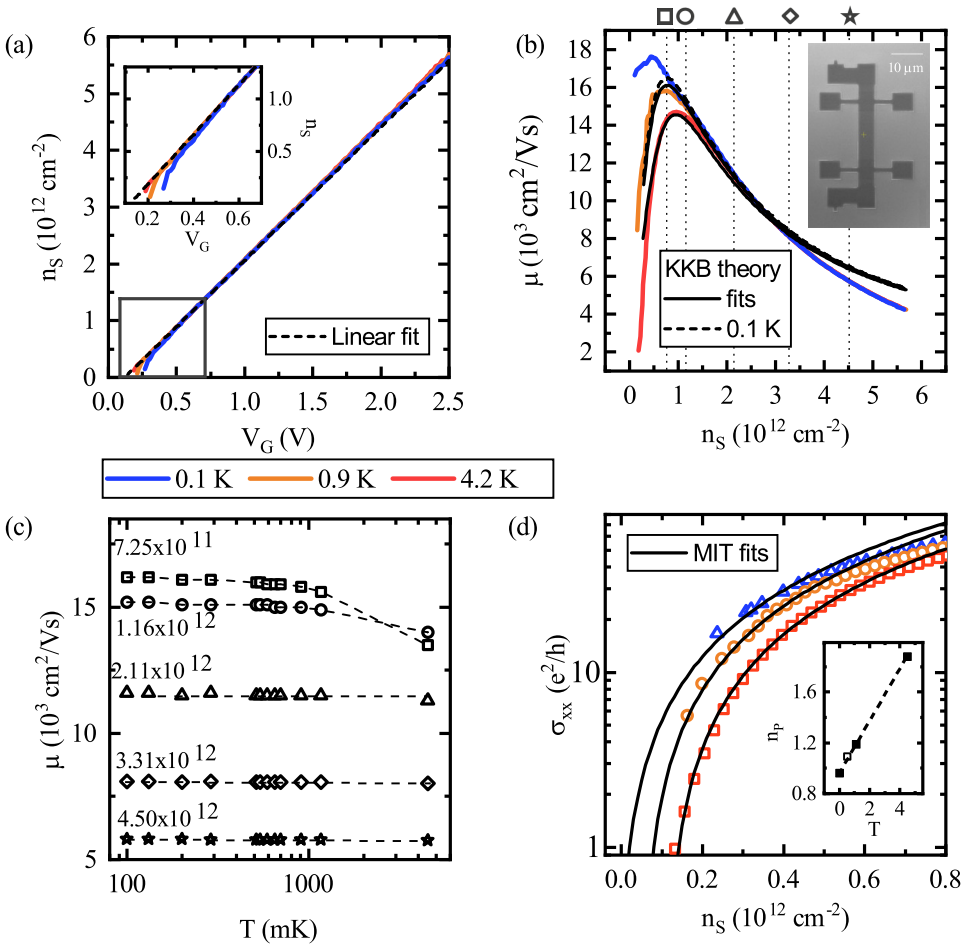


**Figure 5.1: Density and Mobility study** (a) Linear relationship between 2DEG sheet density $n_S$ and the top gate voltage $V_G$. Below a top gate voltage of $\approx 0.4\,\mathrm{V}$ the extracted density deviates from the expected linear behaviour as shown in the inset. (b) Channel mobility $\mu$ measured as a function of $n_S$ and corresponding fit to a mobility model (black) which includes scattering from charge impurities and surface roughness. The inset shows a SEM image of a similar device as the one used during the experiments with the same dimensions. (c) Channel mobility $\mu$ trends with respect to temperature at various sheet densities. The symbols coincide with the ones used in panel b. The dashed lines are linear fits to the extracted mobilities and appear curved due to the logarithmic scale. (d) Longitudinal conductivity $\sigma_{xx}$ in the low density range and fit to a percolation theory (black). A linear trend with respect to temperature for $n_p$ is observed in the inset.

8 nm defined during the fabrication process. As one can see in the inset of Fig.5.1a, the extracted density deviates from a linear regime at very low $V_G$ near the threshold voltage, particularly at the lowest temperature. A temperature dependent dielectric constant would result in a temperature dependent slope of the $n_S$ regardless of the $V_G$ [204], which is not observed in this study. Partial localization of charge carriers in the disorder potential at low sheet density, on the other hand, could explain this [205]. Here, the disorder potential is mainly due to bulk charge scattering and scattering from oxide charges. At these rather low densities close to the 2D Metal to Insulator Transition (MIT), partial localization would effectively reduce the sheet density of mobile carriers below a simple capacitor model, as observed, and thus slightly enhance the mobility, which is inversely proportional to the density.

The extracted densities, in combination with the sheet conductance from the longitudinal voltage measurements, allow for the calculation of the mobility $\mu$ at various temperatures. The resulting curves are shown in Fig.5.1b. We measured a maximum mobility of $17.5 \times 10^3\,\mathrm{cm}^2/\mathrm{Vs}$, among the highest mobility reported for SiMOSFET devices with sub 10 nm oxide thickness [27–29]. We fit the mobility curve with the Kruithof-Klapwijk-Bakker (KKB) model (Ref. [137]) which includes remote impurity scattering and surface roughness terms [137, 149]. Solving the model self-consistently for three separate temperatures (0.5, 0.9 and 4.2 K) yields the charged impurity center density $N_C = 1.53 \pm 0.03 \times 10^{10}\,\mathrm{cm}^{-2}$, the rms height of the amplitude of the interface roughness $\Delta = 5.9 \pm 0.51$ Å and the correlation length $L = 1.8 \pm 0.35$ nm. These numbers indicate a smooth and clean interface which is critical for future qubit implementations.

As shown in Fig.5.1b, there is a slight deviation of the maximum mobility from the theory curve at 0.9 K, and the theoretical curve does not agree with the reported data for 0.1 K in the low density regime. This could be explained by the assumption of a linear relationship between mobility and temperature in the KKB theory. According to our fitting, this assumption seems to be only valid above 1 K and can become a

more complex function of temperature below 1 K if the low density regime becomes non-linear. This is due to the fact that the slightly reduced density (compared to the capacitor model) results in a slightly higher mobility, explaining the deviation of our data from the theory. Furthermore, for sheet densities $n_S$ close to the depletion charge density $n_{dep}$, the calculation of the finite extent of the wave function in the KKB theory can become unreliable because of the assumed approximations. The theoretically predicted curve can be recovered by using a linearly extrapolated density during the calculation of the mobility. Further details are discussed in section 5.10.1.

Another key parameter is the percolation density, which indicates the minimum density required to form a conducting channel. Generally, the percolation density describes the disorder in the channel at low densities, where quantum devices typically operate. In Fig.5.1d, we employed a MIT model in order to fit the density-dependent conductivity $\sigma_{xx} \sim (n-n_p)^p$ [128], where $n_p$ and $p$ are the percolation density and universal exponent, respectively. However, this model is only valid in the low density regime and deviates above $n = 8 \times 10^{11}\,\mathrm{cm}^{-2}$. We fixed the exponent $p = 1.31$, as expected in a two-dimensional system, and allowed $n_p$ to vary [128]. Our fits yield $n_p = 1.86 \times 10^{11}\,\mathrm{cm}^{-2}$ at $T = 4.2\,\mathrm{K}$. As seen in the inset of 5.1d the extracted $n_p$ decreases with decreasing temperature, which is in agreement with previous studies [128], and is below $1 \times 10^{11}\,\mathrm{cm}^{-2}$ at the lowest temperature. Such a low percolation density is among the lowest reported for similar devices[28, 206]. The small percolation density and high peak mobility indicate low interface disorder of the MOS gate stack, which is crucial for large scale quantum dot arrays.

Additionally, we investigate the temperature dependence of mobility at various top gate voltages. For sheet densities less than $2 \times 10^{12}\,\mathrm{cm}^{-2}$ the mobility is a function of temperature, with a linear dependence for temperatures above 1 K (see Fig.5.1c). The temperature dependence of the mobility is only visible for low electron densities because mobilities at higher densities are limited by surface roughness, which is not temperature dependent. Additionally, the peak mobility shifts to higher densities at

higher temperatures due to the activation of background charges limiting the mobility at high temperatures.

## 5.4 Transport Study

In order to extract more information about the transport properties and the dominating scattering mechanism, we investigated the transverse resistance $R_{xy}$ and longitudinal resistivity $\rho_{xx}$ in the quantum Hall regime. The magnetic field $B$ was swept up to 8.5 T at a fixed sheet density of $7.1 \times 10^{11}\,\mathrm{cm}^{-2}$ near the peak mobility. As shown in Fig.5.2a, we observe Shubnikov-De Haas (SdH) oscillations starting at 0.8 T and begin to resolve spin splitting at 3.2 T. The $\rho_{xx}$ shows well developed zeros for magnetic fields larger than 3.8 T. In combination with the single frequency of the SdH oscillations extracted below 2.5 T and the absence of beatings strongly indicate single subband occupancy. We further observe a four-fold degeneracy in the filling factor which changes to a two-fold degeneracy as we increased the magnetic field (Fig.5.2b). The remaining two-fold degeneracy is due to the two lowest lying valleys which are split off from the remaining four valleys due to the z-confinement in Silicon (100) [207]. A linear fit of the filling factor (Fig.5.2b) with respect to inverse magnetic field yields a sheet density $7.1 \times 10^{11}\,\mathrm{cm}^{-2}$ in agreement with the extracted Hall density, further confirming clean single subband transport in the investigated samples.

Upon further investigations into the SdH oscillation amplitudes below 2.5 T, we were able to extract an effective mass $m^* = 0.21 \pm 0.02 \cdot m_0$ from the temperature dependent data, which corresponds to the transverse mass expected for Silicon samples with similar background doping [100]. Further details are discussed in section 5.10.2. From fitting the SdH envelope as a function of temperature and density, we can extract the quantum lifetime $\tau_q$. By combining $\tau_q$, which includes all possible scattering events, and the transport lifetime $\tau_t = e * \mu/m^*$, which includes only the large angle scattering, we extract the so-called Dingle ratio $\tau_t/\tau_q$. The Dingle ratio thus characterizes the dominant scattering mechanism ranging from a ratio of 1 for predominant large

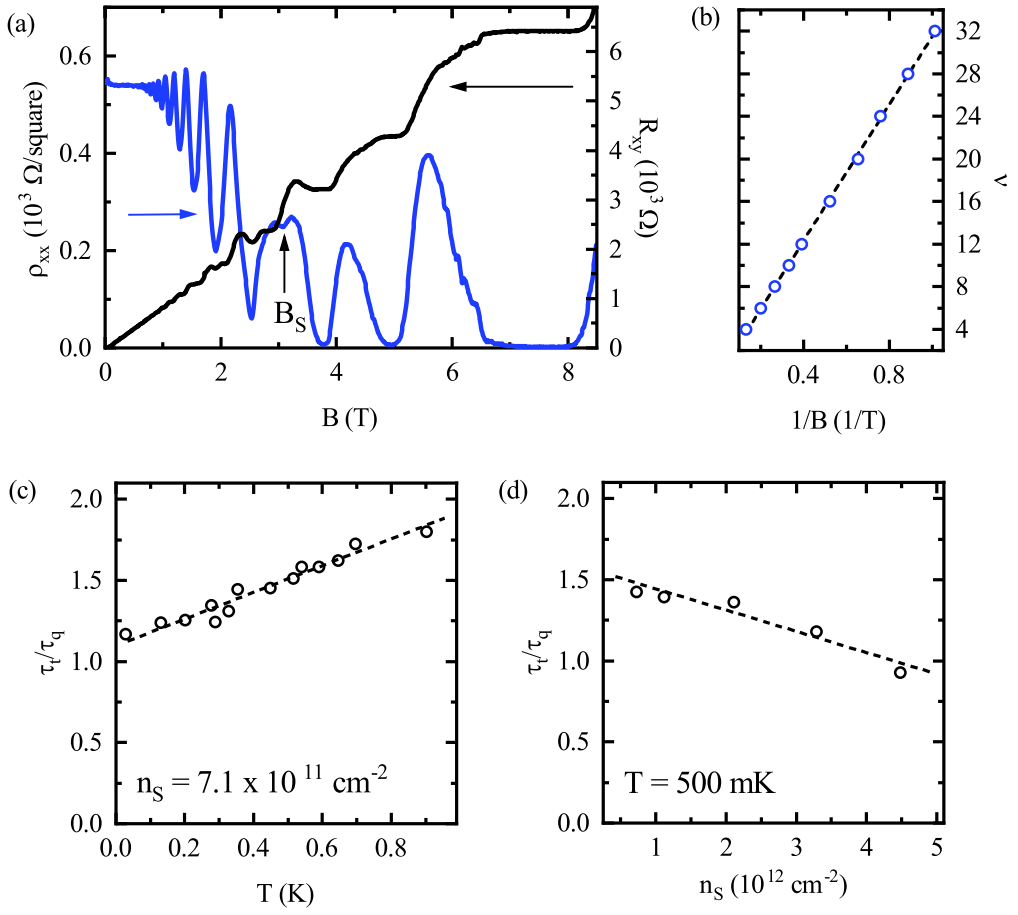


**Figure 5.2: Extended Hall studies with transport properties** (a) Longitudinal resistivity $\rho_{xx}$ (blue) and transverse resistance $R_{xy}$ (black) at $n_S = 7.1 \times 10^{11}\,\mathrm{cm}^{-2}$ as a function of magnetic field $B$. The arrow indicates the magnetic field spin is resolved. (b) Linear relationship between filling factor $\nu$ (blue scatter) and inverse magnetic field. The solid line is a fit from which the sheet density is calculated. (c) and (d) Extracted dingle ratio $\tau_t/\tau_q$ as a function of temperature $T$ and sheet density $n_S$, respectively. The dingle ratio is slightly temperature and density dependent and is $\approx 1$, which indicates that large angle scattering is most dominant scattering mechanism in this sample.

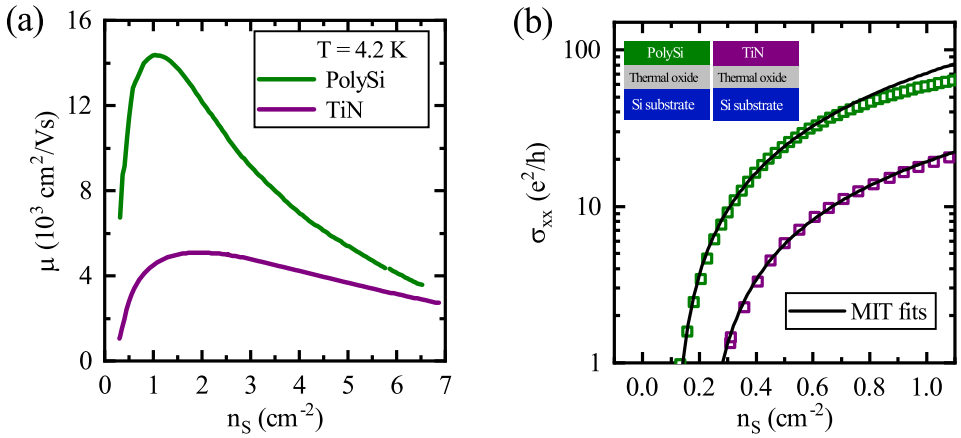


**Figure 5.3: Gate material study** (a) The channel mobility $\mu$ with respect to sheet density $n_S$ for PolySi (green) and TiN (violet), both at 4.2 K. The mobility shows a decrease by a factor of three when changing the top gate material from PolySi to TiN. (b) Longitudinal conductivity $\sigma_{xx}$ with respect to sheet density. The fits to percolation theory (black) show a significant difference between the PolySi and TiN percolation densities.

angle scattering to values >> 1 for dominant small angle scattering. Fig.5.2c shows an increase of the Dingle ratio from $\approx 1$ to $\approx 2$ with increasing temperature, indicating a shift in the type of scattering dominating at different temperature ranges. We can see an inverted trend for the Dingle ratio with respect to density. For a fixed temperature of 0.5 K, we observe a decrease from a ratio of $\approx 1.5$ to $\approx 1$ by increasing the density, again showing a slight shift towards large angle scattering. This is true for all measured temperatures and densities. In all, the observed Dingle ratio around 1 to 2 shows that short range / large angle scattering is the dominant scattering mechanism in this system, where the scattering centers are near or in the channel itself [100].

## 5.5 Influence of the Top Gate Material

Furthermore, we investigate the effect of two different gate metals on the mobility and percolation density. We chose PolySi and titanium nitride (TiN) as top gate materials since both are widely applied gating materials for integrated CMOS device fabrication. While PolySi has generally larger mobilities, which indicates a small disorder

potential and therefore a low dot-to-dot variation, TiN exhibits low resistivity and is superconducting at low temperatures, which is desirable for microwave qubit control and readout. The density dependent mobilities at 4.2 K, for both TiN and PolySi are shown in Fig.5.3a. There is a decrease by a factor of three in the maximum mobility when changing the material from PolySi to TiN while all other parameters in the fabrication remain the same. To investigate the underlying mechanism for the mobility difference, we perform high magnetic field Hall measurements on the TiN devices as well. Unlike PolySi which shows vanishing $\rho_{xx}$ in Fig.5.2a, $\rho_{xx}$ of TiN does not have well developed zeros. This can be attributed to the lower mobility and could be due to multiple subband transport [208] (see section 5.10.3 for further details). At high electron concentrations and in the presence of compressive stress, multiple subbands can be occupied and thus introduce inter-subband scattering at low temperatures.

To explain the inter-subband scattering, we firstly consider the effect of strain. On silicon (100) surfaces, materials used as top gates with certain coefficient of thermal expansion (CTE) introduce compressive strain [209]. This leads to a decrease in the energy splitting of two subsequent subbands [100, 210, 211]. Strain simulations, described in Appendix D, indicate a large difference in strain between TiN and PolySi. However, the strain could only decrease the TiN mobility by roughly 10 percent rather than the three fold decrease observed [211]. This difference could be explained by the oxygen scavenging of TiN on $SiO_2$ [212]. When depositing TiN on a $SiO_2$ surface, $SiO_2$ gets reduced to $SiO_x$ and the free oxygen combines with TiN to form $TiO_2$ and titanium oxynitride ($TiN_xO_y$). This process creates charged oxygen vacancies in the $SiO_2$ layer and because the oxide is very thin in these samples, the charge carriers can then scatter at these defects thus reducing the overall mobility. Indeed, fits of the KKB model to the TiN data indicate a significantly higher $N_C$ than PolySi consistent with the scavenging hypothesis. Those two effects combined therefore could explain the difference in mobilities between the two gate metals.

## 5.6 Conclusion

In summary, we have characterized SiMOSFET samples using Hall effect measurements. We found a record mobility of $17.5 \times 10^3\,\mathrm{cm}^2/\mathrm{Vs}$ which is the highest reported mobility to date for SiMOSFET samples with sub-10 nm oxide thickness. Further, we have shown that the dominant mobility limiting factor are charges near the conducting channel, which can be improved by further reducing the impurity levels in the substrate. For example, an epitaxial layer can reach a background doping level of roughly $1 \times 10^{12}\,\mathrm{cm}^{-3}$, which is three orders of magnitude lower than the samples measured in this study. Additionally, we show that the choice of top gate material directly affects the mobility and percolation density. Factors such as strain and oxygen scavenging could explain the strong influence on both parameters. This demonstrates that the choice of top gate material is of paramount importance. The MOS interface has been widely identified as the source for charge noise and disorder sites, which limits the qubit performance and upscaling. To further improve the qubit device fabrication, more systematical investigations are needed. The Hallbar mobility and the analysis presented in this study could provide valuable insight into the gate stack over a large device area and direct further fabrication optimizations, which could pave the way for a large scale spin qubit processor integration with a full CMOS process.

## 5.7 Acknowledgements

This work was performed as part of imec's Industrial Affiliation Program (IIAP) on Quantum Computing. Additionally, this work was supported by the Swiss Nanoscience Institute (SNI), the Swiss National Science Foundation (SNF), the National Centers of Competence in Research (NCCR) SPIN and the EU H2020 European Microkelvin Platform (EMP) grant No. 824109.

## 5.8 Author contributions

T.N.C., A.E. and D.M.Z performed the experiments, analysed the measurements and wrote the manuscript with input from all authors. B.G. designed the test structures. S.K. and J.J. fabricated the devices. F.A.M. performed the strain simulations. The work was completed with assistance from R.L., P.VD. and I.R..

## 5.9 Data availability statement

The data supporting the plots of this paper are available at the Zenodo repository at https://doi.org/10.5281/zenodo.4784856.

## 5.10 Appendix

### 5.10.1 Mobility as a function of linear density and MIT fitting range

During the calculation of the mobility at the lowest temperature, we observed a peak mobility higher than the KKB model (see Fig.5.1b). We associated this deviation to the non-linear density dependence in the small top gate voltage regime at the lowest temperature as shown in the inset of Fig.5.1a. This assumption is further supported because the theoretical curve can be recovered using a linear extrapolated density when calculating the mobility (see Fig.5.4). This behaviour can be explained within the KKB theory, where the depletion charge density $n_{dep}$ is implicitly assumed to be significantly smaller than the sheet density $n_S$ especially in the critical regime of maximum mobility [137]. If the density becomes non-linear, this violation of the linear density assumption has a significant impact when calculating the finite extent of the wave function $b$ within the Coulomb scattering term $\langle|U_C(q)|^2\rangle$ and the dielectric response function $\varepsilon$. Further research in this regime is needed in order to capture the behaviour found in this work, but it exceeds the scope of this work. Nevertheless, we emphasize the mobility of $17.5 \times 10^3\,\mathrm{cm}^2/\mathrm{Vs}$ is the properly measured mobility, and the slightly lower peak mobility of

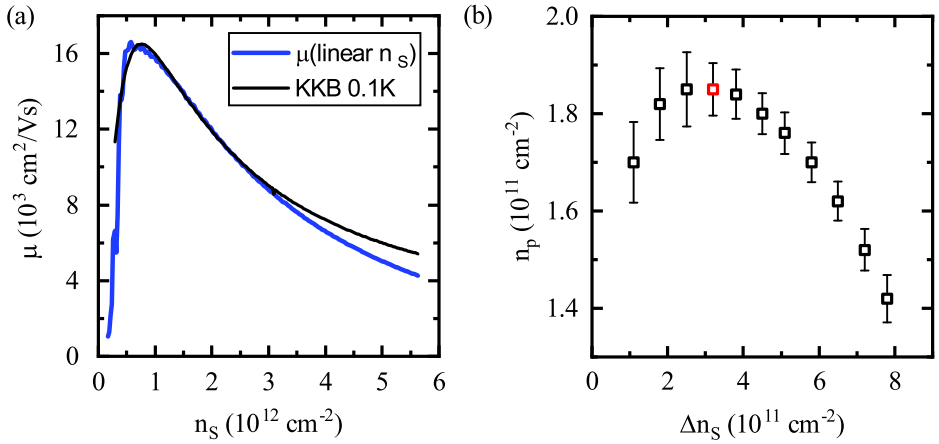


**Figure 5.4: Mobility as a function of linear density and MIT fitting range** (a) When using a linearly extrapolated (instead of the carefully extracted) density in order to calculate the mobility of our sample (blue), the peak mobility becomes slightly smaller than previously demonstrated in Fig.5.1b. Additionally, we can fit the KKB theory (black) self-consistently with the other temperature data highlighting the importance of the density values. (b) By varying $\Delta n_s$ for extracting the percolation density $n_p$ within the metal to insulator transition (MIT) model, we determine the optimal fitting range. We chose $\Delta n_s$ =3.2 $\times$ $10^{11}\,\mathrm{cm}^{-2}$ (indicated by the red box) because the extracted $n_p$ does not change significantly while changing $\Delta n_s$.

$16.5 \times 10^3\,\mathrm{cm}^2/\mathrm{Vs}$ in Fig.5.4 is a modeled mobility assuming a linear density model. The previous mobility record was $\approx 10 \times 10^3\,\mathrm{cm}^2/\mathrm{Vs}$ for a comparable sample although the oxide was slightly thicker in that work[28].

The metal to insulator transition model (MIT) we used in this work is only valid at very low densities (below $1 \times 10^{12}\,\mathrm{cm}^{-2}$ and therefore is rather sensitive to the fitting range. In order to find the appropriate fitting range, we varied both the minimum and maximum value independently. As shown in Fig.5.4, we determined that fitting the data between $2.7 \times 10^{11}\,\mathrm{cm}^{-2}$ and $6.0 \times 10^{11}\,\mathrm{cm}^{-2}$ yields the most reliable outcome because variations in the fitting range do not significantly change the result.

### 5.10.2 Extraction of effective mass and quantum lifetime

In order validate our evaluation approach and our experiments, we extract the effective mass from the temperature dependence of the SdH oscillations. For that, we subtract a polynominal background from the $\rho_{xx}$ data and use the following formula as described

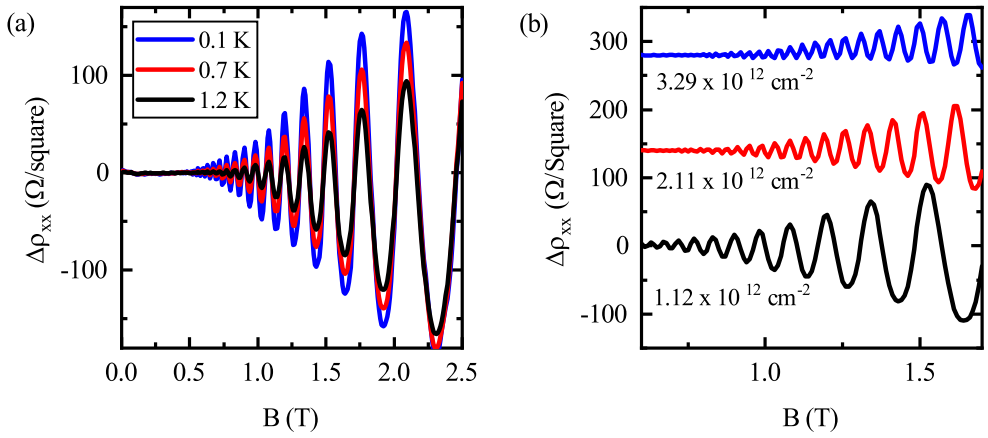


**Figure 5.5: SdH oscillations** (a) We can extract the effective mass by analysing the temperature dependent SdH oscillations at various magnetic field values $B$. (b) The envelope of the SdH oscillations in the fully spin and valley degenerate regime ($<$ 2.5 T) we can extract the quantum lifetime $\tau_q$ for various densities. Curves are offset for clarity.

in [213, 214]

$$\frac{\Delta\rho_{xx}(T)}{\Delta\rho_{xx}(T_0)} = \frac{T}{T_0} \cdot \frac{\sinh\chi(T)}{\sinh\chi(T_0)} \tag{5.1}$$

with $\chi(T) = 2\pi^2 k_B T/\hbar\omega_c$ and $\omega_c = eB/m^*$. Here, $T$ is the temperature, $T_0$ the lowest temperature, $k_B$ is the Boltzmann constant, $\hbar$ the reduced Plank constant, $e$ the electric charge, $B$ the magnetic field and $m^*$ the effective mass. Using the effective mass as the only free fit parameter, we extracted $m^* = 0.21 \pm 0.02 \cdot m_0$, which is close to the expected value of $m^* = 0.19 \cdot m_e$.

Further, the envelope of the SdH oscillations allows for the extraction of the quantum lifetime $\tau_q$. For that, we use the following formula

$$ln\left(\frac{\Delta\rho_{xx}(B)\sinh\chi}{\chi}\right) = C - \frac{\pi m^*}{eB\tau_q} \tag{5.2}$$

Therefore, by analysing the slope of the magnetic field dependent logarithmic term we can extract $\tau_q$ for all measured densities and temperatures. In combination with the transport lifetime $\tau_t$ we can then further extract the dingle ratio as described in the main text.

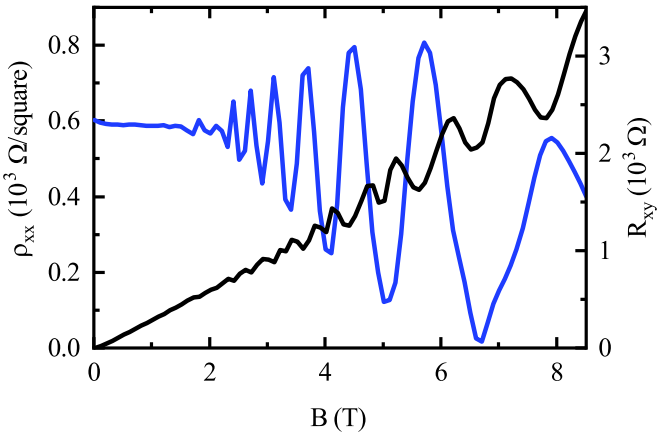


**Figure 5.6: TiN data at high fields** Longitudinal resistivity $\rho_{xx}$ (blue) and transverse Hall resistance $R_{xy}$ (black) of the sample measured with a TiN top gate at 500 mK. Both the not well developed zeroes in $\rho_{xx}$ and the oscillating $R_{xy}$ indicate multiple subband occupancy.

### 5.10.3 TiN data at high fields

In comparison to the reported data in Fig.5.2a, TiN does not show well developed zeroes in the longitudinal resistivity $\rho_{xx}$ at high magnetic fields at a temperature of 500 mK (see Fig.5.7), as expected for a much lower mobility. Further, the transversal Hall resistance $R_{xy}$ shows oscillating features instead of the expected Hall plateaus. This could be due to multiple subbands contributing to the overall transport or with the increased density of background charges due to the above mentioned oxygen scavenging.

### 5.10.4 Strain simulations

We quantify the stain induced in the 2DEG due to the different thermal expansion coefficients of both gate materials. The strain was simulated using a commercially available software [215]. The silicon was simulated isotropically. The temperature dependence of the CTE for PolySi up to room temperature is assumed to be linear because there is no reported data above 200 K [144]. Further, we neglect the intrinsic strain induced during the fabrication process, which is beyond the scope of this work. Thermal contraction is considered from room temperature down to the cryogenic mea-

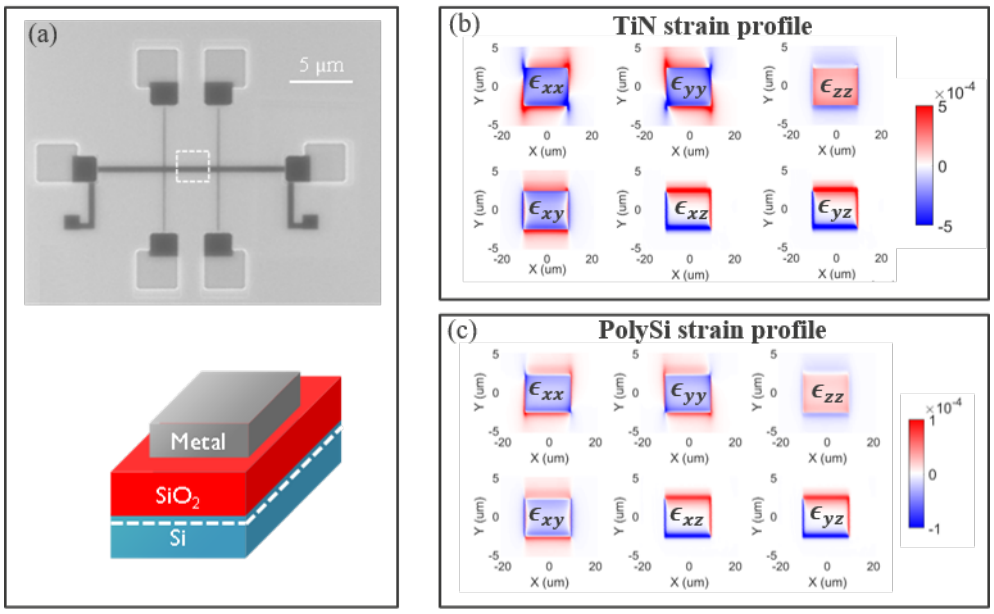


**Figure 5.7: Gate material strain simulations** (a) Schematic of the Hall bar used for the strain simulation. The strain in the channel was calculated using sprocess in the region indicated by the dashed white line. (b, c) The strain in the channel for the PolySi and TiN respectively. The model uses literature values for the thermal expansion coefficient for both materials.

surement temperatures. All simulations were performed in three dimensions and the components of strain $\epsilon_x, \epsilon_y, \epsilon_z$ are calculated 5 nm below the oxide due to the finite extension of the wavefunction. As shown in Fig.5.7b and c, there is a large difference in strain between TiN and PolySi. While TiN induces strain up to $2.4 \times 10^{-4}$, PolySi induces significantly less strain of approximately only $0.28 \times 10^{-4}$.

# 6 Conclusion and Outlook

This thesis has put a strong focus on two of the most promising materials for quantum computing applications − graphene and silicon. Both materials have been investigated thoroughly and have shown fascinating physics when it comes to adding insights into quantum phenomena.

Chapter 3 has discussed the effects of a remote hydrogen plasma on both graphite and graphene surfaces. The plasma creates hydrogen ions as well as radicals and with the sample being placed at a certain distance to the glowing region, anisotropic etching occurs. The switch from isotropic to anisotropic etching happens because of the recombination of hydrogen ions to hydrogen molecules, leaving only hydrogen radicals as reactive species in the reaction chamber above the investigated samples. One of the key characteristics of etching with a remote hydrogen plasma is that the edges have zigzag termination, which can be used for spintronic or spin-filtering applications. Furthermore, etching only occurs at pre-existing defects in the graphene lattice, for example vacancies or non-carbon atoms, which can be used for graphene nanoribbon fabrication. The latter can be accomplished by defining holes with electron beam lithography and subsequent etching of the graphene sheet with an argon plasma. By exposing the created holes to a remote hydrogen plasma, the etch pits become anisotropic and nanoribbons can be found between two neighbouring holes. Using this method, a smooth transition from nanoribbon to bulk graphene can be achieved and allows for high quality ohmic contacts to the bulk graphene which is beneficial for hole or electron transport studies.

This finding indicates that ZZ-GNRs can be fabricated using a remote hydrogen plasma. However, studies have found that the edge quality is not as crystalline as it needs to be in order to show the desired effects. Therefore, the focus of future experiments should lay on the etch process itself to understand the reaction on an atomic level. This could lead to new insights and an improvement of the edge quality by finding a more suitable

range of pressure and temperature where the process is even more anisotropic. Further, hBN has an influence on the etching process due to the small lattice mismatch. The associated Moiré pattern influences the electronic structure of graphene which might change the etching process leading to a poorer edge quality. Therefore, studies that focus on the angle mismatch between graphene and hBN might allow new insights into the etching process.

Switching from a remote hydrogen plasma to a remote nitrogen plasma is supposed to change the termination of the induced anisotropic etch pits in graphene and graphite. In chapter 4, we used a microwave generator in order to ignite a remote nitrogen plasma and then investigated the effects on graphite surfaces. Even though all the possible parameters have been explored to their fullest extent, we were not able to induce anisotropic etching in our samples. Potential reasons for this might be either the too short distance to the plasma, not enough microwave power to create nitrogen radicals, a too fast nitrogen gas flow over the sample or the recombination of the desired species happening too early. Further investigations into the observed parameters might result in anisotropic etching.

As soon as both etching techniques have been optimised, high quality AC- and ZZ-GNRs can be fabricated using the above mentioned methods. This will then allow future research to focus on specific effects such as the helical gap and Majorana fermions in AC-GNRs as well as magnetic ordering and spin-filtering devices with ZZ-GNRs.

Turning to silicon, another candidate for future quantum computing applications, allowed us to investigate mobility limiting factors in SiMOSFETs in chapter 5. These samples have been fabricated using a full CMOS process which will allow for an easy scaling as soon as quantum dots have been demonstrated to host the desired effects used in quantum computing schemes. This paper laid the groundwork for future quantum dot research by extracting the density, peak mobility and percolation density of a SiMOSFET with a PolySi top gate, finding a record mobility for devices with sub 10 nm oxide thickness of $17.5 \times 10^3\,\mathrm{cm}^2/\mathrm{Vs}$ at a relatively low density. In combination

with further key parameters such as the background charge density, the rms height of the interface roughness and the correlation length, this indicates a clean and smooth interface between silicon and its oxide which is advantageous for scaling as the dot-to-dot variance becomes rather small. Further, we showed that the top-gate material itself has a large influence on the mobility via the induced strain and oxygen scavenging. This is crucial when the conducting layer is as close to the surface on which the top gate lies as it is in our configuration. This means that when designing devices for quantum computing, the influence of the materials used is of paramount importance for the successful fabrication of a high quality quantum computing devices.

Using the knowledge gained in the above mentioned experiments, mobility optimised devices can be fabricated using the same CMOS process. A first step will be to produce a single quantum dot where the spins of the trapped electrons can be manipulated using various techniques. A second step will be to demonstrate double quantum dot physics such as bias triangles and Pauli spin blockade with these devices. Doing this, the material of the top gates will have a large influence on the quality and responsiveness of the qubit. Therefore, finding the ideal material for any given purpose is no easy task.

# References

[1] C. H. Bennett and D. P. DiVincenzo. *Quantum information and computation.* nature **404**, 247 (2000).

[2] H. Häffner, C. F. Roos, and R. Blatt. *Quantum computing with trapped ions.* Physics reports **469**, 155 (2008).

[3] J. Benhelm, G. Kirchmair, C. F. Roos, and R. Blatt. *Towards fault-tolerant quantum computing with trapped ions.* Nature Physics **4**, 463 (2008).

[4] C. D. Bruzewicz, J. Chiaverini, R. McConnell, and J. M. Sage. *Trapped-ion quantum computing: Progress and challenges.* Applied Physics Reviews **6**, 021314 (2019).

[5] J. You and F. Nori. *Quantum information processing with superconducting qubits in a microwave field.* Physical Review B **68**, 064509 (2003).

[6] J. M. Gambetta, J. M. Chow, and M. Steffen. *Building logical qubits in a superconducting quantum computing system.* npj Quantum Information **3**, 1 (2017).

[7] P. Krantz, M. Kjaergaard, F. Yan, T. P. Orlando, S. Gustavsson, and W. D. Oliver. *A quantum engineer's guide to superconducting qubits.* Applied Physics Reviews **6**, 021318 (2019).

[8] H.-L. Huang, D. Wu, D. Fan, and X. Zhu. *Superconducting quantum computing: a review.* Science China Information Sciences **63**, 1 (2020).

[9] D. Loss and D. P. DiVincenzo. *Quantum computation with quantum dots.* Physical Review A **57**, 120 (1998).

[10] J. R. Petta, A. C. Johnson, J. M. Taylor, E. A. Laird, A. Yacoby, M. D. Lukin, C. M. Marcus, M. P. Hanson, and A. C. Gossard. *Coherent manipulation of coupled electron spins in semiconductor quantum dots.* Science **309**, 2180 (2005).

[11] B. Trauzettel, D. V. Bulaev, D. Loss, and G. Burkard. *Spin qubits in graphene quantum dots.* Nature Physics **3**, 192 (2007).

[12] R. Hanson, L. P. Kouwenhoven, J. R. Petta, S. Tarucha, and L. M. Vandersypen. *Spins in few-electron quantum dots.* Reviews of modern physics **79**, 1217 (2007).

[13] N. W. Hendrickx, W. I. Lawrie, M. Russ, F. van Riggelen, S. L. de Snoo, R. N. Schouten, A. Sammak, G. Scappucci, and M. Veldhorst. *A four-qubit germanium quantum processor.* Nature **591**, 580 (2021).

[14] S. Nadj-Perge, S. Frolov, E. Bakkers, and L. P. Kouwenhoven. *Spin–orbit qubit in a semiconductor nanowire.* Nature **468**, 1084 (2010).

[15] J. Van den Berg, S. Nadj-Perge, V. Pribiag, S. Plissard, E. Bakkers, S. Frolov, and L. Kouwenhoven. *Fast spin-orbit qubit in an indium antimonide nanowire.* Physical review letters **110**, 066806 (2013).

[16] F. Froning, M. Rehmann, J. Ridderbos, M. Brauns, F. Zwanenburg, A. Li, E. Bakkers, D. Zumbühl, and F. Braakman. *Single, double, and triple quantum dots in Ge/Si nanowires.* Applied physics letters **113**, 073102 (2018).

[17] S. J. Angus, A. J. Ferguson, A. S. Dzurak, and R. G. Clark. *Gate-defined quantum dots in intrinsic silicon.* Nano letters **7**, 2051 (2007).

[18] F. A. Zwanenburg, A. S. Dzurak, A. Morello, M. Y. Simmons, L. C. Hollenberg, G. Klimeck, S. Rogge, S. N. Coppersmith, and M. A. Eriksson. *Silicon quantum electronics.* Reviews of modern physics **85**, 961 (2013).

[19] G. Scappucci. *Semiconductor materials stacks for quantum dot spin qubits.* arXiv preprint arXiv:2102.10897 (2021).

[20] S. Manzeli, D. Ovchinnikov, D. Pasquier, O. V. Yazyev, and A. Kis. *2D transition metal dichalcogenides.* Nature Reviews Materials **2**, 1 (2017).

[21] K. S. Novoselov, A. K. Geim, S. V. Morozov, D. Jiang, Y. Zhang, S. V. Dubonos, I. V. Grigorieva, and A. A. Firsov. *Electric field effect in atomically thin carbon films.* science **306**, 666 (2004).

[22] Y. Cao, V. Fatemi, S. Fang, K. Watanabe, T. Taniguchi, E. Kaxiras, and P. Jarillo-Herrero. *Unconventional superconductivity in magic-angle graphene superlattices.* Nature **556**, 43 (2018).

[23] J. Klinovaja and D. Loss. *Giant Spin-Orbit Interaction Due to Rotating Magnetic Fields in Graphene Nanoribbons.* Phys. Rev. X **3**, 011008 (2013).

[24] B. McCarroll and D. McKee. *Interaction of atomic hydrogen and nitrogen with graphite surfaces.* Nature **225**, 722 (1970).

[25] B. McCarroll and D. McKee. *The reactivity of graphite surfaces with atoms and molecules of hydrogen, oxygen and nitrogen.* Carbon **9**, 301 (1971).

[26] M. Fujita, K. Wakabayashi, K. Nakada, and K. Kusakabe. *Peculiar Localized States at Zigzag Graphite Edge.* J. Phys. Soc. Jpn. **65**, 1920 (1996).

[27] S. Shankar, A. Tyryshkin, J. He, and S. Lyon. *Spin relaxation and coherence times for electrons at the Si/SiO 2 interface.* Physical Review B **82**, 195323 (2010).

[28] D. Sabbagh, N. Thomas, J. Torres, R. Pillarisetty, P. Amin, H. George, K. Singh, A. Budrevich, M. Robinson, D. Merrill, *et al. Quantum Transport Properties of Industrial Si 28/Si O 2 28.* Physical Review Applied **12**, 014013 (2019).

[29] S. Rochette, M. Rudolph, A.-M. Roy, M. Curry, G. T. Eyck, R. Manginell, J. Wendt, T. Pluym, S. Carr, D. Ward, *et al. Quantum dots with split enhancement gate tunnel barrier control.* Applied Physics Letters **114**, 083101 (2019).

[30] R. Peierls. *Quelques propriétés typiques des corps solides.* In *Annales de l'institut Henri Poincaré*, volume 5, 177–222 (1935).

[31] L. D. Landau. *Zur Theorie der Phasenumwandlungen II.* Phys. Z. Sowjetunion **11**, 26 (1937).

[32] P. R. Wallace. *The band theory of graphite.* Physical review **71**, 622 (1947).

[33] J. McClure. *Diamagnetism of graphite.* Physical Review **104**, 666 (1956).

[34] J. Slonczewski and P. Weiss. *Band structure of graphite.* Physical review **109**, 272 (1958).

[35] G. W. Semenoff. *Condensed-matter simulation of a three-dimensional anomaly.* Physical Review Letters **53**, 2449 (1984).

[36] D. DiVincenzo and E. Mele. *Self-consistent effective-mass theory for intralayer screening in graphite intercalation compounds.* Physical Review B **29**, 1685 (1984).

[37] H. Boehm, A. Clauss, G. Fischer, and U. Hofmann. *Surface properties of extremely thin graphite lamellae.* In *Proceedings of the fifth conference on carbon*, volume 1, 73–80 (Pergamon Press New York, 1962).

[38] C. Oshima and A. Nagashima. *Ultra-thin epitaxial films of graphite and hexagonal boron nitride on solid surfaces.* Journal of Physics: Condensed Matter **9**, 1 (1997).

[39] I. Forbeaux, J.-M. Themlin, and J.-M. Debever. *Heteroepitaxial graphite on 6 H- SiC (0001): Interface formation through conduction-band electronic structure.* Physical Review B **58**, 16396 (1998).

[40] K. S. Novoselov, A. K. Geim, S. V. Morozov, D. Jiang, M. I. Katsnelson, I. Grigorieva, S. Dubonos, and A. Firsov. *Two-dimensional gas of massless Dirac fermions in graphene.* nature **438**, 197 (2005).

[41] S. Zhou, G.-H. Gweon, J. Graf, A. Fedorov, C. Spataru, R. Diehl, Y. Kopelevich, D.-H. Lee, S. G. Louie, and A. Lanzara. *First direct observation of Dirac fermions in graphite.* Nature physics **2**, 595 (2006).

[42] A. C. Neto, F. Guinea, N. M. Peres, K. S. Novoselov, and A. K. Geim. *The electronic properties of graphene.* Reviews of modern physics **81**, 109 (2009).

[43] Lumen-Learning. *Covalent Bonding - Sigma and Pi Bonds* (accessed December 1st, 2020). Https://courses.lumenlearning.com/cheminter/chapter/sigma-and-pi-bonds/.

[44] O. V. Yazyev. *Emergence of magnetism in graphene materials and nanostructures.* Rep. on Prog. in Phys. **73**, 056501 (2010).

[45] J. Williams, L. DiCarlo, and C. Marcus. *Quantum Hall effect in a gate-controlled pn junction of graphene.* Science **317**, 638 (2007).

[46] C. Handschin, P. Makk, P. Rickhaus, R. Maurand, K. Watanabe, T. Taniguchi, K. Richter, M.-H. Liu, and C. SchoÌˆnenberger. *Giant valley-isospin conductance oscillations in ballistic graphene.* Nano letters **17**, 5389 (2017).

[47] C. Bai and X. Zhang. *Klein paradox and resonant tunneling in a graphene superlattice.* Physical Review B **76**, 075430 (2007).

[48] G. Li, A. Luican, J. L. Dos Santos, A. C. Neto, A. Reina, J. Kong, and E. Andrei. *Observation of Van Hove singularities in twisted graphene layers.* Nature Physics **6**, 109 (2010).

[49] H. Guo, X. Zhu, S. Feng, and R. T. Scalettar. *Pairing symmetry of interacting fermions on a twisted bilayer graphene superlattice.* Physical Review B **97**, 235453 (2018).

[50] G. Chen, A. L. Sharpe, P. Gallagher, I. T. Rosen, E. J. Fox, L. Jiang, B. Lyu, H. Li, K. Watanabe, T. Taniguchi, *et al. Signatures of tunable superconductivity in a trilayer graphene moiré superlattice.* Nature **572**, 215 (2019).

[51] Y.-W. Son, M. L. Cohen, and S. G. Louie. *Half-metallic graphene nanoribbons.* Nature **444**, 347 (2006).

[52] F. Muñoz-Rojas, J. Fernández-Rossier, and J. Palacios. *Giant magnetoresistance in ultrasmall graphene based devices.* Physical review letters **102**, 136810 (2009).

[53] F. Sols, F. Guinea, and A. C. Neto. *Coulomb blockade in graphene nanoribbons.* Physical Review Letters **99**, 166803 (2007).

[54] A. C. Neto, F. Guinea, and N. Peres. *Edge and surface states in the quantum Hall effect in graphene.* Physical Review B **73**, 205408 (2006).

[55] I. Martin and Y. M. Blanter. *Transport in disordered graphene nanoribbons.* Physical Review B **79**, 235132 (2009).

[56] J. Cai, P. Ruffieux, R. Jaafar, M. Bieri, T. Braun, S. Blankenburg, M. Muoth, A. P. Seitsonen, M. Saleh, X. Feng, K. Muellen, and R. Fasel. *Atomically precise bottom-up fabrication of graphene nanoribbons.* Nature **466**, 470 (2010).

[57] P. Ruffieux, S. Wang, B. Yang, C. Sánchez-Sánchez, J. Liu, T. Dienel, L. Talirz, P. Shinde, C. A. Pignedoli, and D. Passerone. *On-surface synthesis of graphene nanoribbons with zigzag edge topology.* Nature **531**, 489 (2016).

[58] M. Sprinkle, M. Ruan, Y. Hu, J. Hankinson, M. Rubio-Roy, B. Zhang, X. Wu, C. Berger, and W. A. De Heer. *Scalable templated growth of graphene nanoribbons on SiC.* Nature nanotechnology **5**, 727 (2010).

[59] J. Bai, X. Duan, and Y. Huang. *Rational fabrication of graphene nanoribbons using a nanowire etch mask.* Nano letters **9**, 2083 (2009).

[60] L. Jiao, L. Xie, and H. Dai. *Densely aligned graphene nanoribbons at 35 nm pitch.* Nano Research **5**, 292 (2012).

[61] D. V. Kosynkin, A. L. Higginbotham, A. Sinitskii, J. R. Lomeda, A. Dimiev, B. K. Price, and J. M. Tour. *Longitudinal unzipping of carbon nanotubes to form graphene nanoribbons.* Nature **458**, 872 (2009).

[62] X. Li, X. Wang, L. Zhang, S. Lee, and H. Dai. *Chemically Derived, Ultrasmooth Graphene Nanoribbon Semiconductors.* Science **319**, 1229 (2008).

[63] L. Jiao, L. Zhang, X. Wang, G. Diankov, and H. Dai. *Narrow graphene nanoribbons from carbon nanotubes.* Nature **458**, 877 (2009).

[64] L. Jiao, X. Wang, G. Diankov, H. Wang, and H. Dai. *Facile synthesis of high-quality graphene nanoribbons.* Nature Nanotechnology **5**, 321 (2010).

[65] A. L. Elías, A. R. Botello-Méndez, D. Meneses-Rodríguez, V. Jehová González, D. Ramirez-Gonzalez, L. Ci, E. Munoz-Sandoval, P. M. Ajayan, H. Terrones, and M. Terrones. *Longitudinal cutting of pure and doped carbon nanotubes to form graphitic nanoribbons using metal clusters as nanoscalpels.* Nano letters **10**, 366 (2010).

[66] D. Wei, L. Xie, K. K. Lee, Z. Hu, S. Tan, W. Chen, C. H. Sow, K. Chen, Y. Liu, and A. T. S. Wee. *Controllable unzipping for intramolecular junctions of graphene nanoribbons and single-walled carbon nanotubes.* Nature communications **4**, 1 (2013).

[67] L. Xie, H. Wang, C. Jin, X. Wang, L. Jiao, K. Suenaga, and H. Dai. *Graphene nanoribbons from unzipped carbon nanotubes: atomic structures, Raman spectroscopy, and electrical properties.* Journal of the American Chemical Society **133**, 10394 (2011).

[68] K. Hikosaka, T. Mimura, and K. Joshin. *Selective dry etching of AlGaAs-GaAs heterojunction.* Japanese Journal of Applied Physics **20**, L847 (1981).

[69] S. Tachi, K. Tsujimoto, S. Arai, and T. Kure. *Low-temperature dry etching.* Journal of Vacuum Science & Technology A: Vacuum, Surfaces, and Films **9**, 796 (1991).

[70] J. Garra, T. Long, J. Currie, T. Schneider, R. White, and M. Paranjape. *Dry*

*etching of polydimethylsiloxane for microfluidic systems.* Journal of Vacuum Science & Technology A: Vacuum, Surfaces, and Films **20**, 975 (2002).

[71] J. Park, H. Park, Y. Hahn, G.-C. Yi, and A. Yoshikawa. *Dry etching of ZnO films and plasma-induced damage to optical properties.* Journal of Vacuum Science & Technology B: Microelectronics and Nanometer Structures Processing, Measurement, and Phenomena **21**, 800 (2003).

[72] R. Yang, L. Zhang, Y. Wang, Z. Shi, D. Shi, H. Gao, E. Wang, and G. Zhang. *An Anisotropic Etching Effect in the Graphene Basal Plane.* Adv. Mater. **22**, 4014 (2010).

[73] L. Zhang, D. A. Pejaković, B. Geng, and J. Marschall. *Surface modification of highly oriented pyrolytic graphite by reaction with atomic nitrogen at high temperatures.* Appl. Surf. Sci. **257**, 5647 (2011).

[74] F. F. Chen *et al. Introduction to plasma physics and controlled fusion*, volume 1 (Springer, 1984).

[75] K. E. Shuler and K. J. Laidler. *The Kinetics of Heterogeneous Atom and Radical Reactions. I. The Recombination of Hydrogen Atoms on Surfaces.* J Chem. Phys. **17**, 1212 (1949).

[76] R. K. Grubbs and S. M. George. *Attenuation of hydrogen radicals traveling under flowing gas conditions through tubes of different materials.* J. Vac. Sci. Technol. A **24**, 486 (2006).

[77] A. Davydova, E. Despiau-Pujo, G. Cunge, and D. B. Graves. *Etching mechanisms of graphene nanoribbons in downstream H2 plasmas: insights from molecular dynamics simulations.* J. Phys. D: Appl. Phys. **48**, 195202 (2015).

[78] A. Horn, A. Schenk, J. Biener, B. Winter, C. Lutterloh, M. Wittmann, and J. Kueppers. *H atom impact induced chemical erosion reaction at CH film surfaces.* Chem. Phys. Lett. **231**, 193 (1994).

[79] Ç. Ö. Girit, J. C. Meyer, R. Erni, M. D. Rossell, C. Kisielowski, L. Yang, C.-H. Park, M. Crommie, M. L. Cohen, S. G. Louie, *et al. Graphene at the edge: stability and dynamics.* science **323**, 1705 (2009).

[80] K. Kim, S. Coh, C. Kisielowski, M. Crommie, S. G. Louie, M. L. Cohen, and A. Zettl. *Atomically perfect torn graphene edges and their reversible reconstruction.* Nature communications **4**, 1 (2013).

[81] Z. Sun, X. Huang, F. Liu, X. Yang, C. Rösler, R. A. Fischer, M. Muhler, and W. Schuhmann. *Amine-based solvents for exfoliating graphite to graphene outperform the dispersing capacity of N-methyl-pyrrolidone and surfactants.* Chemical Communications **50**, 10382 (2014).

[82] D. Bischoff, A. Varlet, P. Simonet, M. Eich, H. Overweg, T. Ihn, and K. Ensslin. *Localized charge carriers in graphene nanodevices.* Applied Physics Reviews **2**, 031301 (2015).

[83] V. W. Brar, Y. Zhang, Y. Yayon, T. Ohta, J. L. McChesney, A. Bostwick, E. Rotenberg, K. Horn, and M. F. Crommie. *Scanning tunneling spectroscopy of inhomogeneous electronic structure in monolayer and bilayer graphene on SiC.* Applied Physics Letters **91**, 122102 (2007).

[84] G. M. Rutter, J. Crain, N. Guisinger, T. Li, P. First, and J. Stroscio. *Scattering and interference in epitaxial graphene.* Science **317**, 219 (2007).

[85] M. Corso, E. Carbonell-Sanromà, and D. G. d. Oteyza. *Bottom-up fabrication of atomically precise graphene nanoribbons.* In *On-Surface Synthesis II* (Springer Nature, 2018).

[86] O. Gröning, S. Wang, X. Yao, C. A. Pignedoli, G. B. Barin, C. Daniels, A. Cupo, V. Meunier, X. Feng, A. Narita, K. Müllen, P. Ruffieux, and R. Fasel. *Engineering of robust topological quantum phases in graphene nanoribbons.* Nature **560**, 209 (2018).

[87] M. K. Rehmann, Y. B. Kalyoncu, M. Kisiel, N. Pascher, F. J. Giessibl, F. Müller, K. Watanabe, T. Taniguchi, E. Meyer, M.-H. Liu, and D. M. Zumbühl. *Characterization of hydrogen plasma defined graphene edges.* Carbon **150**, 417 (2019).

[88] R. Beams, L. G. Cançado, and L. Novotny. *Raman characterization of defects and dopants in graphene.* Journal of Physics: Condensed Matter **27**, 083002 (2015).

[89] M. Ishigami, J. Chen, W. Cullen, M. Fuhrer, and E. Williams. *Atomic structure of graphene on SiO2.* Nano letters **7**, 1643 (2007).

[90] M. Katsnelson and A. Geim. *Electron scattering on microscopic corrugations in graphene.* Philosophical Transactions of the Royal Society A: Mathematical, Physical and Engineering Sciences **366**, 195 (2008).

[91] S. Morozov, K. Novoselov, M. Katsnelson, F. Schedin, D. Elias, J. A. Jaszczak, and A. Geim. *Giant intrinsic carrier mobilities in graphene and its bilayer.* Physical review letters **100**, 016602 (2008).

[92] T. Ando. *Screening effect and impurity scattering in monolayer graphene.* Journal of the Physical Society of Japan **75**, 074716 (2006).

[93] K. Nomura and A. H. MacDonald. *Quantum transport of massless Dirac fermions.* Physical review letters **98**, 076602 (2007).

[94] E. Hwang, S. Adam, and S. D. Sarma. *Carrier transport in two-dimensional graphene layers.* Physical review letters **98**, 186806 (2007).

[95] J.-H. Chen, C. Jang, S. Xiao, M. Ishigami, and M. S. Fuhrer. *Intrinsic and extrinsic performance limits of graphene devices on SiO 2.* Nature nanotechnology **3**, 206 (2008).

[96] C. R. Dean, A. F. Young, I. Meric, C. Lee, L. Wang, S. Sorgenfrei, K. Watanabe, T. Taniguchi, P. Kim, K. L. Shepard, and J. Hone. *Boron nitride substrates for high-quality graphene electronics.* Nature Nanotechnology **5**, 722 (2010).

[97] C. Handschin. *Quantum transport in encapsulated graphene" pn" junctions.* Ph.D. thesis, University_of_Basel (2017).

[98] G. Giovannetti, P. A. Khomyakov, G. Brocks, P. J. Kelly, and J. Van Den Brink. *Substrate-induced band gap in graphene on hexagonal boron nitride: Ab initio density functional calculations.* Physical Review B **76**, 073103 (2007).

[99] J. R. Chelikowsky and M. L. Cohen. *Nonlocal pseudopotential calculations for the electronic structure of eleven diamond and zinc-blende semiconductors.* Physical Review B **14**, 556 (1976).

[100] T. Ando, A. B. Fowler, and F. Stern. *Electronic properties of two-dimensional systems.* Reviews of Modern Physics **54**, 437 (1982).

[101] F. Schäffler, D. Többen, H.-J. Herzog, G. Abstreiter, and B. Holländer. *High-electron-mobility Si/SiGe heterostructures: influence of the relaxed SiGe buffer layer.* Semiconductor science and technology **7**, 260 (1992).

[102] R. Vrijen, E. Yablonovitch, K. Wang, H. W. Jiang, A. Balandin, V. Roychowdhury, T. Mor, and D. DiVincenzo. *Electron-spin-resonance transistors for quantum computing in silicon-germanium heterostructures.* Physical Review A **62**, 012306 (2000).

[103] M. Friesen, P. Rugheimer, D. E. Savage, M. G. Lagally, D. W. van der Weide, R. Joynt, and M. A. Eriksson. *Practical design and simulation of silicon-based quantum-dot qubits.* Physical Review B **67**, 121301 (2003).

[104] D. Paul, J. Cleaver, H. Ahmed, and T. Whall. *Coulomb blockade in silicon based structures at temperatures up to 50 K.* Applied physics letters **63**, 631 (1993).

[105] D. Ali and H. Ahmed. *Coulomb blockade in a silicon tunnel junction device.* Applied physics letters **64**, 2119 (1994).

[106] A. Morello, J. J. Pla, F. A. Zwanenburg, K. W. Chan, K. Y. Tan, H. Huebl, M. Möttönen, C. D. Nugroho, C. Yang, J. A. van Donkelaar, A. D. C. Alves, D. N. Jamieson, C. C. Escott, L. C. L. Hollenberg, R. G. Clark, and A. S. Dzurak. *Single-shot readout of an electron spin in silicon.* Nature **467**, 687 (2010).

[107] J. J. Pla, K. Y. Tan, J. P. Dehollain, W. H. Lim, J. J. Morton, D. N. Jamieson, A. S. Dzurak, and A. Morello. *A single-atom electron spin qubit in silicon.* Nature **489**, 541 (2012).

[108] R. Maurand, X. Jehl, D. Kotekar-Patil, A. Corna, H. Bohuslavskyi, R. Laviéville, L. Hutin, S. Barraud, M. Vinet, M. Sanquer, *et al. A CMOS silicon spin qubit.* Nature communications **7**, 1 (2016).

[109] G. Tosi, F. A. Mohiyaddin, V. Schmitt, S. Tenberg, R. Rahman, G. Klimeck, and A. Morello. *Silicon quantum processor with robust long-distance qubit couplings.* Nature communications **8**, 1 (2017).

[110] L. Petit, J. Boter, H. Eenink, G. Droulers, M. Tagliaferri, R. Li, D. Franke, K. Singh, J. Clarke, R. Schouten, *et al. Spin lifetime and charge noise in hot silicon quantum dot qubits.* Physical review letters **121**, 076801 (2018).

[111] T. Tanttu, B. Hensen, K. W. Chan, C. H. Yang, W. W. Huang, M. Fogarty, F. Hudson, K. Itoh, D. Culcer, A. Laucht, *et al. Controlling spin-orbit interactions in silicon quantum dots using magnetic field direction.* Physical Review X **9**, 021028 (2019).

[112] A. Sigillito, M. Gullans, L. Edge, M. Borselli, and J. Petta. *Coherent transfer of quantum information in a silicon double quantum dot using resonant SWAP gates.* npj Quantum Information **5**, 1 (2019).

[113] N. Hendrickx, W. Lawrie, L. Petit, A. Sammak, G. Scappucci, and M. Veldhorst. *A single-hole spin qubit.* Nature communications **11**, 1 (2020).

[114] B. P. Wuetz, M. P. Losert, A. Tosato, M. Lodari, P. L. Bavdaz, L. Stehouwer, P. Amin, J. S. Clarke, S. N. Coppersmith, A. Sammak, *et al. Effect of quantum Hall edge strips on valley splitting in silicon quantum wells.* arXiv preprint arXiv:2006.02305 (2020).

[115] H. Watzinger, C. Kloeffel, L. Vukusic, M. D. Rossell, V. Sessi, J. Kukucka, R. Kirchschlager, E. Lausecker, A. Truhlar, M. Glaser, A. Rastelli, A. Fuhrer, D. Loss, and G. Katsaros. *Heavy-hole states in germanium hut wires.* Nano letters **16**, 6879 (2016).

[116] C. Kloeffel, M. J. Rančić, and D. Loss. *Direct Rashba spin-orbit interaction in Si and Ge nanowires with different growth directions.* Physical Review B **97**, 235422 (2018).

[117] F. Froning, L. Camenzind, O. van der Molen, A. Li, E. Bakkers, D. Zumbühl, and F. Braakman. *Ultrafast hole spin qubit with gate-tunable spin-orbit switch.* arXiv preprint arXiv:2006.11175 (2020).

[118] F. Froning, M. Rančić, B. Hetényi, S. Bosco, M. Rehmann, A. Li, E. Bakkers, F. Zwanenburg, D. Loss, D. Zumbühl, *et al. Strong spin-orbit interaction and g-factor renormalization of hole spins in Ge/Si nanowire quantum dots.* arXiv preprint arXiv:2007.04308 (2020).

[119] C. Grazianetti, E. Cinquanta, and A. Molle. *Two-dimensional silicon: the advent of silicene.* 2D Materials **3**, 012001 (2016).

[120] M. A. Green. *Intrinsic concentration, effective densities of states, and effective mass in silicon.* Journal of Applied Physics **67**, 2944 (1990).

[121] M. Cardona and Y. Y. Peter. *Fundamentals of semiconductors* (Springer, 2005).

[122] L. Terrazos, E. Marcellina, S. Coppersmith, M. Friesen, A. Hamilton, X. Hu, B. Koiller, A. Saraiva, D. Culcer, and R. B. Capaz. *Theory of Hole-Spin Qubits in Strained Germanium Quantum Dots.* arXiv preprint arXiv:1803.10320 (2018).

[123] G. Scappucci, C. Kloeffel, F. A. Zwanenburg, D. Loss, M. Myronov, J.-J. Zhang, S. De Franceschi, G. Katsaros, and M. Veldhorst. *The germanium quantum information route.* arXiv preprint arXiv:2004.08133 (2020).

[124] J. H. Davies. *The physics of low-dimensional semiconductors: an introduction* (Cambridge university press, 1998).

[125] P. Mooney. *Strain relaxation and dislocations in SiGe/Si structures.* Materials Science and Engineering: R: Reports **17**, 105 (1996).

[126] S. Wolf. *Silicon processing for the VLSI era.* In *LATTICE*, 559–581 (1995).

[127] S. M. Sze and K. K. Ng. *Physics of semiconductor devices* (John wiley & sons, 2006).

[128] L. Tracy, E. Hwang, K. Eng, G. Ten Eyck, E. Nordberg, K. Childs, M. Carroll, M. Lilly, and S. D. Sarma. *Observation of percolation-induced two-dimensional metal-insulator transition in a Si MOSFET.* Physical Review B **79**, 235307 (2009).

[129] S. V. Amitonov, P. C. Spruijtenburg, M. W. Vervoort, W. G. van der Wiel, and F. A. Zwanenburg. *Depletion-mode quantum dots in intrinsic silicon.* Applied physics letters **112**, 023102 (2018).

[130] H. Köhler and M. Roos. *Quantitative determination of the valley splitting in n-type inverted silicon (100) MOSFET surfaces.* physica status solidi (b) **91**, 233 (1979).

[131] R. Nicholas, K. Von Klitzing, and T. Englert. *An investigation of the valley splitting in n-channel silicon< 100> inversion layers.* Solid State Communications **34**, 51 (1980).

[132] V. Pudalov and S. Semenchinskii. *QUANTUM OSCILLATIONS OF THE DENSITY AND FERMI ENERGY OF ELECTRONS AT AN INVERSION LAYER IN A MAGNETIC-FIELD.* JETP Lett **44** (1986).

[133] P. Weitz, R. Haug, K. Von Klitzing, and F. Schäffler. *Tilted magnetic field studies of spin-and valley-splittings in Si/Si1- xGex heterostructures.* Surface science **361**, 542 (1996).

[134] S. Koester, K. Ismail, and J. Chu. *Determination of spin-and valley-split energy levels in strained Si quantum wells.* Semiconductor science and technology **12**, 384 (1997).

[135] K. Lai, T. Lu, W. Pan, D. Tsui, S. Lyon, J. Liu, Y. Xie, M. Mühlberger, and F. Schäffler. *Valley splitting of Si/ Si 1- x Ge x heterostructures in tilted magnetic fields.* Physical Review B **73**, 161301 (2006).

[136] M. Xiao, M. House, and H. W. Jiang. *Measurement of the spin relaxation time of single electrons in a silicon metal-oxide-semiconductor-based quantum dot.* Physical review letters **104**, 096801 (2010).

[137] G. Kruithof, T. Klapwijk, and S. Bakker. *Temperature and interface-roughness dependence of the electron mobility in high-mobility Si (100) inversion layers below 4.2 K.* Physical Review B **43**, 6642 (1991).

[138] F. Stern and W. Howard. *Properties of semiconductor surface inversion layers in the electric quantum limit.* Physical Review **163**, 816 (1967).

[139] S. Goodnick, D. Ferry, C. Wilmsen, Z. Liliental, D. Fathy, and O. Krivanek. *Surface roughness at the Si (100)-SiO 2 interface.* Physical Review B **32**, 8171 (1985).

[140] A. Ourmazd, D. Taylor, J. Rentschler, and J. Bevk. *Siâ†' SiO 2 transformation: interfacial structure and mechanism.* Physical review letters **59**, 213 (1987).

[141] P. Price. *Two-dimensional electron transport in semiconductor layers. I. Phonon scattering.* Annals of Physics **133**, 217 (1981).

[142] K. Masaki, C. Hamaguchi, K. Taniguchi, and M. Iwase. *Electron mobility in Si inversion layers.* Japanese Journal of Applied Physics **28**, 1856 (1989).

[143] S.-i. Takagi, A. Toriumi, M. Iwase, and H. Tango. *On the universality of inversion layer mobility in Si MOSFET's: Part II-effects of surface orientation.* IEEE Transactions on Electron Devices **41**, 2363 (1994).

[144] T. Thorbeck and N. M. Zimmerman. *Formation of strain-induced quantum dots in gated semiconductor nanostructures.* AIP Advances **5**, 087107 (2015).

[145] S. S. Li. *Scattering mechanisms and carrier mobilities in semiconductors.* In *Semiconductor Physical Electronics*, 211–245 (Springer, 2006).

[146] Y. Takeda and T. Pearsall. *Failure of Matthiessen's rule in the calculation of carrier mobility and alloy scattering effects in Ga0. 47In0. 53As.* Electronics Letters **17**, 573 (1981).

[147] A. Bulusu and D. Walker. *Review of electronic transport models for thermoelectric materials.* Superlattices and Microstructures **44**, 1 (2008).

[148] E. Arnold. *Conduction mechanisms in bandtails at the Si/SiO2 interface.* Surface Science **58**, 60 (1976).

[149] A. Gold and V. Dolgopolov. *Temperature dependence of the conductivity for the two-dimensional electron gas: Analytical results for low temperatures.* Physical Review B **33**, 1076 (1986).

[150] K. Nakada, M. Fujita, G. Dresselhaus, and M. S. Dresselhaus. *Edge state in graphene ribbons: Nanometer size effect and edge shape dependence.* Phys. Rev. B **54**, 17954 (1996).

[151] Y.-W. Son, M. L. Cohen, and S. G. Louie. *Energy Gaps in Graphene Nanoribbons.* Phys. Rev. Lett. **97**, 216803 (2006).

[152] C. Tao, L. Jiao, O. V. Yazyev, Y.-C. Chen, J. Feng, X. Zhang, R. B. Capaz, J. M. Tour, A. Zettl, S. G. Louie, H. Dai, and M. F. Crommie. *Spatially resolving edge states of chiral graphene nanoribbons.* Nature Physics **7**, 616 (2011).

[153] M. Pan, E. C. Girão, X. Jia, S. Bhaviripudi, Q. Li, J. Kong, V. Meunier, and M. S. Dresselhaus. *Topographic and Spectroscopic Characterization of Electronic Edge States in CVD Grown Graphene Nanoribbons.* Nano Letters **12**, 1928 (2012).

[154] X. Zhang, O. V. Yazyev, J. Feng, L. Xie, C. Tao, Y.-C. Chen, L. Jiao, Z. Pedramrazi, A. Zettl, S. G. Louie, H. Dai, and M. F. Crommie. *Experimentally Engineering the Edge Termination of Graphene Nanoribbons.* ACS Nano **7**, 198 (2013).

[155] S. Wang, L. Talirz, C. A. Pignedoli, X. Feng, K. Müllen, R. Fasel, and P. Ruffieux. *Giant edge state splitting at atomically precise graphene zigzag edges.* Nature Communications **7**, 11507 (2016).

[156] G. Z. Magda, X. Jin, I. Hagymási, P. Vancsó, Z. Osvath, P. Nemes-Incze, C. Hwang, L. P. Biró, and L. Tapaszto. *Room-temperature magnetic order on zigzag edges of narrow graphene nanoribbons.* Nature **514**, 608 (2014).

[157] M. Han, B. Özyilmaz, Y. Zhang, and P. Kim. *Energy Band-Gap Engineering of Graphene Nanoribbons.* Phys. Rev. Lett. **98**, 206805 (2007).

[158] E. Mucciolo, A. Castro Neto, and C. Lewenkopf. *Conductance quantization and transport gaps in disordered graphene nanoribbons.* Phys. Rev. B **79**, 075407 (2009).

[159] J. B. Oostinga, B. Sacépé, M. F. Craciun, and A. F. Morpurgo. *Magnetotransport through graphene nanoribbons.* Phys. Rev. B **81**, 193408 (2010).

[160] C. Stampfer, J. Güttinger, S. Hellmüller, F. Molitor, K. Ensslin, and T. Ihn. *Energy Gaps in Etched Graphene Nanoribbons.* Phys. Rev. Lett. **102**, 506403 (2009).

[161] P. Gallagher, K. Todd, and D. Goldhaber-Gordon. *Disorder-induced gap behavior in graphene nanoribbons.* Phys. Rev. B **81**, 115409 (2010).

[162] X. Liu, J. Oostinga, A. Morpurgo, and L. Vandersypen. *Electrostatic confinement of electrons in graphene nanoribbons.* Phys. Rev. B **80**, 121407 (2009).

[163] *Energy and transport gaps in etched graphene nanoribbons* **25**.

[164] L. C. Campos, V. R. Manfrinato, J. D. Sanchez-Yamagishi, J. Kong, and P. Jarillo-Herrero. *Anisotropic etching and nanoribbon formation in single-layer graphene.* Nano Letters **9**, 2600 (2009).

[165] D. Geng, B. Wu, Y. Guo, B. Luo, Y. Xue, J. Chen, G. Yu, and Y. Liu. *Fractal Etching of Graphene.* J. Am. Chem. Soc. **135**, 6431 (2013).

[166] W. Guo, B. Wu, Y. Li, L. Wang, J. Chen, B. Chen, Z. Zhang, L. Peng, S. Wang, and Y. Liu. *Governing Rule for Dynamic Formation of Grain Boundaries in Grown Graphene.* ACS Nano **9**, 5792 (2015).

[167] Y. Zhang, Z. Li, P. Kim, L. Zhang, and C. Zhou. *Anisotropic Hydrogen Etching of Chemical Vapor Deposited Graphene.* ACS Nano **6**, 126 (2012).

[168] P. Nemes-Incze, G. Magda, K. Kamaras, and L. Biró. *Crystallographically selective nanopatterning of graphene on SiO2.* Nano Research **3**, 110 (2010).

[169] B. Krauss, P. Nemes-Incze, V. Skakalova, L. P. Biró, K. v. Klitzing, and J. Smet. *Raman Scattering at Pure Graphene Zigzag Edges.* Nano Letters **10**, 4544 (2010).

[170] F. Oberhuber, S. Blien, S. Heydrich, T. Yaghobian, Fatemeh Korn, C. Schüller, C. Strunk, D. Weiss, and J. Eroms. *Weak localization and Raman study of anisotropically etched graphene antidots.* Appl. Phys. Lett. **103**, 143111 (2013).

[171] F. Oberhuber, S. Blien, F. Schupp, D. Weiss, and J. Eroms. *Anisotropic etching of graphene in inert and oxygen atmospheres.* Phys. Status Solidi A **214**, 1600459 (2017).

[172] Z. Shi, R. Yang, L. Zhang, Y. Wang, D. Liu, D. Shi, E. Wang, and G. Zhang. *Patterning Graphene with Zigzag Edges by Self-Aligned Anisotropic Etching.* Adv. Mater. **23**, 3061 (2011).

[173] L. Xie, L. Jiao, and H. Dai. *Selective Etching of Graphene Edges by Hydrogen Plasma.* J. Am. Chem. Soc. **132**, 14751 (2010).

[174] G. Wang, S. Wu, T. Zhang, P. Chen, X. Lu, S. Wang, D. Wang, K. Watanabe, T. Taniguchi, D. Shi, R. Yang, and G. Zhang. *Patterning monolayer graphene with zigzag edges on hexagonal boron nitride by anisotropic etching.* Appl. Phys. Lett. **109**, 053101 (2016).

[175] G. Diankov, M. Neumann, and D. Goldhaber-Gordon. *Extreme Monolayer-Selectivity of Hydrogen-Plasma Reactions with Graphene.* ACS Nano **7**, 1324 (2013).

[176] G. Wang, S. Wu, T. Zhang, P. Chen, X. Lu, S. Wang, D. Wang, K. Watanabe, T. Taniguchi, and D. Shi. *Patterning monolayer graphene with zigzag edges on hexagonal boron nitride by anisotropic etching.* Appl. Phys. Lett. **109**, 053101 (2016).

[177] NGS Naturgraphit GmbH.

[178] R. K. Janev, D. Reiter, and U. Samm. *Collision Processes in Low-Temperature Hydrogen Plasmas* (Forschungszentrum Juelich GmbH, 2003).

[179] G. Dixon-Lewis, M. M. Sutton, and A. Williams. *The kinetics of hydrogen atom recombination.* Discussions of the Faraday Society **33**, 205 (1962).

[180] Suprasil 310, Heraeus Quarzglas GmbH.

[181] Y. Zhang, V. W. Brar, C. Girit, A. Zettl, and M. F. Crommie. *Origin of spatial charge inhomogeneity in graphene.* Nature Physics **5**, 722 (2009).

[182] R. Decker, Y. Wang, V. W. Brar, W. Regan, H.-Z. Tsai, Q. Wu, W. Gannett, A. Zettl, and M. F. Crommie. *Local Electronic Properties of Graphene on a BN Substrate via Scanning Tunneling Microscopy.* Nano Letters **11**, 2291 (2011).

[183] J. Xue, J. Sanchez-Yamagishi, D. Bulmash, P. Jacquod, A. Deshpande, K. Watanabe, T. Taniguchi, P. Jarillo-Herrero, and B. J. LeRoy. *Scanning tunnelling microscopy and spectroscopy of ultra-flat graphene on hexagonal boron nitride.* Nature Materials **10**, 282 (2011).

[184] Y. C. Kim and M. Boudart. *Recombination of O, N and H atoms on Silica: Kinetics and Mechanism.* ACS Langmuir **7**, 2999 (1991).

[185] T. Taniguchi and K. Watanabe. *Synthesis of high-purity boron nitride single crystals under high pressure by using Baâ€“BN solvent.* J. Cryst. Growth **303**, 525 (2007).

[186] A. C. Ferrari, J. C. Meyer, V. Scardaci, C. Casiraghi, M. Lazzeri, F. Mauri, S. Piscanec, D. Jiang, K. S. Novoselov, S. Roth, and A. K. Geim. *Raman Spectrum of Graphene and Graphene Layers.* Phys. Rev. Lett. **97**, 187401 (2006).

[187] D. C. Elias, R. R. Nair, T. M. G. Mohiuddin, S. V. Morozov, P. Blake, M. P. Halsall, A. C. Ferrari, D. W. Boukhvalov, M. I. Katsnelson, and A. K. Geim. *Control of graphene's properties by reversible hydrogenation: evidence for graphane.* Science **323**, 610 (2009).

[188] J. Sofo, A. Chaudhari, and G. Barber. *Graphane: A two-dimensional hydrocarbon.* Phys. Rev. B **75**, 153401 (2007).

[189] B. Eren, D. Hug, L. Marot, R. Pawlak, M. Kisiel, R. Steiner, D. M. Zumbühl, and E. Meyer. *Pure hydrogen low-temperature plasma exposure of HOPG and graphene: Graphane formation?* Beilstein Journal of Nanotechnology **3**, 852 (2012).

[190] C. Woods, F. Withers, M. Zhu, Y. Cao, G. Yu, A. Kozikov, M. B. Shalom, S. Morozov, M. van Wijk, and A. Fasolino. *Macroscopic self-reorientation of interacting two-dimensional crystals.* Nature communications **7**, 10800 (2016).

[191] D. Wang, G. Chen, C. Li, M. Cheng, W. Yang, S. Wu, G. Xie, J. Zhang, J. Zhao, and X. Lu. *Thermally Induced Graphene Rotation on Hexagonal Boron Nitride.* Phys. Rev. Lett. **116**, 126101 (2016).

[192] M. Moisan and Z. Zakrzewski. *Plasma sources based on the propagation of electromagnetic surface waves.* J. Phys. D: Appl. Phys. **24**, 1025 (1991).

[193] K. Sancier and H. Wise. *Diffusion and Heterogeneous Reaction. XI. Diffusion Coefficient Measurements for Gas Mixture of Atomic and Molecular Hydrogen.* Journal of Chemical Physics **51**, 1434 (1969).

[194] S. Weissman and E. Mason. *Estimation of the mutual diffusion coefficient of hydrogen atoms and molecules.* The Journal of Chemical Physics **36**, 794 (1962).

[195] R. Geick, C. H. Perry, and G. Rupprecht. *Normal modes in hexagonal boron nitride.* Phys. Rev. Lett. **146**, 543 (1966).

[196] M. Begliarbekov, K. Sasaki, O. Sul, E. Yang, and S. Strauf. *Optical Control of Edge Chirality in Graphene.* Nano Letters **11**, 4874 (2011).

[197] T. N. Camenzind. *Anisotropic etching in graphite induced by a remote nitrogen plasma.* Master's thesis, University of Basel (2015).

[198] D. Hug, S. Zihlmann, M. K. Rehmann, Y. B. Kalyoncu, T. N. Camenzind, L. Marot, K. Watanabe, T. Taniguchi, and D. M. Zumbühl. *Anisotropic etching of graphite and graphene in a remote hydrogen plasma.* npj 2D Materials and Applications **1**, 1 (2017).

[199] L. Vandersypen, H. Bluhm, J. Clarke, A. Dzurak, R. Ishihara, A. Morello, D. Reilly, L. Schreiber, and M. Veldhorst. *Interfacing spin qubits in quantum*

*dots and donorsâ€"hot, dense, and coherent.* npj Quantum Information **3**, 1 (2017).

[200] M. Veldhorst, J. Hwang, C. Yang, A. Leenstra, B. de Ronde, J. Dehollain, J. Muhonen, F. Hudson, K. M. Itoh, A. Morello, *et al. An addressable quantum dot qubit with fault-tolerant control-fidelity.* Nature nanotechnology **9**, 981 (2014).

[201] M. Veldhorst, C. Yang, J. Hwang, W. Huang, J. Dehollain, J. Muhonen, S. Simmons, A. Laucht, F. Hudson, K. M. Itoh, *et al. A two-qubit logic gate in silicon.* Nature **526**, 410 (2015).

[202] R. Li, L. Petit, D. P. Franke, J. P. Dehollain, J. Helsen, M. Steudtner, N. K. Thomas, Z. R. Yoscovits, K. J. Singh, S. Wehner, *et al. A crossbar network for silicon quantum dot qubits.* Science advances **4**, eaar3960 (2018).

[203] R. Li, N. D. Stuyck, S. Kubicek, J. Jussot, B. Chan, F. Mohiyaddin, A. Elsayed, M. Shehata, G. Simion, C. Godfrin, *et al. A flexible 300 mm integrated Si MOS platform for electron-and hole-spin qubits exploration.* In *2020 IEEE International Electron Devices Meeting (IEDM)*, 38–3 (IEEE, 2020).

[204] P. Lautenschlager, M. Garriga, L. Vina, and M. Cardona. *Temperature dependence of the dielectric function and interband critical points in silicon.* Physical Review B **36**, 4821 (1987).

[205] M. Tsukada. *On the tail states of the landau subbands in MOS structures under strong magnetic field.* Journal of the Physical Society of Japan **41**, 1466 (1976).

[206] J.-S. Kim, A. M. Tyryshkin, and S. A. Lyon. *Annealing shallow Si/SiO2 interface traps in electron-beam irradiated high-mobility metal-oxide-silicon transistors.* Applied Physics Letters **110**, 123505 (2017).

[207] F. Herman. *The electronic energy band structure of silicon and germanium.* Proceedings of the IRE **43**, 1703 (1955).

[208] G. Kruithof and T. Klapwijk. *Electron transport with two occupied subbands in a Si (100) inversion layer.* Physical Review B **42**, 11412 (1990).

[209] F. Nix and D. MacNair. *The thermal expansion of pure metals: copper, gold, aluminum, nickel, and iron.* Physical Review **60**, 597 (1941).

[210] S. Kawaji, K. Hatanaka, K. Nakamura, and S. Onga. *Mobility Hump and Inversion Layer Subbands in Si on Sapphire.* Journal of the Physical Society of Japan **41**, 1073 (1976).

[211] I. Eisele. *Stress and intersubband correlation in the silicon inversion layer.* Surface Science **73**, 315 (1978).

[212] E. O. Filatova, S. S. Sakhonenkov, A. S. Konashuk, S. A. Kasatikov, and V. V. Afanasâ€™ ev. *Inhibition of Oxygen Scavenging by TiN at the TiN/SiO2 Interface by Atomic-Layer-Deposited Al2O3 Protective Interlayer.* The Journal of Physical Chemistry C **123**, 22335 (2019).

[213] G. Bauer and H. Kahlert. *Low-temperature non-ohmic galvanomagnetic effects in degenerate n-type InAs.* Physical Review B **5**, 566 (1972).

[214] O. Celik, E. Tiras, S. Ardali, S. B. Lisesivdin, and E. Ozbay. *Determination of the in-plane effective mass and quantum lifetime of 2D electrons in AlGaN/GaN based HEMTs.* physica status solidi c **8**, 1625 (2011).

[215] Sentaurus Process - Technology Computer Aided Design (TCAD) | Synopsys.

# List of Figures

# Acknowledgements

The past four years have been an amazing journey through the possibilities of fabrication and low temperature measurements on different types of semiconductor devices. As with every journey, also this one had its fair share of ups and downs as well as dead ends. The one constant throughout the journey were the many people without whom this thesis would not have been completed.

First, a big thank you goes to my supervisor Prof. Dr. Dominik Zumbühl. I first encountered him as a lecturer in condensed matter physics during my undergrad studies and was amazed by his ability to convey complicated topics in an understandable way. His passion for physics and semiconductors in particular motivated me to start my doctorate, which resulted in four years of extensive research, discussions about physics and life in general and lots of perfectly made steaks. Thank you for granting me the opportunity to make my doctorate in your group.

Second, I would like to thank Prof. Dr. Floris Zwanenburg for his interest in my work and taking his time for being part of my PhD comittee. The interactions we had during conferences were very enlightening and contributed to my interest in silicon as a material for quantum computing.

Further tanks go to Prof. Dr. Ilaria Zardo for being my second supervisor. Her knowledge and enthusiasm helped me during the time I was fabricating nanowire related samples and I would like to thank her for allowing me to use her 4 K probe station for quick device testing.

A big thank you goes to all current and former group members of the Quantum Coherence Lab. Particularly, I would like to thank Dr. Mirko Rehmann for introducing me into the world of graphene during my project work and master thesis as well as helping me during the start of my doctorate. His knowledge and patience helped a lot while looking for atomically thin sheets of magic material and subsequently transferring it. Fabrication wise, I would also like to thank Dr. Florian Froning who introduced me to

nanowire fabrication and helped me a lot navigating the silicon literature. For the time I spent in the laboratory, I would like to thank Dr. Christian Scheller, Dr. Taras Patlatiuk and Dr. Mohammad Samani for their help while setting up the measurements and especially helping whenever there was an Igor or Python related problem. Both helped tremendously and without them, many bugs would still plague the measurement routines. Further, I would like to thank Miguel Carbadillo and Kristopher Cerveny for the pleasant atmosphere in the office and the diversified talks we had about podcasts, crazy dudes (usually from the podcasts) and health related topics.

In the later stages of my doctorate I got introduced to the group of Iuliana Radu at IMEC in Belgium. Via the European Microkelvin Platform they were able to provide us with SiMOSFET samples and the measurements from this collaboration lead to the second paper in this doctoral thesis. From this group I would like to thank Asser Elsayed for the numerous discussions we had during and after his stay in Basel and for the time we spend together analysing the data and writing the resulting paper. Additional thanks go to Bogdan Govereanu for supervising the project and to Fahd Mohiyaddin for the theoretical inputs.

Last, but not least, I would like to thank Seline Emmenegger for always believing in me and supporting me for more than the last four years. Without her, I would not be here and my level of English would not be on the level it is now. Thank you very much.

# Curriculum Vitae

Timothy Nigel Camenzind, from Gersau, Switzerland

| | |
|---|---|
| 2010 | Matura, Gymnasium Muttenz |
| 2011 | Military Service |
| 2012 - 2017 | Bachelor and Master studies in Nanosciences at the University of Basel |
| 2017 - 2021 | PhD at University of Basel |

### Publications

- D. Hug, S. Zihlmann, M. K. Rehmann, Y. B. Kalyoncu, T. N. Camenzind, L. Marot, K. Watanabe, T. Taniguchi, and D. M. Zumbühl. *Anisotropic etching of graphite and graphene in a remote hydrogen plasma.* npj 2D Materials and Applications **1**, 1 (2017).

- S. Keller, T. N. Camenzind, J. Abraham, A. Prescimone, D. Häussinger, E. C. Constable, and C. E. Housecroft. *Self-assembly of heteroleptic dinuclear silver (I) complexes bridged by bis (diphenylphosphino) ethyne.* Dalton Transactions **43**, 3 (2018).

- T. N. Camenzind, A. Elsayed, F. A. Mohiyaddin, R. Li, S. Kubicek, J. Jussot, P. Van Dorpe, B. Govoreanu, I. Radu, and D. M. Zumbühl. *High mobility SiMOSFETs fabricated in a full 300 mm CMOS process.* arXiv:2106.05254